Active Acoustics for Monitoring Unreported Leaks in Water Distribution Networks

by

Marshal Deep Kafle

A thesis
presented to the University of Waterloo
in fulfillment of the
thesis requirement for the degree of
Doctor of Philosophy
in
Engineering

Waterloo, Ontario, Canada, 2021

Examining Committee Membership

The following served on the Examining Committee for this thesis. The decision of the Examining Committee is by majority vote.

External Member:	Dr. Sunil K Sinha Professor, Dept. of Civil and Env. Engineering,, Virginia Tech
Supervisor(s):	Dr. Sriram Narasimhan Adjunct Professor, Dept. of Civil and Env. Engineering, University of Waterloo
Internal Member:	Dr. Giovanni Cascante Professor, Dept. of Civil and Env. Engineering, University of Waterloo
Internal Member:	Dr. Bryan Tolson Professor, Dept. of Civil and Env. Engineering, University of Waterloo
Internal-External Member:	Dr. Sean Peterson Professor, Dept. of Mech. and Mechatr. Engineering, University of Waterloo

Author's Declaration

This thesis consists of material all of which I authored or co-authored: see Statement of Contributions included in the thesis. This is a true copy of the thesis, including any required final revisions, as accepted by my examiners.

I understand that my thesis may be made electronically available to the public.

Statement of Contribution

The part of the results shown in this thesis has been submitted to the following journal, co-authored by myself, Stanley Fong (Ph.D. Candidate at the University of Waterloo), and my supervisor.

Kafle, M.D., Fong, S., and Narasimhan, S.. Active acoustic leak detection and localization in a plastic pipe using time delay estimation. *Applied Acoustics* - Under review.

I developed Prony's method and conducted all the experimental studies. Mr. Fong's contribution was on the development of mean-shift clustering method.

Abstract

Water distribution networks (WDNs) are critical infrastructure elements conveying water through thousands of kilometers of pipes. Pipes—one of the most critical elements in such systems—are subjected to various structural and environmental degradation mechanisms, eventually leading to leaks and breaks. Timely detection and localization of such leaks and bursts is crucial to managing the loss of this valuable resource, maintaining hydraulic capacity, and mitigating serious health risks which can potentially arise from such events. Much of the literature on leak detection has focused on passive methods; recording and analyzing acoustic signatures produced by leak(s) from passive piezo acoustic or pressure devices. Passive acoustic methods have received disproportionate attention both in terms of research as well as practical implementation for leak (or, bursts) detection and localization. Despite their popularity, passive methods have shown not to be reliable in detecting and localizing small leaks in full-scale systems, primarily due to acoustic signal attenuation and poor signal-to-noise ratios, especially in plastic materials. In this dissertation, an active method is explored, which uses an acoustic source to generate acoustic signatures inside a pipe network. A combination of active source and hydrophone receivers is demonstrated in this thesis as a viable method for monitoring leaks in water distribution pipes.

The dissertation presents experimental results from two layouts of pipes, one a simple straight section and another a more complex network with tees and bends, with an acoustic source at one end, and hydrophones at strategic locations along the pipe. For leak detection, the measured reflected and transmitted energy using hydrophone receivers is used to determine the presence of a leak. To this effect, new leak indicators such as power reflection and transmission coefficients, power spectral density, reflected spectral density, and transmission loss are developed. Experimental results show that the method developed in this thesis can detect leaks robustly and has significant potential for use in pressurized water distribution systems.

This thesis also presents a new framework for active method-based localization. Starting with a simple straight section for a proof of concept study and moving to lab-based WDNs, several methods are explored that simultaneously detect and locate a leak. The primary difficulty in detecting and estimating the location of a leak is overcome through a statistical treatment of time delays associated with multiple acoustic paths in a reverberant environment and estimated using two approaches: (i) classical signal decomposition technique (Prony's / matrix pencil method (MPM)) and (ii) a clustering pre-processing approach called mean-shift clustering. The former works on the cross-correlation of acoustic data recorded at two locations, while the latter operates on acoustic sensor data from a single location. Both methods are tested and validated using experimental data obtained from

a laboratory testbed and are found to detect and localize leaks in plastic pipes effectively. Finally, time delay estimates obtained from Prony's / MPM are used in conjunction with the multilateration (MLAT) technique and extended Kalman filter (EKF) for localization in more complex WDNs. This study shows that the proposed active technique can detect and reliably localize leaks and has the potential to be applied to complex field-scale WDNs.

Acknowledgements

First and foremost, I am deeply grateful to my advisor, Professor Sriram Narasimhan, for the guidance and support that let me grow as a researcher. His encouragement, support, and constructive criticism have always motivated me to do better. Without him, I would not be in the place where I am today.

I would also like to thank my Ph.D. defense committee members, Prof. Giovanni Cascante, Prof. Bryan Tolson, Prof. Sean Peterson, and Prof. Sunil Sinha, for giving me their valuable time to review my work and serve on my committee.

I should not miss this opportunity to acknowledge the funding support from the Natural Sciences and Engineering Research Council of Canada (NSERC) through their Strategic Project Grants program that made this research possible. A big thank you to Terry Ridgway, without whom experimental tests on would not have been made possible. I would also like to thank my colleagues and friends of Structural Dynamics, Identification and Control (SDIC) Lab; Ali, Kevin, Guru, Pampa, Jinane, Roya, Rajdip, Piyius, Stan, Nina, Dylan, Steve, Nick, Evan, and Dirk. You are all amazing, kind, and extremely talented, and I could not ask for better colleagues than you guys are.

Finally, I would like to thank my family and friends for their love, patience, and unconditional support during these years. I love you all!

Dedication

To my beloved parents, Indra Bahadur Kafle and Subhadra Bhattarai Kafle,
my wife, Akanchha Aryal,
and my siblings Akriti Kafle and Sushan Kafle.

Table of Contents

List of Figures

List of Tables

Chapter 1

Introduction

1.1 Overview

Pipes are vital to modern society, transporting and distributing fluids including drinking and wastewater [1]. They consist of several pipe segments connected through joints, valves, and other devices to control flow and pressure to form a water distribution network (WDNs). The total length of the pipelines worldwide is over 20 million kilometers today and with a growing population, they are being extended by 40-50 thousand kilometers each year [2]. Of primary interest in this dissertation are pressurized water pipes, which are the lifelines of our society, conveying drinking water to millions. But a significant portion of water is lost due to leaks between supply and delivery. A good distribution system should guarantee high water quality, sufficient pressure head, access to the water supply via hydrant in the event of a fire, properly laid and distributed pipe, and at least a meter away from sewer lines. But with aging pipelines, increasing breaks, and lack of proactive detection technologies, water leaks have resulted in deteriorating the quality of WDNs.

1.2 Motivation for Monitoring WDNs

Capital budget constraints, age, and environmental factors have all contributed to the deterioration of pipes, which manifest themselves as leaks, wall corrosion, tubercle growth, entrapped air pockets, etc. Such factors result in significant loss of water, repair expenses, loss of efficiency [3] and sometimes pose serious health risks when they allow wastewater intrusion to occur from compromised locations [4, 5]. Water leaks can be small that are

characterized by low to moderate flow rate, undetectable or hidden from the ground surface [6]. These hidden leaks, when left to run, can lead to pipe bursts over time due to strain and pressure. An example of such leak that can only be found using some monitoring methods is shown in Fig. 1.1, and if such leak is undetected, over time, it can be extremely large, e.g., [7], resulting in a flood, as shown in Fig. 1.2.

Figure 1.1: A typical leakage on main pipe and service pipe [6]

Figure 1.2: Leaking 30-inch main pipe near UCLA on July 29, 2014 [7]

The direct consequences of un-monitored and faulty WDNs result in the loss of a valuable resource. Even though Canada holds nearly 20% of the world's total freshwater resources, less than half of this (about 7%) is renewable, and most of it is fossil water trapped in lakes, underground aquifers, or in glaciers. Water is only useful when it is of a certain

quality, and in some locations, it has a longer cycling time and if heavily used, it can result in water scarcity. Because of this, even though the water resource is technically renewable, it can be virtually non-renewable [8].

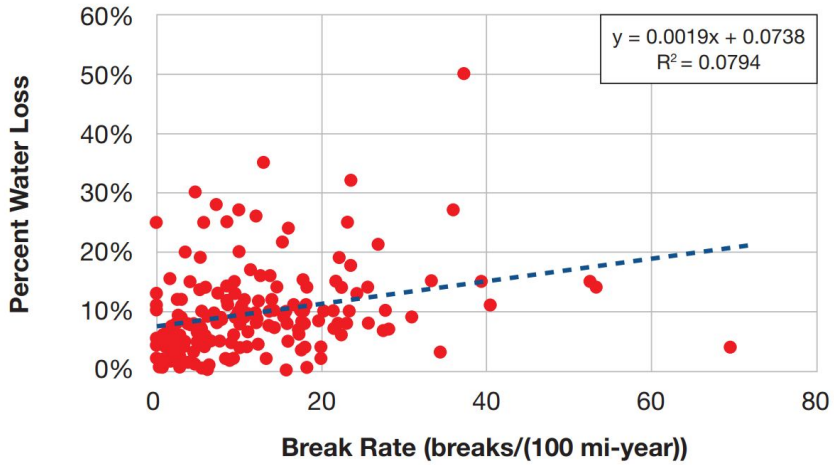

(a) Comparison of water loss in percentage with break rates [9].

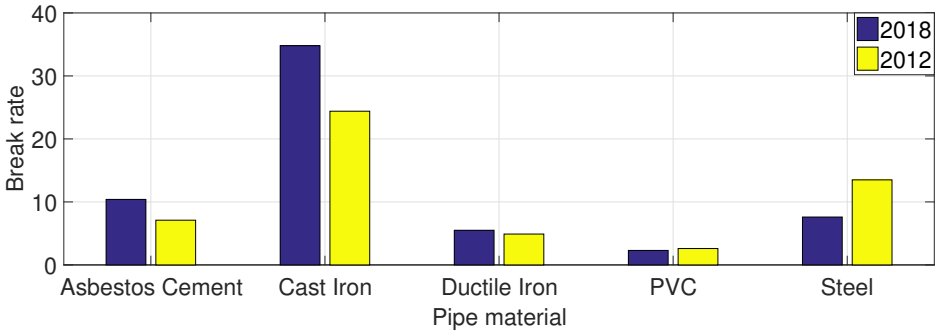

(b) Overall break rates (breaks per 100 miles/year) of 2012 and 2018 surveys.

Figure 1.3: Statistics on pipe break rate

It is reported that modern cities typically lose 20% of water from leaks which is a significant amount of loss [10]. Water loss estimates are about 9-30% in Europe [11], 43% in Malaysia and can be much higher in developing countries, e.g., 56% in Bangladesh [12]. In North America, unaccounted-for water is about 20-50% [13]. Figure 1.3a shows the correlation between water main break rates and water loss, with cast iron pipes associated with a higher break rate. Comparison of break rate in Fig. 1.3b shows that the breaks in cast

iron (CI) and asbestos cement (AC) based pipe increased in 2018 while decreased for PVC pipe. Also, the figure shows the most sought-after pipe material to be AC, CI, ductile iron (DI), and PVC [9].

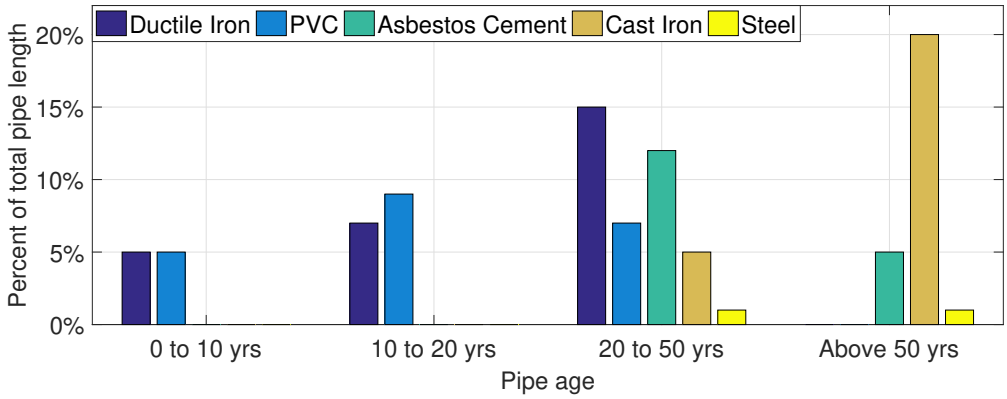

Figure 1.4: Comparison of pipe material by age

Most breaks in WDNs are attributed to pipe networks made of cast iron pipes, as more than 20% of the total pipe length in North America made of cast iron is over 50 years old. Figure 1.4 shows the age distribution as a percentage of the total length of all pipe materials. In recent years (0 to 10 years), DI and PVC are preferred material types and constitute about 5% of the total installed length. In total, about 240 thousand water main breaks occur per year, resulting in significant water loss. Globally, the estimated water loss is about 33.2 billion gallons per year which translates to a monetary value of about $40 billion annually [14].

Besides water loss, deteriorated infrastructure causes pressure drops in the system and leads to energy loss, creating energy inefficiency across the system [15]. Leaks in the system also may give rise to health risks due to the possibility of contaminants entering the water through leaks. Generally, the risk of contamination is low if sufficient internal pressure is maintained in the system. However, during events such as pipe breaks, pump shutdown or sudden changes in the water demand, low or negative pressure could result, which increases the probability of contaminant intrusion [16, 17]. This leads to a higher costs of water treatment and distribution. Therefore, pipe leakage monitoring and proactive rehabilitation of deteriorated infrastructure not only addresses the aforementioned problems but can also avoid unwarranted disproportionate failure consequences.

1.2.1 Water from the source to the tap

Water is collected from various sources such as underground water, wells, lakes, etc., and is transported and collected in water reservoirs. It is then treated and transported to pressure tanks located at high points throughout the distribution area. The height of the water tanks relative to the distribution area is what generates pressure. Finally, the water is distributed to subsections of WDNs using a combination of gravity and pumps through water distribution mains. In Ontario, Canada, the WDNs are designed to maintain a minimum water pressure of 140 kPa (20 psi) at the ground level at all points under maximum day demand plus fire flow conditions. The normal residential water pressure range between 50 and 70 psi and not less than 40 psi [18]. Municipal fire codes also require that the distance between any two fire hydrants be $122 - 182\ m$ between them [19].

For illustration, a water distribution network of district metering area (DMA) 11 [20] of the city of Guelph is shown in Fig. 1.5. This DMA uses 150 mm plastic pipe in the service line and 300 mm plastic pipe in the mainline. Red dots are the hydrant locations which are the connection point for firefighters to access the water supply.

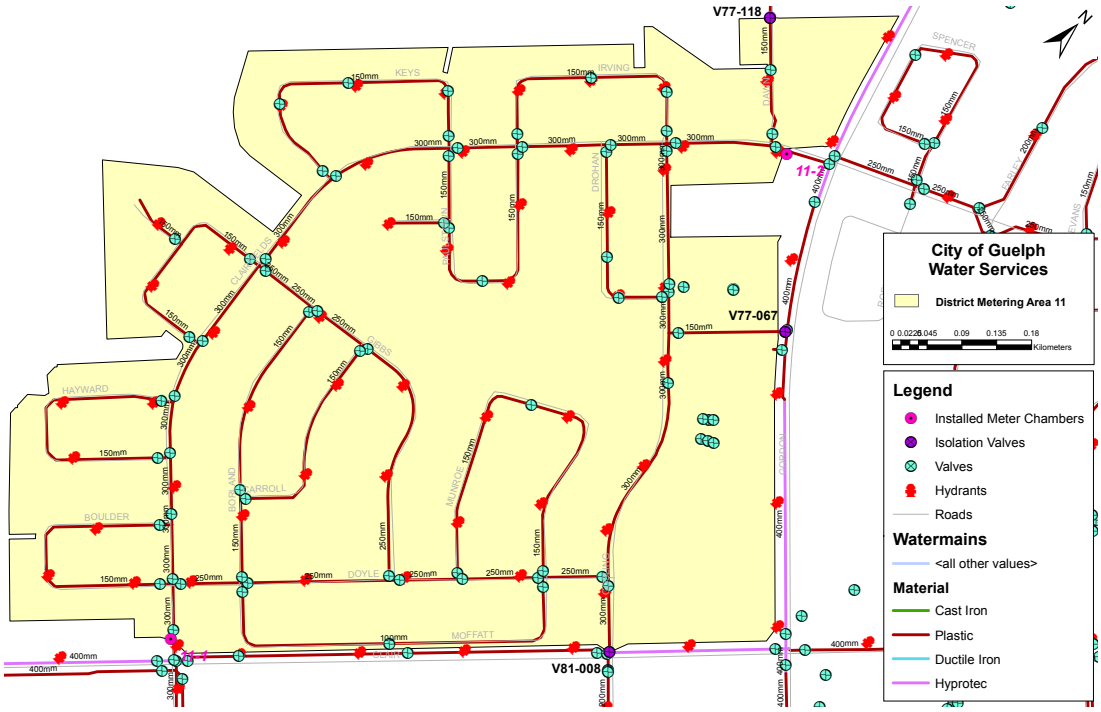

Figure 1.5: District Metering Area (DMA) 11 of City of Guelph Water Service [20].

1.3 Research Background

There are a variety of reasons for the occurrence of leaks and bursts in pipes. They can range from bad pipe connections, internal or external pipe corrosion, mechanical damage caused by surcharge load, ground movement, high system pressure, pipe age, winter temperature, and ground conditions [4]. The physical mechanisms that cause pipe failure are often complex and not well understood and therefore still an active research topic. Since pipelines are usually underground, little information is available about the modes of failure. Large breaks typically surface, so detecting them is relatively simple. However, leaks associated with low flow rate can remain underground, may not alter the hydraulic characteristics significantly, and hence can be extremely difficult to detect. Many leaks may run continuously before ever being detected. Hence, a significant amount of research and technology has been invested into pro-actively detecting leaks in buried pipes before they surface and result in catastrophic losses.

The efficient monitoring of events such as leaks requires reconsideration and evaluation of technologies with time. While reviewing monitoring methods, assessment is necessary based on factors such as system integrity, connectivity, and accessibility. Any changes to existing water distribution infrastructure must be done cautiously, so as not to disrupt the integrity of the system. Leak detection techniques in use today range from simple visual inspections to the use of sophisticated devices such as sonar, radar, acoustic listening devices, and robotics. Such methods are being used in conjunction with signal processing and data-driven statistical algorithms for leak detection. Purely data-driven techniques pose many challenges as they do not naturally obey physical constraints due to their limited observation of the environmental dynamics. Also, several model-based techniques exist which utilize global system-level information such as pipe pressure, flow data, etc. obtained from pipe network, but they tend to be fraught with assumptions and lack granularity. Also, the system models would need to be accurately configured and tested for similarity. Acoustic devices, which constitute the bulk of inspection devices in use today, include listening rods, noise correlators, and noise loggers, which listen to the acoustic signatures created by a leak and propagate through the water column. However, if the leak is small, or the pipe is non-metallic and large in diameter, the acoustic signals are heavily attenuated and generally narrow-band and of low-frequency [5, 21]. This makes the task of such passive leak detection difficult. Other non-acoustic-based methods include gas injection, ground penetration radar, thermal infrared imaging, etc. Such methods are not the focus of this dissertation and hence are not explored in detail.

A relatively new class of leak detection methods involves introducing active acoustic pressure waves into the pipe system. If there is a leak or variations in the geometry, material

properties, air pockets, etc., the acoustic wave is decomposed into reflected and transmitted components. The reflected wave due to leak, for example, can be used as an indirect means of detection [22]. Depending on the size of the leak and the frequency of the incident wave, part of the incident wave may radiate through the leakage orifice to the environment but a portion of the wave is reflected back towards the source, which can aid in leak diagnosis [23]. Such an active leak detection system can detect and locate leaks at large distances from the source generation point and are more robust to unknowns in the system (since the input energy is known with a great deal of confidence). Despite its promise, this technology has not been fully explored in the literature and hence the focus of this thesis is on exploring technology from both scientific and implementation standpoints.

Testing and validation of data is a key step to verify the effectiveness of such technology and are generally performed in a laboratory setting initially. Many WDNs laboratory setups are too simplistic and do not represent pipe geometry found in the field. Also, many laboratory setups also do not include common features such as elbows and junctions. While the initial testing of newer technology in a straight section is justified, it is also important to verify the method in more realistic representations, while taking into consideration main factors such as water pressure, leak size, and the pipe properties.

In this dissertation, an active leak detection approach based on active acoustics is explored as an alternative to the passive method to detect and localize leaks. An active source coupled directly to the water column generates acoustic waves of the desired frequency, which can propagate long distances and carry information of the pipe condition contained in the interaction between the injected waves and leak-induced signal changes. The detection and localization are premised on measuring the changes—from the baseline —induced in the acoustic field due to leak-induced impedance changes in a pipe. The main advantage of this method is that the driving frequency of such waves can be carefully selected so that it does not fall in the same frequency or amplitude regions as the background noise. Moreover, under the right conditions (e.g., power and frequency), these waves can travel long distances with minimal attenuation.

This research is both original and cutting-edge. So far, active acoustics has only been used by sea-going vessels or submarines for underwater navigation and ocean mapping using autonomous vehicles, underwater imaging, etc [24]. Moreover, despite the fact that the theory of acoustics waves is well developed, their principles haven't been explored for applications involving leak detection and localization. These gaps and the enormous potential of this technology motivate the proposed thesis work, which combines both experimental and theoretical studies in pursuit of active leak detection enabled using underwater acoustics.

1.4 Objectives

The overarching objectives of this research are as follows:

- Develop the theory and algorithms to enable an active acoustic monitoring system to detect and localize leaks in pressurized water pipes.
- Test and validate this system using laboratory experiments involving both single pipes and a more complex system of pipes.

While it is possible to identify already existing leaks in the system, the scope of this dissertation is limited to detecting newly developed leaks only with respect to a baseline. This approach relies on processing the transmitted and reflected parts of an injected acoustic signal, where several aspects of fundamental acoustics are explored. In this thesis, the use of hydrophones to measure acoustic data is motivated by the fact that, unlike surface mounted accelerometers, sound signatures have been shown to travel large distances inside water mains, even in traditionally challenging materials such as plastic.

1.5 Organization

The dissertation is organized as follows:

- Chapter 1 contains the introduction and research background on leak detection in pipelines, followed by the over-arching objectives of the dissertation.
- Chapter 2 presents the literature survey on the research topic. This is followed by a summary of the research gaps
- Chapter 3 presents the background on fundamentals of acoustics and signal processing. The acoustic characteristics and the equation of motion for plane waves are discussed; the reflection and transmission of plane waves and their relation to acoustic impedance are shown. Moreover, the basics of several signal processing methods that are used throughout the study are also presented.
- Chapter 4 describes the theoretical framework and methodology on several signal decomposition techniques that are applied directly to leak detection and localization. The theory on several multilateration techniques used for leak localization in a complex WDNs is also described.

- Chapter 5 shows the experimental results of leak detection and localization from a single pipe. For leak detection, the power transmission and reflection coefficient due to leak impedance is studied. Furthermore, two microphone techniques are explored to understand the resonance condition of the pipe and to estimate the transmission loss.

- Chapter 6 shows the experimental results for leak detection and localization in a network of pipes. Both active and passive methods are applied for leak detection and localization. Power transmission and reflection are studied for few leak scenarios.

- Summary and the contributions of the studies are outlined in Chapter 7 of this dissertation. Possible direction for future studies are also shown in this chapter.

- Additional important information is shown in the appendices. The list of publications is shown in A while the dimensions of the experimental setup are shown in Appendix B. Throughout the body of the dissertation, the schematic of the setup is used whenever necessary to discuss. So, some pictures of real WDNs and single pipe setup are shown in Appendix C. Few roots of *Bessel's Function* and its derivative are provided in Appendix D. Appendix E presents the theoretical background of techniques used for mitigating NLOS errors. Methods like the Extended Kalman Filter (EKF) and the maximum likelihood (ML) method are studied with the objective of improving the localization results. Appendix F shows some multilateration results conducted in a single pipe for proof of concept. Finally, a result from the high-frequency test conducted in WDNs is shown in Appendix G.

Chapter 2

Literature Review

2.1 Introduction

Leak monitoring techniques in water distribution pipes range from manual inspections to the use of various sophisticated acoustic, non-acoustic, modeling and data-driven techniques. The application of manual assessments of a pipe is made simply by trained inspection personnel relying on natural senses. There are methods relying on a hydraulic model where several parameters such as pressure, temperature, flow rate, etc., are continuously monitored, and interpretations are made using computer algorithms. Non-acoustic methods use special sensing devices (radar, tracer gas to name a few) and depending on the type of sensors and equipment methods to infer leak vastly differ. Finally, of specific relevance to this thesis are acoustic methods which rely on detecting and locating leaks based on the acoustic signals produced by the leak. Acoustic methods are by far the most popular in the literature and practice, but as explored in this thesis such methods are prone to environmental noise contamination and attenuation issues. Such issues can be overcome using active methods and constitutes the major focus of this thesis. This chapter shows the literature study of the available methods, and the research gaps are identified.

The chapter is organized as follows. Section 2.2 starts with a brief introduction of different types of leaks. The chapter then describes the overall methodology used for leak detection and expands on the state-of-art in Section 2.3. The acoustic method is the core topic of this dissertation. Hence, pertinent literature on both active and passive methods is presented in Section 2.4. From the literature study, the research gaps identified are outlined in Section 2.5, concluding with specific objectives in Section 2.6.

2.2 Background on Leaks

The most common form of water loss in WDNs occurs through leaks and bursts, although the latter are usually major events and are usually repaired immediately. Leaks could potentially run for long periods underground unnoticed, and hence are a major concern to utilities. Some of the known reasons for leakage occurrence are the poor installation and workmanship of the technician, poor material choice, pressure transients and fluctuations, excess water pressure, corrosion, vibration, and traffic loading, weather, and lack of proper maintenance [25, 4]. A bathtub curve as shown in Fig. 2.1 can be used to understand various phases in the life of a pipe [26]. The initial burn-in phase may have leaks resulting due to structural integrity of the pipe wall or due to improper installation (e.g., joints). The system may operate without any leaks during the usage phase unless there are failures attributed to excess pressure and its transients and other external factors. Most of the problems arise in the wear-out phase where the pipe deteriorates due to age and environmental stressors. Large breaks that typically surface in the burn-in and wear-out phase are rectified as they receive public attention due to the disruption caused by it. Smaller background leaks (characterized by low flow rate) are a key contributor to water loss as they cannot be easily detected and localized. Therefore, localizing the sections of the network to detect and locate these relatively small leaks as soon as they occur is central to leak reduction and minimizing water loss.

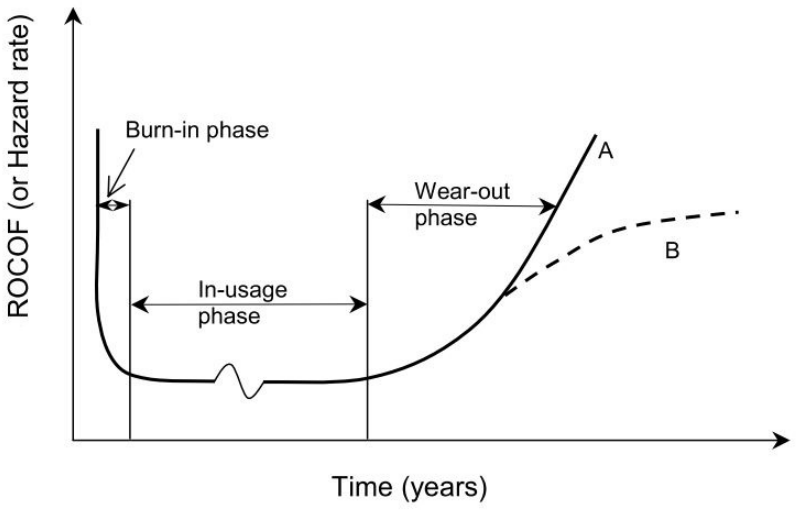

Figure 2.1: The life cycle of buried pipe explained by a bathtub curve [26].

The International Water Association (IWA) distinguishes the water loss occurrence into two major categories, real losses, and apparent losses [27]. Real losses are explained by the loss of water through pipes, joints, fittings, reservoirs, and tanks, while apparent losses are caused by inaccuracies related to customer metering, data handling errors, etc. Real losses, which are usually through leakage, are again broadly classified in three different groups as ([27]):

- background (undetectable) leaks—characterized by low flow rate (1 gallon per minute) may increase with increasing age of the network. These leaks are too small to be detected by conventional acoustic leak-detection equipment and run continuously until the leak size increases to the point that they can be detected;
- unreported leaks—characterized by moderate flow rate and may leak forever if not found with leak monitoring techniques; they are usually hidden from above ground view, and the duration of the leak depends on maintenance policies and effectiveness of the monitoring methods adopted by the utility.
- reported leaks—characterized by high flow rate generally last a short period of time (depending on how soon the corrective action is taken) as they surface easily and are visually evident and disruptive.

The British leakage management terminology differentiates reported with unreported leaks, as reported bursts and unreported leaks [27]. So, the substantial bursts that are more recognizable are termed as reported leaks, while small leaks that easily escape the attention of the public and water suppliers are identified as unreported leaks. In the United States, the term "reported, and unreported" are not used, and the distinction between leak and bursts are rather a personal choice. Unreported leaks account for large amounts of water loss and the objective of this dissertation is to develop technology which can reliably monitor for such leak events.

2.3 Classification of Leak Monitoring Methods

Literature on leak detection and localization is vast; some review papers [28, 4, 29] are included for reference. There is no commonly accepted classification scheme for leak detection methods, and literature is replete with many schemes. In one type of classification scheme from the literature, [30, 21, 29], leak detection techniques are broadly classified into three general categories as software based, non-technical, and hardware based method.

The detection approach usually associated with using a hardware device is defined as a hardware-based method that is further divided into acoustic and non-acoustic methods. On the other hand, software-based methods rely mainly on algorithms and models for detection. They also rely on additional data such as flow and system-related information. Non-technical methods do not require any instruments and are solely based on physical inspection. Other classification schemes [31] categorize the methods into direct and indirect methods. The direct method includes non-destructive and automated testing. Visual inspection, laser scanning, electro-magnetic, acoustic methods, etc., fall under this category. The indirect method employs techniques such as water audit, flow testing, etc. Recently, the classification of leak detection was further updated into passive and active methods[32], but the passive method in this study is defined to be a visual inspection or monitoring of sites based method while the latter is comprised of an analysis of acoustic and vibration signal, flow and pressure measurement. A review of existing classification schemes reveals a confusing and contradictory landscape and therefore a new and simple classification scheme is developed in this thesis as shown in Fig. 2.2.

There are also methods requiring no special instruments, which are known as non-technical methods. Patrolling along with the mains for visual signs, using soap solution on the pipe surface [33], inspecting, and listening to sound resulting from a leak all fall under this category. The accuracy of such inspection methods is greatly affected by inspector interpretation or the accessibility of mains, thus ruling out its application in buried pipes[29, 3]. Such methods are not the focus of this thesis and hence only some relevant ones are reviewed here.

2.3.1 Hydraulic based methods

Hydraulic based methods make use of an algorithm or a model to detect leaks, importantly they rely on hydraulic information such as flow data and water pressure to do so. Broadly, these methods can be further classified as model based and data-driven. Model based methods rely on using transient events with an attendant hydraulic model as the basis for leak detection. A leak is a hydraulic phenomenon and transient pressure waves can be useful to detect the presence of a leak[28]. An incoming transient signal interacts with a leak, resulting in wave reflections, which may alter the system flow and pressure response. The characterization of system flow and pressure provides leak-relevant information. Transients are generally generated by closing a valve for a very short time. The **inverse transient method (ITA)** involves modeling the hydraulic phenomena under transient events. The method is termed "inverse" as state variables such as pressure and

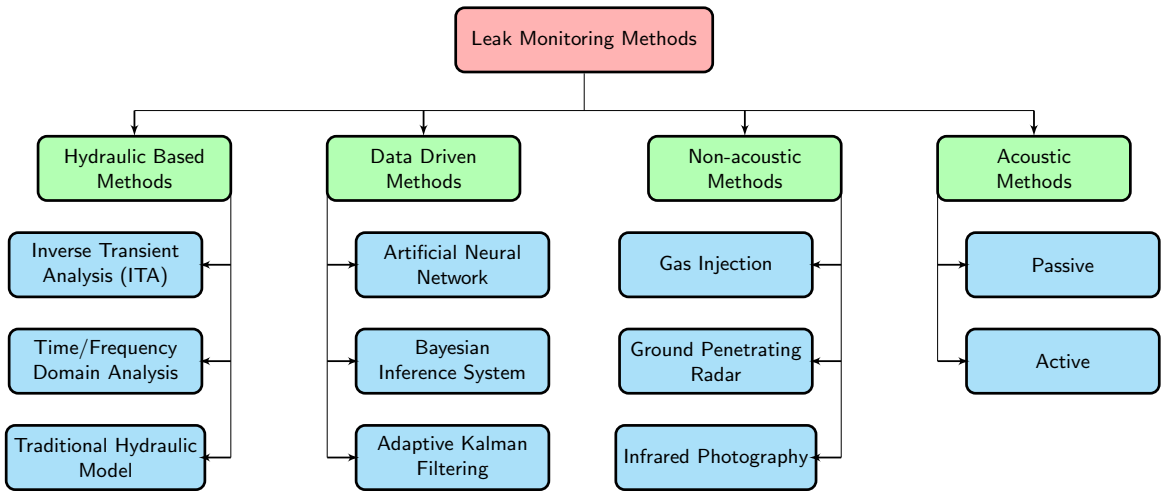

Figure 2.2: Classification of leak monitoring methods

flow are known/measured but other parameters such as pipe roughness and leak are unknown. The state variables are measured during a transient event and compared with measured data of system free from a leak. Then the leak is analyzed until the pressure traces of system with and without leak are acceptably matched. Then the system of equations are solved for other parameters such as the leak size and location [28]. Since its introduction by Liggett and Chan [34] as an extension of previous work by Pudar and Liggett [35], this method has been well researched, but experimental validation remains sparse. This method typically requires a good transient model as well as effective extraction of leak information which are usually buried in background noise. Also, as pipe complexity increases, this method becomes less reliable.

Time/frequency domain analysis first proposed by Jonsson and Larson for leak detection [36], probes acoustic pressure signals for wave reflection due to leakage (wave generated by sudden valve closure). The position of a leak is determined by measuring the arrival time and velocity of the reflected pressure wave. Silva [37] proposed a sparse wavelet method to detect negative pressure waves caused by pipe bursts on a single pipeline. The wave propagating at speed c, due to the pressure drop (Δp) was recorded by pressure transducers [37]. The data was then analyzed with an online computer program to provide leak information. In contrast to the time domain, frequency domain analysis looks for the amplitude change of the resultant transients due to a leak. Lee [38, 39, 40, 41, 42]

investigated several frequency based methods and impulse responses of the pipe system for leak assessment using transients generated by the sudden closure of a valve.

Traditional hydraulic modeling techniques for leak detection have improved due to the advances in supervisory control and data acquisition (SCADA) systems. Detection and localization of events in WDNs in which the hydraulic characteristics of the system are altered significantly have been treated using model based approaches, e.g., [43, 44, 45]. Such approaches have also been used in tandem with machine learning tools, e.g., bayesian learning, neural networks, support vector machines [46, 47, 48]. Sage [49] reported a successful implementation of a hydraulic model based on leakage demand in a number of district metering areas (DMA). The difference between field metered inflow and modeled demand (estimated consumption) provided information of leakage demand. Wu [43] later developed a pressure dependent leak detection model and demonstrated the usefulness of this model in a district metered water system in the UK. The method seemed to be effective in detecting leaks regardless of the pipe material. However, model-based approaches typically entail complex modeling procedures, generating likely leak scenarios, and offline calibrations, rendering them too cumbersome for implementation in real-world complex WDNs.

2.3.2 Data driven methods

Data-driven models combine monitored data with other tools such as artificial intelligence to identify leaks. For pipe leak detection, several machine learning methods such as support vector machines (SVM), neural networks and Bayesian learning are available and the algorithms associated with these methods are well established. Mounce [47] combined **artificial neural network** with a fuzzy inference system to detect pipe bursts and used field data from several DMAs to validate their method. However, this method requires significant historical data to train the neural network which is not always available, hence limiting its application. Ye and Fenner [44] developed a leak detection method based on Kalman filtering on measured flow and pressure data at a DMA level. A model for normal water usage was developed using **adaptive Kalman filtering** and the residual of the filter which is the difference between the measurement and filtered estimate presented an estimate for loss. The benefit of this method over the artificial neural network is that this method does not require a large amount of training data. The **Bayesian inference method** provides magnitude and location for leaks, along with the uncertainties associated with probable leak events [4, 46]; however, this method can be computationally intensive and may not be conducive to automation.

2.3.3 Non-acoustic methods

Researchers have tried several approaches to detect leaks using non-acoustic methods such as **gas injection** infuse industrial gases such as hydrogen into the pipe and look for gas traces using detectors [50]. The location of a gas trace provides evidence and location of leaks. This method, however, is costly and not feasible for long pipes. Moreover, gas being less dense than water, cannot be used to detect leaks which are located at the bottom of the pipe. Similarly, **ground penetration radar** is a non-destructive method that transmits high-frequency electromagnetic waves underground. The reflected wave is studied to infer the presence of underground pipe leaks[51]. This method though cannot be used in cold climates or in saturated soil [52]. In addition to these methods, **thermal infrared imaging** is also a non-acoustic method for leak detection that measures emitted IR radiation from the pipe system. A thermal camera can be used to obtain thermal contrast in IR images and that is the basis of this detection method[53]. This method also suffers from many challenges such as weather, soil and surface conditions. The image-based analysis combined with a neuro-fuzzy algorithm is also proposed to extract a crack feature of an underground pipe, but it is targeted for sewer lines [54].

Most of the water leak detection and localization methods are developed on the foundation of acoustic wave generation and propagation. The upcoming section differentiates the class of detection methods within this branch and shows some of the methods applied for monitoring water leaks.

2.4 Acoustic Methods

Acoustic methods for leak detection have been studied since the 1930s, and their application in pipe networks has shown that leaks from gasoline and liquid-filled pipelines can be identified and localized well [55]. A good classification scheme for acoustic methods is not available in the literature; for the purposes of this dissertation, they are categorized into the two broad categories of passive and active methods, as shown in Fig. 2.3. Active methods involve providing external stimuli, while passive methods do not rely on such external stimuli and use acoustic signatures generated by the leak.

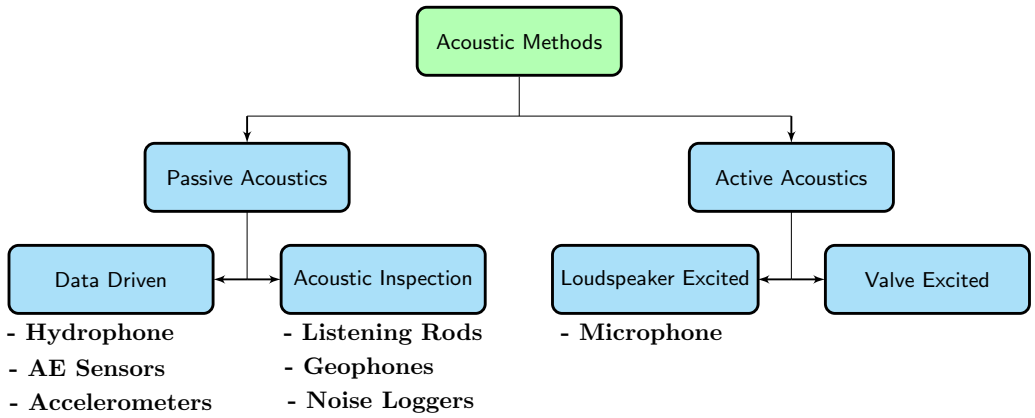

Figure 2.3: Classification for the acoustic class of methods

2.4.1 Passive methods

Detection

In the passive acoustic leak detection method, instruments such as listening rods, geophones, leak correlators, noise loggers, etc. are employed. For instance, listening rods detect the sound produced by a leak, which is generally between 20 Hz to 250 Hz and hence in the audible range of the human ear. Geophones are built on the same idea as listening rods. The drawback of these methods is that they depend on the expert user to infer from data and rely solely on the acoustic properties of the leak. Hence they present difficulties in identifying small leaks, especially when the pipe diameter is large.

Other passive methods work by remotely monitoring and extracting leak-induced signatures from vibrations or sound produced by the leak leaving the orifice using sensors (accelerometers or hydrophones) distributed strategically within a WDN. As the name implies, passive methods do not inject additional energy into the system and rely on measurements emanating due to pressure fluctuations, flow conditions, or acoustic noise induced by water leaving the pressure boundary, either with or without models, to determine the presence of leaks and bursts [43, 44, 56, 57]. Such passive methods have also been employed on plastic pipes, e.g., [58, 59, 60]. However, the detection and localization accuracy of passive methods depends on a high signal-to-noise ratio (SNR), pipe material, or the amount of a priori knowledge available, such as speed of sound in the fluid-pipe system. Passive methods which rely solely on leak-induced acoustic signatures suffer from attenuation and noise contamination issues. In most cases manually labeled data or expert knowledge is

required to delineate leak presence from other sources, which makes such methods difficult to employ in autonomous settings or in large-scale monitoring applications.

Khulief [23] used a hydrophone to address the feasibility of in-pipe acoustic measurement by conducting an experimental study in a rig that can simulate water transmission in a pipeline with different leak sizes, flow rates, and pressures, to characterize acoustic signatures of the leak. From a study conducted in 200 m long PVC pipe, Hunaidi and Chu [19] concluded that leak type, flow rate, pipe pressure, water temperature, wave propagation velocity, and attenuation rate determines the frequency content of acoustic leak signal. Ahadi and Bakhtiar [55] captured leak signatures by monitoring the short-time Fourier transforms (STFT) of the acoustic emission (AE) signal. This was followed by the processing of signals to localize leaks in the time and frequency domains. Jin [61] applied a wavelet-based denoising optimization technique with least squares support vector machine (LS-SVM) to deduce the size and condition of the leak. Butterfield [62] used vibroacoustic emission (VAE) produced by the leak to investigate signal processing techniques to quantify the leak flow rate. Out of several signal processing techniques, a strong correlation between the signal root mean square (RMS) and the leak flow rate was found. This was then used to develop a flow prediction model. It was also found that VAE signal is strongly influenced by surrounding media which can affect accuracy. Li [63] used acoustic signals obtained using AE sensors, applied kernel principal component analysis (kernel PCA) to reduce the dimension of the features, and used a support vector machine (SVM) classifier on generated features to determine the leakage level.

While these methods appear promising and can produce results with high accuracy for noisy leaks, with PVC and larger diameter pipes there can exist large interfering signals from external sources as well as excessive signal attenuation [64], which could limit the application of passive methods. Moreover, in noisy environments with frequencies similar to those induced by the leak, reliable recovery of the leak vibration signatures from passive acoustic data can be extremely difficult.

Localization

Leak localization methods in the literature (in the context of passive acoustic methods) are based on the cross-correlation technique [65, 50, 56, 66, 67]. This involves estimating time-delays directly from the cross-correlation function between two measured signals (acceleration or acoustic pressure), which can be achieved using various time-delay estimation techniques [65], provided the wave speed c and distance between the two sensors is known. As shown in Fig. 2.4, if the distance and the wave speed are known, using time delay

obtained from the cross-correlation function, the position of the leak can be obtained from one of the sensor location using:

$$\tau_{max} = \frac{L_2 - L_1}{c} \tag{2.1}$$

$$L_1 = \frac{D - c\tau_{max}}{2} \tag{2.2}$$

where, L_2 and L_1 are the positions of the leak relative to the sensor points, D is the distance between the two sensors and c is the speed of leak sound. If τ_{max} is known from the measured data, then the position of the leak can be estimated.

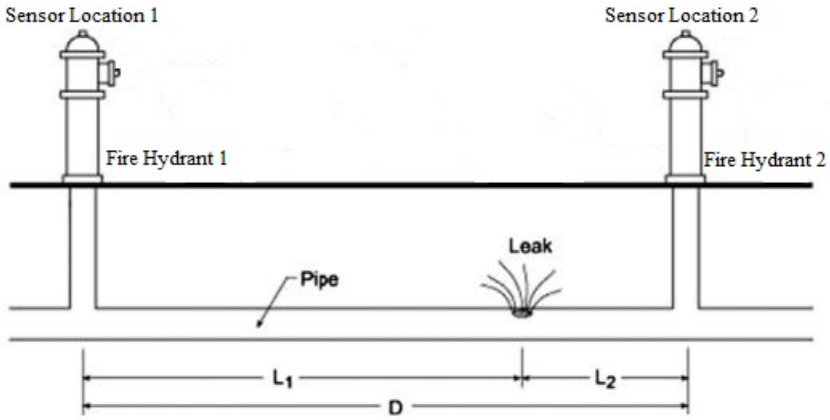

Figure 2.4: Principle of LeakFinderRT [56]

Hunaidi [56] developed a low-cost and easy-to-use system named "LeakfinderRT" which is based on an enhanced cross-correlation function. The enhanced cross-correlation function [56] that was presented uses the inverse Fourier transform of the cross-spectral density (CSD) function, instead of the shift-and-multiply method in the time domain. This system determines the time delay τ_{max} which corresponds to the peak of the cross-correlation function, based on the location of the leak relative to the sensor, and the propagation velocity of sound in the medium.

Gao [5] used both hydrophones and accelerometers to measure acoustic/vibration signals on either side of the leak and applied correlation techniques in order to locate it within the pipe segment. The theoretical results were compared with experimental data, which showed that hydrophones were effective for small signal-to-noise ratio (SNR), while accelerometers provided a sharper correlation peak. The same team [67, 5, 66] later proposed the generalized cross-correlation (GCC) method [65, 68, 69, 70, 71] to improve the time delay estimate

through band-pass filtering and pre-whitening the signals to sharpen the leak-induced peak in the cross-correlation function.

Ozevin and Harding [72] used a conventional acoustic sensor known as R6 mounted on a pipe to record waveforms generated due to a leak. They were able to determine arrival time difference using correlation and introduced geometric connectivity in order to pinpoint the wave propagation trail to the sensor locations. They also showed the signal attenuation curves in a 2.54 cm PVC pipe by recording the amplitude every 0.1 m up to 0.6m as shown in Fig. 2.5. The figure shows that acoustic waves attenuate from 80 dB to 40 dB in just half a meter.

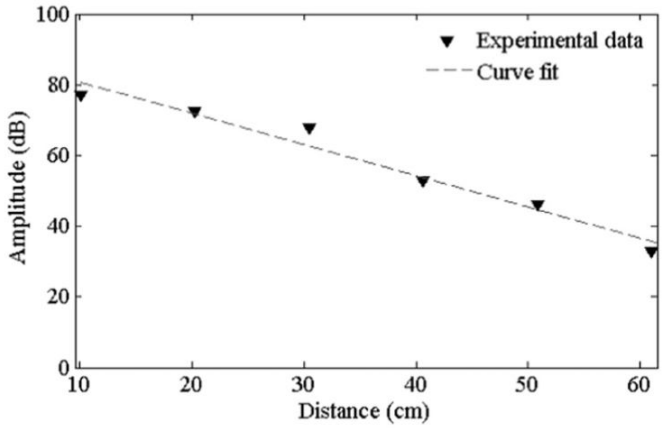

Figure 2.5: Wave attenuation curve of PVC pipe [72]

2.4.2 Active methods

Detection

Active methods largely overcome the problem of low SNR found in passive methods by injecting an acoustic signal into the system and recording the resulting acoustic responses from the system. Active methods do not rely on acoustic energy produced by the leaks themselves; rather, they probe the changes produced by leak(s) to the injected energy/signals. The basic principle in active acoustic methods is that a portion of injected acoustic energy (in the appropriate frequency range) is reflected where impedance changes occur and such information can be probed to detect leaks present in a pipe. Further analysis of the recorded signal is performed to acquire information about the system's condition.

For example, these studies have utilized active energy sources such as portable pressure wave maker [73], solenoid valves [40, 10, 74, 75, 76], acoustic transducers [22] and low frequency mechanical actuators [77].

Active methods have also been applied to assess the condition of pipes and valves. For example, in [78] the authors used wave speed to indicate pipe deterioration and in [79], the authors developed a spark transient pressure wave generator to detect thinner-walled pipe sections in a pressurized copper pipe. Despite the scarcity of literature on active leak detection, results generally show that active methods can be designed to be robust to ambient and background noise interference [80].

There are studies where the acoustic method has been used to measure airway dimensions for medical applications [81, 82]. In these studies, acoustic pulses were sent into human airways such as lungs and resulting reflections were used to reconstruct the area-distance function (impedance and area profile of the object under investigation). In such studies, pressure sensitive transducers were used to record the impulse and the reflections from the emitted source pulses and the resulting signals were analysed to reconstruct the profile of the object.

Active sources employing loudspeakers have been used in these studies [83, 82, 84, 80], but in air-filled tubes and ducts, not in water-filled pipes. Hydraulic impedance based method was also used for a hypothetical branched pipeline system having both leakage and a blockage; a water hammer was generated by rapidly closing a control valve [74]. [85] conducted numerical studies to explain the properties of acoustic waves in fluid-filled pipes, including dispersion, multi-path behavior, and various factors affecting the propagation range and distribution of energy.

A pulse signal and its reflection have also been used to measure the input impulse response of wind instruments [86]. Sharp [84] used pulse signals and recorded the resultant reflections to measure the input impulse response of an air-filled tube to detect the position and size of the orifice and to evaluate the input impedance of the system. The pulse was amplified by a stereo amplifier and a compression driver loudspeaker with a microphone attached to tube to record the reflections.

Louati and Ghidaoui [85, 87] described the properties of high-frequency acoustic waves in a water-filled pipe analytically. In the first part of their study, dispersion and multi-path behavior of the wave are reviewed, while the factors affecting the propagation range and distribution of energy are later reviewed. Their study shows theoretical and numerical results obtained using high-frequency waves in in-viscid, stagnant flow in a single pipe system and develops a two-dimensional wave model. For a pressure wave with a first radial mode ($n = 1$) as shown in Fig. 2.6, M1 is excited if $\frac{w\,R}{c} \geq 3.83$. This means the classical

1D wave theory is no longer valid above the cutoff frequency [85] which is computed using Eq. 2.3.

$$f > f_1 \approx \frac{3.83}{\pi} \frac{c}{D} \tag{2.3}$$

where c and D are the speed of sound in the fluid and diameter of the pipe.

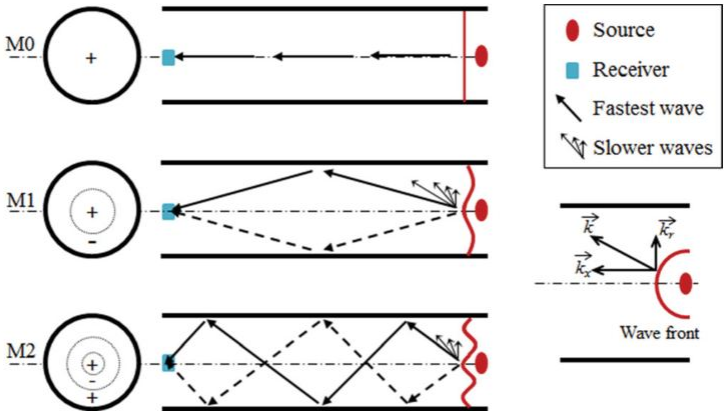

Figure 2.6: Wave direction and modes [85]

Nguyen [75] used a customized valve connected to the pipe to generate an inverse repeat pseudo binary sequence (IRS) signal and studied the impulse response function (IRF), in order to localize a leak. The basic idea is that any irregularity inside the pipe will will result in a reflection of the generated wave, which can be recorded using a pressure transducer placed inside the pipe. Both numerical and experimental data are used to verify this technique and their results showed that the estimated IRF provides accurate leak localization and is sensitive to small leaks as well. However, experimental results comparing leak to no-leak signals were not shown. In general, active methods hold significant promise for leak detection and localization applications, however they have not yet been fully explored, especially using sonar acoustic devices. Experimental studies on active leak detection in pipes are relatively scarce compared to passive methods and those that exist rely on creating low-frequency pressure transients, e.g., [40, 41]. Hence, a large literature gap has been identifies during the exploratory phase of this thesis, which motivated the current work.

Localization

For passive approaches, the leak is assumed to constitute the dominant excitation source and hence the first peak in the correlation function corresponds to the time (difference) taken for the leak-induced acoustic signal to travel from the source to the two sensor locations. However, for the active case, the main source of excitation comes from the active source, and hence the first peak is not associated with the leak, but rather the time for direct transmission of the induced excitation between the two sensors. This phenomenon can be observed in Fig. 2.7 where, (a) shows the cross-correlation function due to leak only and (b) shows the cross-correlation function of both leak and the actuator; the first peak is associated with the signal from the actuator. This results in added complexity to the

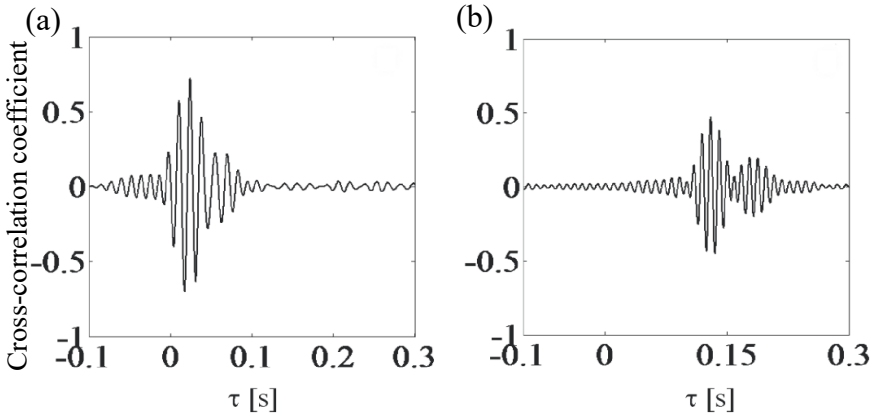

Figure 2.7: The cross correlation function obtained due to: (a) leak only; (b) both actuator and leak [88]

time-delay estimation problem in the active case as delineating leak-induced time delay and the direct transmission time associated with the energy from the active source in the cross-correlation function can be difficult. Generally, the acoustic energy produced by the active source will mask the leak-induced acoustic signature [88, 77]; it is important to note here that the aforementioned study [77], while presented an active approach, focused on the determination of wave speed, not on the problem of leak detection and localization.

Wang et al. [89, 76] used the matched-field processing (MFP) method to localize a leak via a 1D search of leak location, as MEP uses the shape of the frequency response function (FRF) of the viscoelastic pipe. The experiment conducted at two locations used a long single-section pipe, which is driven using a transient generating valve, and the resulting pressures are measured using hydrophones. However, this method needs a physical model (viscoelastic and K-V model coefficients) to localize leaks accurately.

There are also studies that have proposed cepstrum (inverse Fourier transform of the logarithm of the Fourier transform) as a powerful alternative to the correlation method to detect transient events [90]. This tool has been shown to work well in a single straight pipe by extracting the time of reflection instances [91, 92, 90, 75] and obtaining leak distance from the time delay. Cepstrum combined with the cross-correlation technique has also been studied in a T-junction system to identify local singularities and harmonics within the signal history [93]. However, the ability to discern features using this technique is compromised in complex and large WDNs. Recently, a new localization method based on the time-reversal technique has also been proposed, but only a numerical case study has been shown [94].

Wave speed (c) has a significant effect on localization accuracy, both for the active and the passive method. A vast majority of studies in the literature utilize theoretical values of c as opposed to estimates obtained from in-situ measurements. Wave speed is a function of the pipe properties such as thickness, radius, and material properties, which in turn depends on the manufacturing processes and the level of degradation, which are difficult to determine *a priori*. In plastic pipes, in situ measurements are further exacerbated due to the high level of attenuation presented by the pipe material. As pointed out in [77], a 10% error in the estimate of c could translate to as large as 5% error in the leak location estimate. Muggleton et al. [95] experimentally determined the fluid-borne wavenumber in a buried pipe and validated their results using theoretical predictions. In-situ measurements of wave speed and attenuation in viscoelastic pipes were performed in the following studies [96, 97], however, these studies do not consider the problem of leak detection or localization. Some studies use time-frequency maps, e.g., [96], as a tool to estimate frequency-dependent statistical estimates for speed. However, time-frequency maps produced from experimental data tend to be very noisy and difficult to process directly.

Multilateration (MLAT) is a technique for determining the position of the source based on the times of arrival of waves. It assumes that the speed of the wave from the source to the receivers is already known. The receivers are at known positions and have a synchronized clock. The MLAT techniques explored later in the thesis are the time of arrival (TOA) and the time difference of arrival (TDOA) [98, 99]. These techniques, for scenarios like the line of sight (LOS) and non-line of sight (NLOS), are the basis of localization in a global positioning system (GPS). The use of such methods to locate leaks in WDNs is new field and there is no directly relevant literature on this topic.

2.5 Research Gaps

The identified gap areas in the current state of leak detection and localization in WDNs and the expected contributions of this thesis are summarized below.

1. The most sought-after leak detection technique, i.e., passive method, relies on leak sound propagation through the walls and the fluid medium. In real-life networks consisting of multiple sections and junctions, detection and localization accuracy with this method may suffer because of the signal attenuation and noise contamination issues, especially in plastic pipes, which are associated with high loss factors. Such issues have not received the attention they deserve in the literature.

2. Most active methods in the context of leak detection and localization have thus far relied on using solenoid valves to generate pressure waves. Such methods are not easy to deploy in the field and create large turbulences in the system, which negates many of the assumptions made in linear wave theory. Despite this, these methods continue to be studies without addressing these fundamental problems.

3. Theories on acoustic waves have been developed and have been applied in air duct related experiments and medical applications, however, they have not been studied in fluid filled pipelines for leak detection and localization. As a result, the applicability of this vast theoretical foundations to this application is yet to be demonstrated. There is little work performed on low-frequency acoustic wave reflection and transmission due to leaks in water mains and distribution networks.

4. A system defect such as blockage, leak, or variation in the cross-section area results in changes to the overall impedance of the system. The impedance change results in the reflection of wave. In a water-filled pipe, studies connecting geometric changes to impedance have not been fully explored. There are few studies, for example, to determine the size of the orifice in an air-filled open waveguide; but not for leak detection in pressurized pipes.

5. The cross-correlation method remains the most used technique to estimate the time delay for localization, and the first peak is associated with the leak. However, if the system is driven by external stimuli as discussed earlier using Fig. 2.7, then the traditional process of extracting time delay will not suffice, but has not been treated in any detail in the existing literature.

6. Much of the leak localization literature focuses on simple straight pipe sections to validate their methods of localization. Furthermore, they utilize pipes not representative of full-scale systems, in geometry or in complexity. While understandably, mimicking field scale in laboratory environments is not practical, to the author's knowledge, experimental studies for localization on set ups with multiple junctions, multiple pipe sections, hydrants and end-caps have also not been attempted. Needless to say, this means localization in multi-path environments have not been studied.

2.6 Specific Objectives

In an attempt to address some of the gap areas, the specific research objectives of this thesis are as follows:

1. To develop a theoretical and algorithmic framework for monitoring leaks in water filled pressurized pipes based on acoustic wave propagation, with specific emphasis on the active acoustic method.
2. Test and validate the developed approach using experiments in both single pipe sections and more complex WDN laboratory testbed, which include:
   (a) the development of robust leak detection indicators by comparing with a baseline;
   (b) developing a methodology to estimate leak-induced time delays in multi-path acoustic environments for localization;
   (c) developing new localization methods to work in multi-path environments; and
   (d) validation and evaluation of the results of the methods developed in the test bed.

Clearly, not all the research gaps identified earlier will be addressed in this research; however, it is anticipated that this thesis will attempt to resolve a few major ones with the expectation that future studies will attempt to build upon this work to solve the remaining gap areas.

Chapter 3

Background Theory

Acoustic methods for leak detection rely primarily on analyzing sound waves traveling through the water column inside the pipe. Sound is produced as a result of pressure variations or oscillations generated by vibrating surfaces or turbulent fluid flow. A sound wave requires elastic material support to propagate through a medium. This elastic material support can be explained using a distributed mass-spring system in which the displacement of an element due to a vibrating surface results in the propagation of disturbances throughout the medium, which is how a wave propagates [100]. In other words, compression and rarefaction due to the vibrating surface is passed from one point to the other through the elastic nature of the material support.

This chapter will establish the background on the fundamentals of acoustic wave and basics on signal processing techniques. Plane-wave theory, its relation to the impedance of a system will be explained, as well as how—with known system impedance and wave properties—a leak may manifest in a pipe will be described. This chapter begins by deriving the acoustic wave and pressure equations, which are then explained in terms of impedance. This chapter also presents the mathematical formulations for impedance under different pipe conditions, such as closed ends and sections with branches. Attenuation of signal energy is a significant issue in leak diagnosis, which is overcome to a large extent using the active method. The frequency-dependent attenuation of a signal is also discussed in Section 3.2.1.

3.1 Acoustic Wave Characteristics

The field of acoustics deals with the study of mechanical waves in material mediums such as gases, liquids, or solids. Mechanical waves in solids fall into three categories, namely shear, Rayleigh, and Love waves [101]. Rayleigh and Love waves travel on the surface, while shear waves depend on the elastic deformation of the medium. In liquids and gases, there is no shear, so waves propagate only by compression and rarefaction. At an interface between a solid and liquid, a surface wave is generated. A wave of pure tone (single frequency) is characterized by:

- Local amplitude of each particle: Acoustic pressure expressed in Pascals (Pa) is the quantity often used in underwater acoustics. Amplitudes are described by the maximum pressure, p_M, or root mean square (RMS) pressure, p_{rms}. For a wave of mono-frequency, p_{rms} is related to p_M by Eq. 3.1.

$$p_{rms} = \frac{p_M}{\sqrt{2}} \tag{3.1}$$

- Frequency (f): Frequency is the number of cycles per unit time or simply number of cycles per second and is expressed in Hertz (Hz).

- Time period (T): The period is the duration that a wave cycle takes to pass a fixed point. It is related to the frequency by Eq. 3.2:

$$T = \frac{1}{f} \tag{3.2}$$

- Speed of propagation (c_f): The speed of propagation is the speed at which a wave travels in a medium. In a free field, the speed of sound is a function of fluid density, ρ, and bulk modulus, B_f, and is expressed as Eq. 3.3:

$$c_f = \sqrt{\frac{B_f}{\rho}} \tag{3.3}$$

  In seawater, the wave speed is approximately 1500 m/s, and depends on pressure, salinity, and temperature. In air, the wave speed is 343 m/s at 20^0C and 1 atm pressure.

- Wavelength (λ): It is the distance travelled by the wave in one cycle. Wavelength is a spatial correspondent to time periodicity and is expressed in units of length, such as meters (m). Speed of propagation, frequency, wavelength, and time period are related to each other by Eq. 3.4.

$$\lambda = c_f \, T = \frac{c_f}{f} \tag{3.4}$$

- Wave number (k): Wavenumber k is the spatial frequency (a measure of how frequent the sinusoidal components of the structure repeat per unit distance) of a wave measured in radians per unit distance or cycles per unit distance. The relationship between k, λ, f and c_f is shown in Eq. 3.5.

$$k = \frac{2\pi}{\lambda} = \frac{2\pi f}{c_f} = \frac{\omega}{c_f} \tag{3.5}$$

  where, ω is the angular frequency.

3.2 Wave Equation of Motion

The wave equation in an one-dimensional space can be derived using several physical analogs, e.g., a vibrating string. For two-dimensional space, the motion of a thin membrane such as a drum-head that is stretched uniformly in all directions can be used to motivate the mathematical formulation. If the tension per unit length, T is uniform at all points and the deflections $u(x, y, t)$ during motion are small, then according to Fig. 3.1, the net vertical forces in the x-axis and y-axis, respectively, are shown in Eq. 3.6.

$$\begin{aligned} T\Delta y(sin\beta - sin\alpha) &\approx T\Delta y(tan\beta - tan\alpha) \\ &= T\Delta y(\frac{\partial u}{\partial x}|_{x+\Delta x, y_1} - \frac{\partial u}{\partial x})|_{x,y_2}) \\ T\Delta x(sin\beta - sin\alpha) &\approx T\Delta x(tan\beta - tan\alpha) \\ &= T\Delta x(\frac{\partial u}{\partial y}|_{x_1, y+\Delta y} - \frac{\partial u}{\partial y})|_{x_2,y}) \end{aligned} \tag{3.6}$$

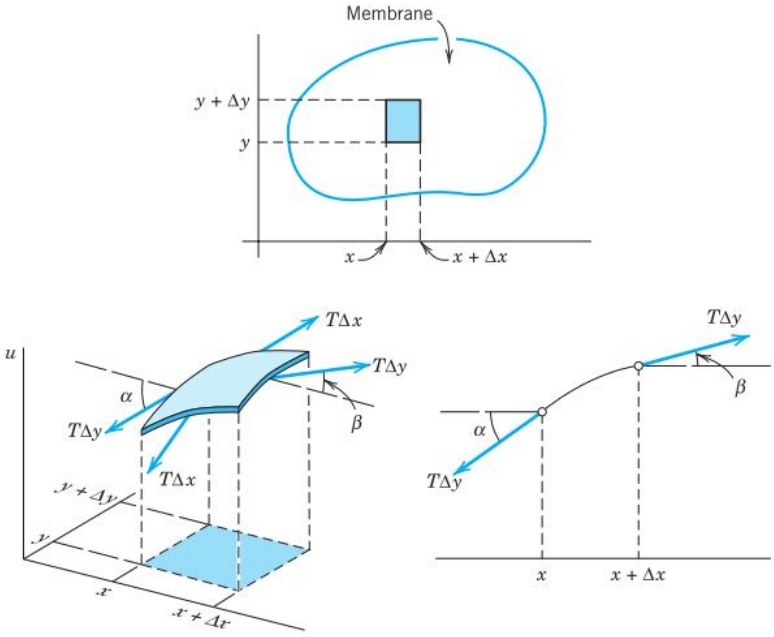

Figure 3.1: Forces acting on the stretched membrane [102]

Applying Newton's law for equilibrium and summing the forces in the two directions [102],

$$\frac{\partial^2 u}{\partial t^2} = \frac{T}{\rho}\left[\frac{\frac{\partial u}{\partial x}|_{x+\Delta x,y_1} - \frac{\partial u}{\partial x})|_{x,y_2}}{\Delta x} + \frac{(\frac{\partial u}{\partial y}|_{x_1,y+\Delta y} - \frac{\partial u}{\partial y})|_{x_2,y})}{\Delta y}\right] \tag{3.7}$$

$$= c^2\left(\frac{\partial^2 u}{\partial x^2} + \frac{\partial^2 u}{\partial y^2}\right) \tag{3.8}$$

$$= c^2 \nabla^2 u \tag{3.9}$$

where $c^2 = \frac{T}{\rho}$ and ∇^2 is the Laplacian operator.

To derive the equation for normal modes, the equation of motion shown in Eq. 3.9 is assumed to have solutions of the form of,

$$\boldsymbol{u} = \boldsymbol{\Psi} e^{i\omega t} \tag{3.10}$$

where $\boldsymbol{\Psi}$ is a function of only the position. Substituting Eq. 3.10 into Eq. 3.9 and the wave number (k) gives the Helmholtz equation [103] shown in,

$$\nabla^2 \boldsymbol{\Psi} + k^2 \boldsymbol{\Psi} = 0. \tag{3.11}$$

Cylindrical coordinates are very useful when working with pipes due to their typical circular cross-section. The Helmholtz equation can be expressed in cylindrical coordinates as, [103]

$$\frac{\partial^2 \boldsymbol{\Psi}}{\partial r^2} + \frac{1}{r}\frac{\partial \boldsymbol{\Psi}}{\partial r} + \frac{1}{r^2}\frac{\partial^2 \boldsymbol{\Psi}}{\partial \theta^2} + k^2 \boldsymbol{\Psi} = 0. \tag{3.12}$$

Applying separation of variables by assuming $\boldsymbol{\Psi} = \boldsymbol{R}(r)\boldsymbol{\Theta}(\theta)$ and substituting into Eq. 3.12 results in,

$$\boldsymbol{\Theta}\frac{\partial^2 \boldsymbol{R}}{\partial r^2} + \frac{\boldsymbol{\Theta}}{r}\frac{\partial \boldsymbol{R}}{\partial r} + \frac{\boldsymbol{R}}{r^2}\frac{\partial^2 \boldsymbol{\Theta}}{\partial \boldsymbol{\theta}^2} + k^2 \boldsymbol{R}\boldsymbol{\Theta} = 0. \tag{3.13}$$

Multiplying the above equation by $r^2/\boldsymbol{\Theta}$ and re-arranging gives,

$$\frac{r^2}{\boldsymbol{R}}\left(\frac{\partial^2 \boldsymbol{R}}{\partial r^2} + \frac{1}{r}\frac{\partial \boldsymbol{R}}{\partial r}\right) + k^2 r^2 = -\frac{1}{\boldsymbol{\Theta}}\frac{\partial^2 \boldsymbol{\Theta}}{\partial \theta^2}. \tag{3.14}$$

If

$$\frac{\partial^2 \boldsymbol{\Theta}}{\partial \theta^2} = -m^2 \boldsymbol{\Theta}, \tag{3.15}$$

admits the harmonic solution $\boldsymbol{\Theta}(\theta) = cos(m\theta + y_m)$, where y_m are obtained from initial conditions then, with m fixed in value, Eq. 3.14 becomes the *Bessel's equation*, which is,

$$\frac{\partial^2 \boldsymbol{R}}{\partial r^2} + \frac{1}{r}\frac{\partial \boldsymbol{R}}{\partial r} + \left(k^2 - \frac{m^2}{r^2}\right)\boldsymbol{R} = 0. \tag{3.16}$$

The solutions to this equation take the form of *Bessel's functions* of order m of the first kind $J_m(kr)$ and second kind $Y_m(kr)$ as shown in,

$$\boldsymbol{R}(r) = \boldsymbol{A}J_m(kr) + \boldsymbol{B}Y_m(kr). \tag{3.17}$$

The first few roots of the *Bessel's functions* and its derivative are available in this text [103] and are also shown in Appendix D.

The solution of Eq. 3.17 consists of oscillatory functions of kr whose amplitude reduces roughly as $1/\sqrt{kr}$. As $kr \to 0$, the function $\boldsymbol{B}Y_m(kr)$ becomes unbounded. However, the

membrane that extends across origin ($r = 0$) should have finite displacement. Thus, $\boldsymbol{B}$ in Eq. 3.17 should be zero, which reduces to,

$$\boldsymbol{R}(r) = \boldsymbol{A}J_m(kr). \tag{3.18}$$

At $r = a$, the boundary condition $\boldsymbol{R}(a) = 0$ requires $J_m(ka) = 0$. If the values of function of J_m in Eq. 3.18, that cause it to be zero are represented by j_{mn} and k_{mn} is defined as the function of j_{mn} and a as $k_{mn} = j_{mn}/a$, then the solution for a circular membrane with fixed rim is given by,

$$\boldsymbol{u}_{r,\theta,t} = \boldsymbol{A}_{mn}J_m(k_{mn}r)cos(m\theta + \gamma_{mn})e^{i\omega_{mn}t} \tag{3.19}$$

where, $\boldsymbol{A}_{mn} = A_{mn}e^{j\phi_{mn}}$. γ_{mn} is the azimuthal phase angle that depend on the location of initial excitation of the membrane and ϕ_{mn} is the initial phase angle of the motion.

Using zeros of the first kind $J_m(kr)$ of *Bessel function*, the speed of sound in a pipe and the pipe radius a, the fundamental frequency of the system can be obtained using,

$$f_{mn} = \frac{1}{2\pi}\frac{j_{mn}c}{a}. \tag{3.20}$$

The real part of Eq. 3.19 [103] gives the equation of the physical motion of (m, n) mode given by,

$$u_{r,\theta,t} = A_{mn}J_m(k_{mn}r)cos(m\theta + \gamma_{mn})cos(\omega_{mn}t + \phi_{mn}), \tag{3.21}$$

and their shapes are shown in Fig. 3.2 [104].

In Fig. 3.2, the first integer m represents the number of radial nodal lines, whereas the second integer n controls the number of nodal circles. The minimum value of n is 1, which corresponds to the first mode with the nodal circle at a fixed boundary.

The rigid boundary at $r = a$ also means that the normal component of the velocity vector is equal to zero which means,

$$J'_m(j'_{mn}) = \frac{\partial}{\partial r}[J_m(k_{mn}a)] = 0, \tag{3.22}$$

where, j'_{mn} are the extrema of *Bessel's functions*.

For a wave to be a plane wave, the acoustic variables should be of constant amplitude and phase on any plane perpendicular to the direction of propagation. The first mode represents the plane wave, and the frequency below which this mode occurs can be obtained by using

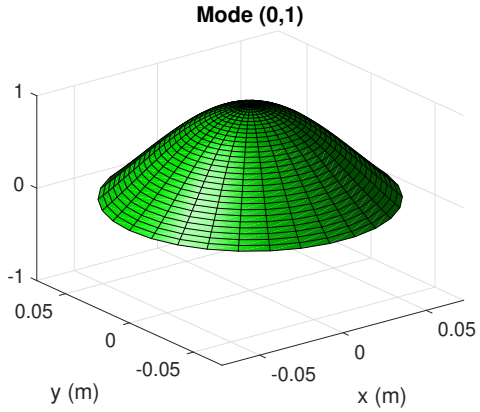

(a) Mode (0,1)

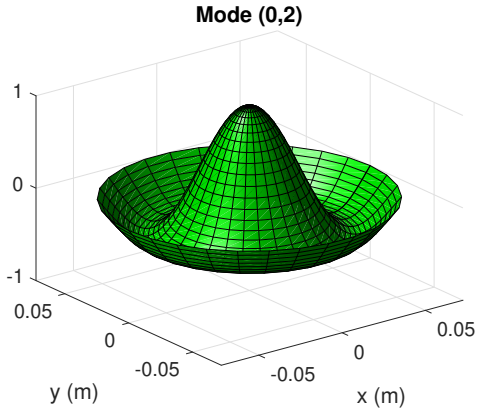

(b) Mode (0,2)

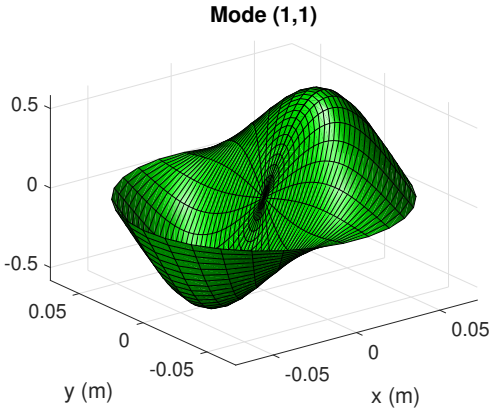

(c) Mode (1,1)

Figure 3.2: Modes of vibration of circular membrane fixed at the rim

j'_{mn}. The value of j'_{mn} for which the Eq. 3.22 is satisfied are substituted in Eq. 3.23 to obtain the cutoff frequency of that mode.

$$fc_{mn} = \frac{1}{2\pi}\frac{j'_{mn}c}{a}. \tag{3.23}$$

If the driving frequency (f) is greater than the cut-off frequency (fc_{mn}) of the wave and the axial wave number (k_s) is greater than zero, the acoustic wave with (m, n) mode shape propagates downstream along the pipe. At the cutoff frequency $f = fc_{mn}$ and zero axial wave number, there is no longitudinal acoustic wave motion. The axial wave number is

given by,

$$k_s = k_{mn}\sqrt{1 - \left(\frac{f c_{mn}}{f}\right)^2}. \tag{3.24}$$

If the driving frequency is lower than the cut-off frequency ($f c_{mn}$), the axial wave number is purely imaginary, and an acoustic wave with mode shape (m, n) does not propagate. The amplitude of this mode decays exponentially, and only the lower mode propagates downstream [105]. For instance, if the driving frequency of a wave is 1600 Hz and the cut-off frequency for mode (1,1) is 1863 Hz, mode (1,1) does not propagate and only lower mode, i.e., mode (0,1), propagates. The speed of sound, critical to the wave equation and subsequent theoretical background, is discussed next.

3.2.1 Wave speed

The speed at which a plane pressure wave travels in a given medium is known as the wave speed c. The acoustic field in a visco-elastic pipe is affected by material properties such as the bulk and shear modulus, as well as coupling between the pipe wall and the fluid [97]. The non-linearity of the pipe wall material and the dynamic effects of the pipe wall can significantly alter the speed of sound and will result in a frequency-dependent wave speed [96]. For thin-walled cylindrical structures, the inertial load is roughly equal to an additional mass per unit length. Therefore, at low frequencies, the elastic reaction greatly exceeds the inertial reaction, and hence the inertial effects can be neglected resulting in frequency independent wave speed [106].

This section briefly reviews the basic equations of motion and the equation for the speed of sound in the fluid-filled pipe. The pipe equation for $n = 0$ axisymmetric wave motion begins with the force equilibrium in axial and radial directions assuming there is no circumferential variation. These are given, with reference to Fig. 3.3, where the shell displacements are u, v and w in the axial (x), circumferential (θ), and radial (r) directions respectively, in equations 3.25 and 3.26 [107], respectively.

$$\rho\ddot{u} = \frac{\partial \sigma_x}{\partial x}, \tag{3.25}$$

$$(p_f(a) - p_m(a))(a/h) = \sigma_\theta + \rho a\ddot{w}, \tag{3.26}$$

where σ_x and σ_θ are the axial and circumferential stresses assessed at $r = a$, ρ is the density of the shell material, and a and h are the radial and thickness of the shell wall, respectively $(h << a)$. p_m and p_f are the pressures in the external and internal media, respectively.

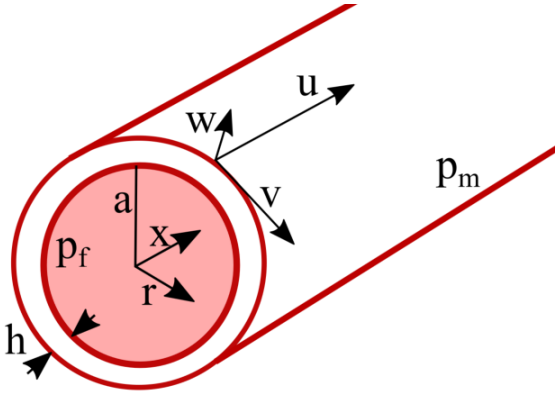

Figure 3.3: The co-ordinate system for a fluid filled pipe, surrounded by an infinite elastic medium.

These coupled with Hooke's Law relationships for the shell can be combined to yield the two coupled shell equations for $n = 0$ motion, given in equations 3.27 and 3.28,

$$\rho\ddot{u} - \frac{E}{1-\nu^2}\left(\frac{\partial^2 u}{\partial x^2} + \frac{\nu}{a}\frac{\partial w}{\partial x}\right) = 0, \tag{3.27}$$

$$\rho a\ddot{w} + \frac{E}{1-\nu^2}\left(\frac{w}{a} + \nu\frac{\partial u}{\partial x}\right) = [p_f(a) - p_m(a)]\frac{a}{h}, \tag{3.28}$$

in which E and ν are the shell material Young's modulus and the Poisson ratio, respectively, w/a and $\partial u/\partial x$ and the circumferential and axial strains, respectively.

The traveling wave solutions can be used to describe the displacements which are shown in equation 3.29 [107],

$$u = U_s e^{j(\omega t - k_s x)},\ w = W_s e^{j(\omega t - k_s x)}. \tag{3.29}$$

In the equation, ω is the angular frequency, and k_s is the axial wavenumber for the s wave. The traveling wave equations, coupled with the shell equations, are further expanded to derive the expression for the s wavenumbers [107].

If the internal medium is fluid (cannot endure shear), the internal pressure p_f can be described by the *Bessel function* J_0 of order zero and the external pressure p_m can be described by the *Hankel function* H_0 of order zero as,

$$p_f = P_{fs} J_0(k_{fs}^r r) e^{j(\omega t - k_s x)}, \tag{3.30}$$

$$p_m = P_{ds} H_0(k^r_{ds} r) e^{j(\omega t - k_s x)} + P_{rs} H_0(k^r_{rs} r) e^{j(\omega t - k_s x)}, \tag{3.31}$$

where, P_{fs}, P_{ds} and P_{rs} are the independent expressions for pressure coefficient and the formulation is given by Muggleton et al.(2002) [107]. The internal radial wavenumber, k^r_{fs} is related to fluid wave number, k_f by $(k^r_{fs})^2 = k_f^2 - k_s^2$. The radial components of longitudinal k^r_{ds} and shear wavenumbers k^r_{rs} are related to longitudinal k_d and shear k_r wavenumbers by,

$$(k^r_{ds})^2 = k_d^2 - k_s^2, \ (k^r_{rs})^2 = k_r^2 - k_s^2. \tag{3.32}$$

Substituting the pressure and displacement solutions into Eqs. 3.27 and 3.28 and solving for the fluid borne wavenumber (s = 1, $k_s = k_1$ from here onwards) for the low frequency gives Eq. 3.33,

$$k_1^2 = k_f^2 \left(1 + \frac{\frac{2B_f}{a}}{\frac{Eh}{a^2} - \omega^2(\rho h + M_{rad}) + i\rho R_{rad}}\right), \quad (h << a) \tag{3.33}$$

where, B_f is the bulk modulus of the contained fluid, and ρ is the density of the shell material [95].

The expression for the wavenumber given by Eq. 3.33 below the first cutoff frequency given by Eq. 3.23 corresponds to plane wave mode ($(m, n) = (0, 1)$) (shown in Fig. 3.2) and hence, k_1 can be reformulated in the form of impedances of the fluid, pipe wall, and the radiation to the surrounding medium. Muggleton et al. [107] expressed the wave number in the form of a ratio of the impedance of the fluid ($z_{fluid} = -2iB_f/(a\omega)$ to the pipe wall ($z_{pipe} = i(\rho h\omega - Eh/(a^2\omega))$ and the surrounding medium which is given by radiation impedance, (z_{rad}) [95], as shown in equation 3.34.

$$k_1^2 = k_f^2 \left(1 + \frac{z_{fluid}}{(z_{pipe} + z_{rad})}\right), \tag{3.34}$$

in which

$$z_{rad} = R_{rad} + i\omega M_{rad} = \sum_m \frac{-i\rho_m c_m k_m}{k^r_{m1}} \frac{H_0(k^r_{m1} a)}{H_0'(k^r_{m1} a)}, \tag{3.35}$$

where R_{rad} and M_{rad} are the resistance and mass components of the z_{rad} at the pipe wall; m is each wave type present in the surrounding medium, ρ_m, c_m and k_m are the density, wave speed, and wavenumber, respectively, for all wave types present. $(k^r_{m1})^2 = k_m^2 - k_1^2$ is the radial component of the wavenumber in the surrounding medium. The assumption is that the surrounding medium is infinite (and thus is no reflected waves are present). H_0 is the *Hankel function* of the second kind, representing incident waves (when the $e^{i\omega t}$ time dependence is adopted), and prime denotes differentiation [95].

For the in-vacuo case, there is no z_{rad} term and Eqs. 3.34 and 3.33 simplify to Eq. 3.36 [95].

$$k_1^2 = k_f^2(1 + \frac{z_{fluid}}{z_{pipe}}) = k_f^2(1 + \frac{2B_f/a}{(Eh/a^2 - \omega\rho h)}, \tag{3.36}$$

which at low frequencies simplifies to:

$$k_1^2 = k_f^2(1 + \frac{2B_f/a}{Eh/a^2}) \tag{3.37}$$

which is also known as the non-dispersive Korteweg equation [95] as the wave speed is independent of wave number and all waves of any wave number propagate at the same speed.

In the case where the pipe material is elastic and lossy, Young's modulus may be complex and comprise the term η which is the material loss factor ($E \rightarrow E(1 + i\eta)$. In a viscoelastic pipe, the wavenumber is then both complex and a function of the wave speed and attenuation. The analytical model for wave number for a fluid-filled pipe as shown in Eq. 3.38,

$$\boldsymbol{k}_1^2 = k_f^2\big(1 + \frac{B_f D}{E\, e + i\eta E\, h}\big) \tag{3.38}$$

In Eq. 3.38, D is the internal diameter of the pipe, and it is clear that pipe wall thickness also contributes to the speed of sound. A pipe is considered thin-walled if $\frac{D}{h} > 10$. One of the studies also shows the speed of sound as the function of the pipe support, called the pipe support factor ψ [108]. The value for ψ changes with the support condition and is a function of the pipe material's Poisson ratio ν, and whether it is thin-walled or thick-walled. For a thin-walled pipe free to expand throughout, $\psi = 1$. At low frequencies, for a circular elastic thin-walled pipe, solving the real part of Eq. 3.38 and substituting $k_f = \omega/c_f$, the speed of sound is reduced to Eq. 3.39 [95, 23]:

$$c = \frac{c_f}{\sqrt{1 + \frac{B_f D}{E\, h}}} \tag{3.39}$$

This value obtained from this equation provides a reference for experimentally obtained c from experiments later on. For example, for a PVC pipe of 14.5 cm diameter and a nominal thickness of 1 cm, assuming an elastic tensile modulus of 3.069 GPa and isothermal bulk modulus of fluid of 2.18 GPa, Eq. 3.39 results in a theoretical value for the speed of sound,

458 m/s. This value is used later in the thesis as a theoretical basis for the experimental study.

In practice, metal and plastic water pipes tend to exhibit broadly non-dispersive behavior over the frequency range in which measurements are made (which is usually below 500 Hz). Thus, the wave speed can be assumed to be approximately constant, so the phase and the real part of the wavenumber tend to have approximately straight-line behavior as a function of frequency. The imaginary part of Eq. 3.38 results in the attenuation as shown in Eq. 3.41.

$$\text{Wave attenuation } (dB/m) = \text{Attenuation / wavelength} \quad \text{x} \quad \text{wavelengths / metre} \tag{3.40}$$

$$\text{Wave attenuation } (dB/m) = -\frac{20\pi\eta}{ln(10)} \quad \text{x} \quad \frac{Re(\boldsymbol{k}_{mn})}{2\pi} \tag{3.41}$$

This attenuation of the wave is due to losses within the pipe wall as the wall expands and contracts in response to the wave pressure, with a higher loss factor resulting in higher attenuation. Experimental studies of loss factor in a 34 m long water-filled MDPE (medium density polyethylene) pipe of 180 mm diameter system by Muggleton et al. [95, 109] showed the value about $\eta = 0.06$. The experiment used a modified underwater loudspeaker to excite a stepped sine wave in the frequency range of 30 Hz to 1kHz with 1Hz increments, and the pressure was measured using two hydrophones placed 2 m apart. The loss factor corresponding to the plane wave is practically zero because the particles of the plane wave oscillate in the direction of wave propagation.

For the PVC pipe of diameter 14.5 cm and nominal thickness of 1 cm (which have been used in experimental studies later), the frequency-dependent attenuation when η is 0 and 0.06 is shown in Fig. 3.5. The attenuation is obtained by the multiplication of attenuation per wavelength and wavelength per meter, and each quantity in terms of frequency in the range of 1 to 100 Hz is shown in Fig. 3.4.

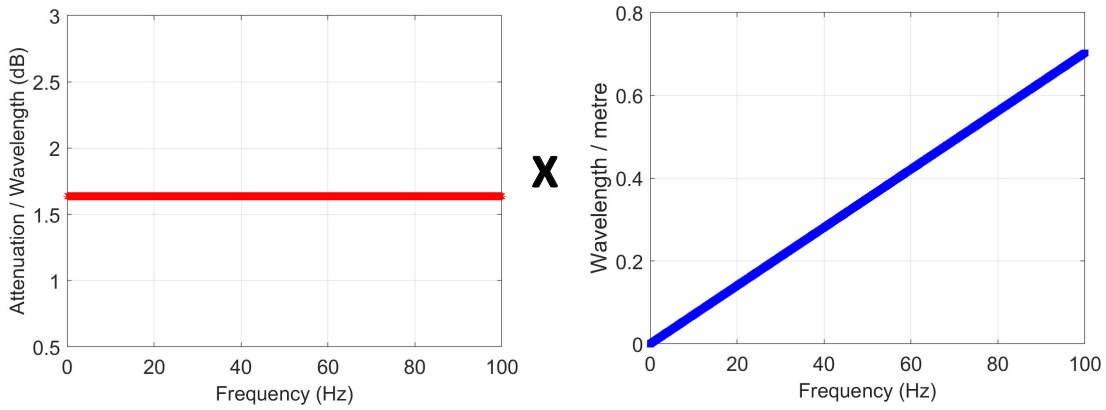

Figure 3.4: Attenuation per wavelength and wavelength per metre for $\eta = 0.06$. The linearity between wavelength/metre and frequency is because of constant c

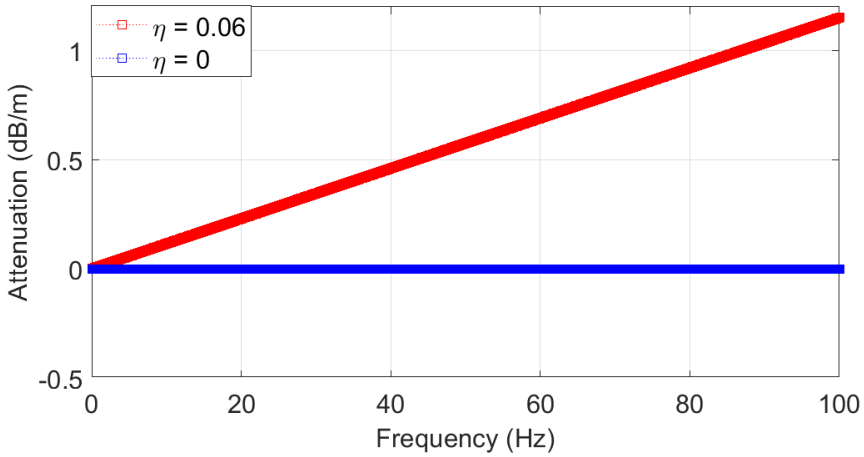

Figure 3.5: Comparison of signal attenuation for different value of η

3.2.2 Wave number and its relationship to group speed and propagation angle

Group velocity of the wave is the velocity of the propagation of the envelope modulated by waves of different frequencies [110]. The theoretical speed can be used to understand the group velocity and the propagation angle of the wave in the frequency range (1-12kHz) of relevance to the experiments presented in this study (in a 14.5 cm diameter PVC pipe).

The axial and radial numbers, $k_s = \sqrt{(\omega/c)^2 - k_{mn}^2}$ and $k_{mn} = \frac{j'_{mn}}{a}$ respectively are needed to calculate the group velocity [85] which is expressed in ([103]),

$$V_{gn} = \frac{ck_s}{\sqrt{k_s^2 + k_{mn}^2}} = \frac{c\sqrt{(\omega/c)^2 - k_{mn}^2}}{(\omega/c)}. \tag{3.42}$$

$$\theta_{kn} = cos^{-1}(\frac{k_s}{k}) \quad \text{and } k = k_{mn} + k_s \tag{3.43}$$

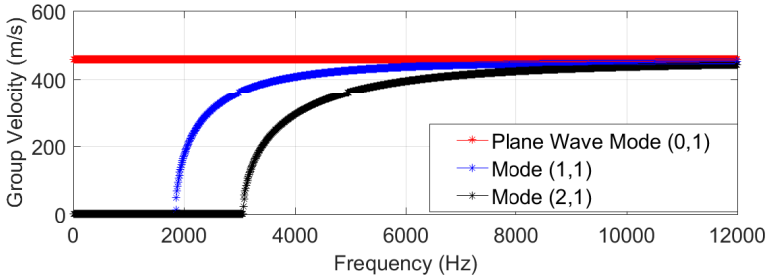

(a)

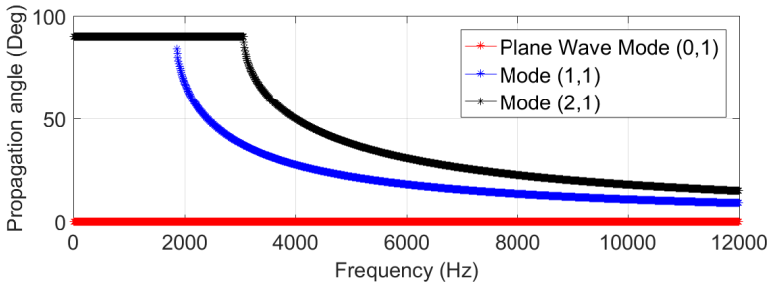

(b)

Figure 3.6: Plane wave: (a) group velocity; (b) propagation angle

Figure 3.6a shows the group velocity for three modes, showing that the velocities associated with higher modes (mode (1,1) or mode (2,1)) are lower than the plane wave mode (mode (0,1)) velocity [85]. The propagation angle in that frequency range calculated using Eq. 3.43 and Fig. 3.6b shows that the higher modes travel along a diagonal direction in a 'zigzag' manner at an angle (θ_{kn}) with respect to the centre line of the pipe ($k_{mn} \neq 0$ in Eq. 3.43), while plane waves travel in straight path along the pipe ($k_{mn} = 0$ in Eq. 3.43). Theoretically, below the cut-off of 1863 Hz (for the experimental pipe properties

used here), the plane wave mode dominates, and above this cut-off frequency, there is more than one wave propagating in the pipe. All the experiments presented in this dissertation are conducted below this cut-off frequency.

With the derivation of equation of motion of two-dimensional wave, the acoustic wave equation is derived next, which shows the relationship between acoustic pressure fluctuation or particle velocity as a function of position (x) and time (t) in a fluid.

3.3 Acoustic Wave Equation

The wave equation of motion in Section 3.2 presents the equation of motion, especially the the modes of vibration and the associated frequencies. The active approach used in this thesis utilizes an acoustic source to excite the fluid, thereby generating acoustic pressure waves within the water column. These waves are then used to probe for leaks in the system. The terms impedance and reflection coefficient used in this dissertation are described in terms of acoustic pressure in this section. The wave equation of motion which governs the propagation of acoustic waves through a material medium is derived next. For this, the acoustic pressure p in terms of adiabatic bulk modulus K and condensation s is expressed as ([103]),

$$p \approx Ks. \tag{3.44}$$

Condensation, s is the change in density with respect to an ambient density, $s = (\rho - \rho_0)/\rho_0$ where ρ and ρ_0 are the instantaneous and equilibrium density at (x,y,z). Condensation occurs due to compression and relaxation of a particle in a fluid as sound propagates. To relate the motion of the fluid with its compression or expansion, a relationship between particle velocity and local density is required. The net influx of mass in a fixed control volume due to flow in the x-direction as shown in Fig. 3.7 is given by,

$$[\rho u_x - (\rho u_x + \frac{\partial(\rho u_x)}{\partial x})dx]dydz = -\frac{\partial(\rho u_x)}{\partial x}dV. \tag{3.45}$$

Similarly, the net influx of mass is obtained in the y- and z-directions and summed to give total influx as,

$$-(\frac{\partial(\rho u_x)}{\partial x} + \frac{\partial(\rho u_y)}{\partial y} + \frac{\partial(\rho u_z)}{\partial z})dV = -\nabla.(\rho\vec{u})dV. \tag{3.46}$$

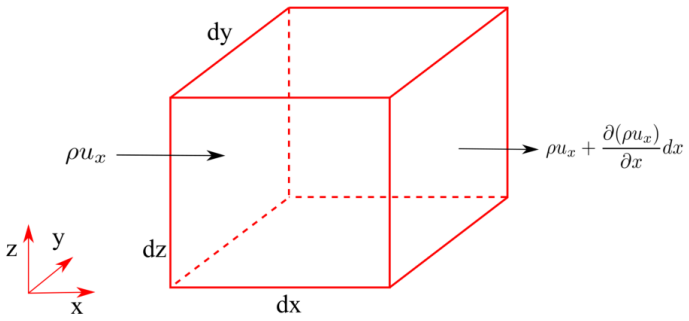

Figure 3.7: Fixed volume showing the rate of mass flow into and out of the volume in x-direction.

Where, $\vec{u}$ is the particle velocity of the fluid element, ∇ is the vector differential operator and $dV = dx\,dy\,dz$ is the volume element.

The rate of mass increase in the volume is $(\partial\rho/\partial t)dV$, which is equal to the total influx. This gives,

$$\frac{\partial \rho}{\partial t} + \nabla.(\rho\vec{u}) = 0. \tag{3.47}$$

Writing ρ as $\rho = \rho_0(1 + s)$, where ρ_0 is a weak function of time and s is very small, the previous equation becomes,

$$\rho_0 \frac{\partial s}{\partial t} + \nabla.(\rho_0\vec{u}) = 0. \tag{3.48}$$

Eq. 3.48 is used with the Euler's equation for the derivation of wave equation. For acoustic processes of small amplitude, the *linear Euler's equation* [103] is,

$$\rho_0 \frac{\partial \vec{u}}{\partial t} = -\nabla p. \tag{3.49}$$

The derivation of this equation can be found in several books (e.g., [111]). The divergence of the linear Euler's equation in Eq. 3.49 results in,

$$\nabla.(\rho_0 \frac{\partial \vec{u}}{\partial t}) = -\nabla^2 p. \tag{3.50}$$

The time derivative of Eq. 3.48 results in,

$$\rho_0 \frac{\partial^2 s}{\partial t^2} + \nabla.(\rho_0 \frac{\partial \vec{u}}{\partial t}) = 0. \tag{3.51}$$

Dropping the divergence term from both Eq. 3.50 and Eq. 3.51 and expressing condensation in the form $s = p/B_f$ results in the linear, lossless wave equation for propagation of sound in fluids with speed c. This is expressed as

$$\nabla^2 p = \rho_0 \frac{\partial^2 s}{\partial t^2} = \frac{1}{c^2}\frac{\partial^2 p}{\partial t^2}. \tag{3.52}$$

With the derivation of acoustic wave equation, the solution to this partial differential equation is discussed next.

3.3.1 General plane waves

For a wave to be a plane wave, the acoustic variables have to be constant in amplitude and phase on any plane perpendicular to the direction of propagation [103]. If a plane wave is propagating along the x-axis, Eq. 3.52 becomes,

$$\frac{\partial^2 p}{\partial x^2} = \frac{1}{c^2}\frac{\partial^2 p}{\partial t^2}. \tag{3.53}$$

Equation 3.53 is a second-order partial differential equation whose solution contains two functions. The complex solution for the acoustic pressure and particle velocity of a plane wave traveling along x-axis [103] is given by:

$$\boldsymbol{p} = \boldsymbol{P}_i e^{j(\omega t - kx)} + \boldsymbol{P}_r e^{j(\omega t + kx)} \tag{3.54}$$

$$\vec{\boldsymbol{u}} = \boldsymbol{u}\hat{x} = [\frac{\boldsymbol{P}_i}{\rho_0 c} e^{j(\omega t - kx)} - \frac{\boldsymbol{P}_r}{\rho_0 c} e^{j(\omega t + kx)}]\hat{x} \tag{3.55}$$

where, $\boldsymbol{P}_i$ and $\boldsymbol{P}_r$ are the complex pressure amplitudes of incident and reflected waves, respectively and are determined by boundary conditions.

For a plane wave travelling not limited to one-dimension, the equation reduces to,

$$\boldsymbol{p} = \boldsymbol{P}_i e^{j(\omega t - k_x x - k_y y - k_z z)} \tag{3.56}$$

$$\boldsymbol{p} = \boldsymbol{P}_i e^{j(\omega t - \vec{k}.\vec{r})} \tag{3.57}$$

where, $\vec{k}$ is the propagation vector defined as $\vec{k} = k_x\hat{x} + k_y\hat{y} + k_z\hat{z}$ and $\vec{r}$ is the position vector which is $\vec{r} = x\hat{x} + y\hat{y} + z\hat{z}$. $\hat{x}$, $\hat{y}$, $\hat{z}$ are the unit vectors in the x, y and z directions, respectively.

3.3.2 Reflection and transmission of plane waves

If a plane wave traveling in a medium encounters a boundary or discontinuity, portions of this wave are reflected and transmitted. The ratios of the pressure amplitudes of reflected and transmitted waves to the incident wave depend on the impedance of the medium and the speed of sound [103]. The incident wave traveling in the positive x-direction is $\boldsymbol{p}_i$, the reflected wave $\boldsymbol{p}_r$ and a transmitted wave $\boldsymbol{p}_t$ as shown in Fig. 3.8 can be represented by:

$$\begin{aligned} \boldsymbol{p}_i &= \boldsymbol{P}_i e^{j(\omega t - k_1 x)} \\ \boldsymbol{p}_r &= \boldsymbol{P}_r e^{j(\omega t + k_1 x)} \\ \boldsymbol{p}_t &= \boldsymbol{P}_t e^{j(\omega t - k_2 x)} \end{aligned} \tag{3.58}$$

where $\boldsymbol{P}_t$ is the complex pressure amplitudes of transmitted waves. It can be noticed that the wavenumbers are different before and after encountering a discontinuity.

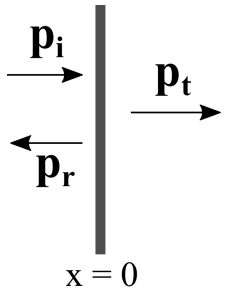

Figure 3.8: Reflection and transmission of wave incident on a boundary

A wave passing through a discontinuity should follow the continuity of pressure, $\boldsymbol{p}$, and volume velocity, $\boldsymbol{U}$. If such a discontinuity is at $x = 0$ and the boundary conditions are followed, then

$$\boldsymbol{p}_i + \boldsymbol{p}_r = \boldsymbol{p}_t. \tag{3.59}$$

$$\boldsymbol{U}_i + \boldsymbol{U}_r = \boldsymbol{U}_t. \tag{3.60}$$

Division of Eq. 3.59 by Eq. 3.60 yields

$$\frac{\boldsymbol{p}_i + \boldsymbol{p}_r}{\boldsymbol{U}_i + \boldsymbol{U}_r} = \frac{\boldsymbol{p}_t}{\boldsymbol{U}_t}, \quad \text{at x} = 0. \tag{3.61}$$

By introducing acoustic impedance $\boldsymbol{Z}$ which is $\boldsymbol{Z} = \boldsymbol{p}/\boldsymbol{U} = \rho_0 c/S$, for section before the discontinuity, i.e., $x < 0$ as:

$$\boldsymbol{Z} = R + jX = \frac{\boldsymbol{p}_i + \boldsymbol{p}_r}{\boldsymbol{U}_i + \boldsymbol{U}_r} = \frac{\rho_0 c}{S} \frac{\boldsymbol{P}_i e^{-jkx} + \boldsymbol{P}_r e^{jkx}}{\boldsymbol{P}_i e^{-jkx} - \boldsymbol{P}_r e^{jkx}} \tag{3.62}$$

where, R and X are mechanical resistance and reactance and S is cross section area before the discontinuity. At the discontinuity, i.e., $x = 0$

$$\boldsymbol{Z}_0 = \frac{\rho_0 c}{S} \frac{\boldsymbol{P}_i + \boldsymbol{P}_r}{\boldsymbol{P}_i - \boldsymbol{P}_r}. \tag{3.63}$$

Solving the above equation for the pressure reflection coefficient, $\frac{\boldsymbol{P}_r}{\boldsymbol{P}_i}$, gives:

$$\frac{\boldsymbol{P}_r}{\boldsymbol{P}_i} = \frac{\boldsymbol{Z}_0 - \rho_0 c/S}{\boldsymbol{Z}_0 + \rho_0 c/S}. \tag{3.64}$$

The power transmission and reflection coefficients based on the pressure reflection coefficients and impedance $\boldsymbol{Z}_0$ are shown in Eq. 3.65. This equation is used later to obtain the reflection and transmission coefficients based on impedance of side branch.

$$\begin{aligned} R_\Pi &= |\frac{\boldsymbol{P_r}}{\boldsymbol{P_i}}|^2 \\ T_\Pi &= 1 - R_\Pi \end{aligned} \tag{3.65}$$

3.4 Plane Wave and Acoustic Impedance in Pipes

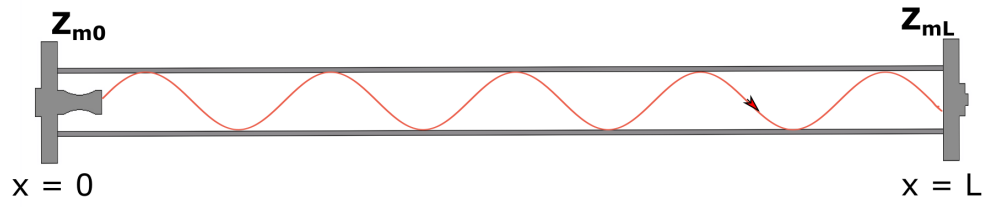

Figure 3.9: Schematic of single pipe system with no leak and driven by an acoustic source at $x = 0$

For a fluid-filled pipe of cross-sectional area S and length L, driven at $x = 0$, and closed at $x = L$ (Fig. 3.9), the plane wave propagating along the x-axis is given by,

$$\boldsymbol{p} = \boldsymbol{P}_i e^{j(\omega t - k(L-x))} + \boldsymbol{P}_r e^{j(\omega t + k(L-x))}. \tag{3.66}$$

The continuities of particle speed and force require that the mechanical impedance of wave at $x = L$ should be the same as the mechanical impedance, $\boldsymbol{Z}_{mL}$, of the closed-end. The force of the fluid on termination is $\boldsymbol{p}(L,t)S$ and the particle speed [103] is given by,

$$\boldsymbol{u}(L,t) = -\frac{1}{\rho_0}\int \frac{\partial \boldsymbol{p}}{\partial x}dt. \tag{3.67}$$

From this, the impedance at the termination is given by,

$$\boldsymbol{Z}_{mL} = \frac{\boldsymbol{p}(L,t)S}{\boldsymbol{u}(L,t)}. \tag{3.68}$$

Using Eq. 3.66 and Eq. 3.67, Eq. 3.68 can be written as,

$$\boldsymbol{Z_{mL}} = \rho_0 c S\,\frac{\boldsymbol{P}_r + \boldsymbol{P}_i}{\boldsymbol{P}_r - \boldsymbol{P}_i}. \tag{3.69}$$

Similarly, impedance at the driven end reduces to,

$$\boldsymbol{Z_{m0}} = \rho_0 c S\,\frac{\boldsymbol{P}_r e^{jkL} + \boldsymbol{P}_i e^{-jkL}}{\boldsymbol{P}_r e^{jkL} - \boldsymbol{P}_i e^{-jkL}}. \tag{3.70}$$

In reality, the sound is absorbed within a fluid and by the walls of the pipe. In this case, the wavenumber k in the lossless solution should be replaced with a complex wavenumber, $\boldsymbol{k} = k - j\alpha$. The absorption coefficient, α, is given by Sharp [84] as,

$$\alpha = \frac{1}{R_0 c}\left(\sqrt{\frac{\eta\omega}{2\rho_0}} + (\gamma - 1\sqrt{\frac{\kappa\omega}{2\rho_0 c_p}})\right). \tag{3.71}$$

where, η, γ, κ, and c_p are the coefficient of shear viscosity of water, the ratio of the principal specific heats of water, the thermal conductivity of water, and the specific heat of water at constant pressure, respectively.

3.4.1 Impedance of a closed-end pipe

Referring to the pipe in Fig. 3.9 driven at $x = 0$ whose impedances are given by $\boldsymbol{Z}_{mL}$ and $\boldsymbol{Z}_{m0}$ at the terminated and driven ends respectively, the incident wave is partially reflected due to $\boldsymbol{Z}_{mL}$. The impedance $\boldsymbol{Z}_{mL}$ in terms of $\boldsymbol{Z}_{m0}$ is computed by solving Eq. 3.69 and Eq. 3.70, followed by eliminating $\boldsymbol{P}_i$ and $\boldsymbol{P}_r$ [103]. The impedance $\boldsymbol{Z}_{m0}$ as a function of $\boldsymbol{Z}_{mL}$ as shown in Fig. 3.9 can be obtained using,

$$\frac{\boldsymbol{Z}_{m0}}{\rho_0 cS} = \frac{\frac{\boldsymbol{Z}_{mL}}{\rho_0 cS} + jtan\boldsymbol{k}L}{1 + j(\frac{\boldsymbol{Z}_{mL}}{\rho_0 cS})tan\boldsymbol{k}L}. \tag{3.72}$$

If the end at $x = L$ is closed by a rigid cap, the resonance condition is obtained, which is $|\frac{\boldsymbol{Z}_{mL}}{\rho_0 cS}| \rightarrow \infty$. This means the incident acoustic wave is reflected back, increasing the amplitude of the resulting wave. Eq. 3.72 then becomes

$$\frac{\boldsymbol{Z_{m0}}}{\rho_0 cS} = -j\ cot\boldsymbol{k}L. \tag{3.73}$$

In the above equation, the complex wave number $\boldsymbol{k}$ can again be substituted in the form of the real wave number and absorption coefficient; with the expansions of sines and cosines of the complex argument, Eq. 3.73 becomes Eq. 3.74. For the closed end, leak free pipe, the impedance of the system at the source, i.e., at $x = 0$ is given by,

$$\frac{\boldsymbol{Z}_{m0}(f)}{\rho_0 cS} = \frac{\alpha L - j\, cosk L\, sinkL}{sin^2 kL + (\alpha L)^2 cos^2 kL}. \tag{3.74}$$

3.4.2 Impedance of a driver-pipe system

When the acoustic wave is generated through an acoustic driver, the driver's properties are tightly coupled with the resonating properties of the fluid-pipe system. The driver has its own mechanical impedance; hence the mechanical resonance of the combined system combines the mechanical behavior of both the pipe and the driver. If a driver, as shown

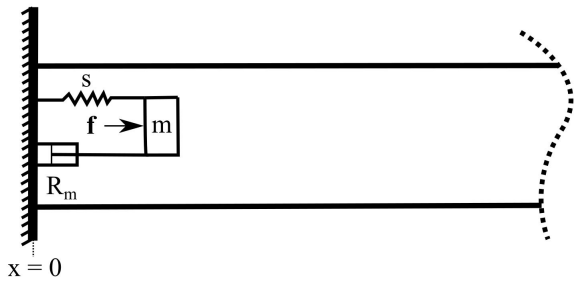

Figure 3.10: Schematic of a coupled driver-pipe system

in Fig. 3.10, is modeled as a damped harmonic oscillator generating a force $\boldsymbol{f}$, the motion of the mass is given by ([103]):

$$m\frac{\partial^2 \boldsymbol{\xi}}{\partial t^2} = -R_m\frac{\partial \boldsymbol{\xi}}{\partial t} - s\boldsymbol{\xi} - S\boldsymbol{p}(0,t) + \boldsymbol{f} \tag{3.75}$$

where, $\boldsymbol{\xi}$ is displacement of mass to the right, $\boldsymbol{p}(0,t)$ is pressure in the pipe at $x = 0$, and $\boldsymbol{f} = F\ exp(j\omega t)$. R_m and s are the mechanical resistance and stiffness of the driver respectively and the complex speed of the mass is $\boldsymbol{u}(0,t) = d\boldsymbol{\xi}/dt$. Eq. 3.75 then becomes,

$$\boldsymbol{f} = [R_m + j(\omega m - \frac{s}{\omega}) + \frac{S\boldsymbol{p}(0,t)}{\boldsymbol{u}(0,t)}]\boldsymbol{u}(0,t). \tag{3.76}$$

The first two terms in Eq. 3.76 are related to the mechanical impedance of the driver $\boldsymbol{Z}_{md}$ while the remaining term is the mechanical impedance of the pipe $\boldsymbol{Z}_{m0}$. Therefore, Eq. 3.76 can be written in the form of total impedance, $\boldsymbol{Z_T}$ as,

$$\boldsymbol{f} = \boldsymbol{Z_T}\boldsymbol{u}(0,t) = (\boldsymbol{Z}_{md} + \boldsymbol{Z}_{m0})\boldsymbol{u}(0,t). \tag{3.77}$$

The change in pipe geometry, such as a leak, joint, or a change in the diameter, affects the impedance of the pipe, which changes the total impedance of the system. The coupling behavior between the driver and pipe is helpful to study the dynamics of the forced system and can also be used as a detection tool when impedance changes are suddenly introduced (say, leaks) on the pipe boundary.

Eq. 3.77 shows that both the driver and pipe mechanical behaviors are combined to make up the mechanical resonance of the combined system. For the system to resonate, the imaginary part of total impedance has to be zero, i.e., $\mathrm{Im}(\boldsymbol{Z}_T) = 0$. For the leak-free system, substituting the value of $\boldsymbol{Z}_{md}$ and $\boldsymbol{Z}_{m0}$ in Eq. 3.77 and solving for the resonant condition in terms of kL yields,

$$\frac{cos\ kL\ sin\ kL}{sin^2 kL + (\alpha L)^2 cos^2 kL} = a_m kL - \frac{b_s}{kL}, \tag{3.78}$$

where, $a_m = \frac{m}{S\rho_0 L}$ is the ratio of the mass of the acoustic driver to the mass of the fluid in the pipe and $b_s = \frac{sL}{S\rho_0 c^2}$ is the ratio of stiffness of the driver to the fluid inside the pipe. The resonance frequencies of the combined system are obtained by solving Eq. 3.78.

3.4.3 Impedance of a pipe with a leak

A leak in the pipe can be modeled using a *branch* discontinuity as explained in this section. Assume that a branch with arbitrary input impedance is located at $x = 0$ as shown in Fig. 3.11.

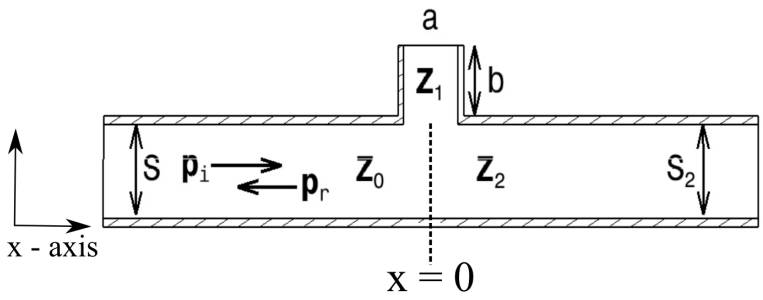

Figure 3.11: Schematic of a pipe with two branches showing the incident and reflected waves.

The incident and reflected waves shown in Eq. 3.58 are then expressed as,

$$\begin{aligned} \boldsymbol{p}_i &= \boldsymbol{P}_i e^{j\omega t}, \\ \boldsymbol{p}_r &= \boldsymbol{P}_r e^{j\omega t}. \end{aligned} \tag{3.79}$$

In terms of input impedances and complex volume velocity, they can be written as

$$\begin{aligned} \boldsymbol{p}_1 &= \boldsymbol{Z}_1 \boldsymbol{U}_1 e^{j\omega t}, \\ \boldsymbol{p}_2 &= \boldsymbol{Z}_2 \boldsymbol{U}_2 e^{j\omega t}. \end{aligned} \tag{3.80}$$

Similarly, as before, continuity of pressure and volume velocity at the junction requires

$$\boldsymbol{p}_i + \boldsymbol{p}_r = \boldsymbol{p}_1 + \boldsymbol{p}_2, \tag{3.81}$$

and

$$\boldsymbol{U}_i + \boldsymbol{U}_r = \boldsymbol{U}_1 + \boldsymbol{U}_2. \tag{3.82}$$

Division of Eq. 3.82 by Eq. 3.81 and solving for impedance results in the admittance of the pipe branches. Admittance is a measure of how easily a system allows an acoustic wave to flow across and is a reciprocal of impedance. This shows that the combined acoustic

admittance associated with the incident and reflected waves equal to the sum of acoustic admittance of the two branches,

$$\frac{1}{\boldsymbol{Z}_0} = \frac{1}{\boldsymbol{Z}_1} + \frac{1}{\boldsymbol{Z}_2}. \tag{3.83}$$

Now, consider a leak of radius a in a pipe as shown in Fig. 3.11. This pipe is also driven at $x = 0$ and terminated by a rigid cap at $x = L$. Modeling the leak orifice as a branch, the impedance of the branch Z_1 can be expressed as ([103]):

$$\boldsymbol{Z}_1 = R_1 + j\ X_1 = \frac{\rho_0 c k^2}{4\pi} + j\omega \frac{\rho_0 L'}{\pi a^2}, \tag{3.84}$$

where, the first term R_1 is the radiation resistance of the pipe, the second term X_1 is the reactance due to the pressure difference of the fluid going through the side branch. The reactance can also be written in the form of pressure difference as $X_1 = \omega\,(\Delta p_f/\dot{Q})$. The term inside the bracket is called *inertance (I)* of the fluid, where Δp_f is the pressure difference of the fluid, and Q is the volumetric flow rate. L' is the effective length, and b is the length of the branch. For flanged and un-flanged branches, the effective lengths are [103],

$$\begin{aligned} L' &= L + (0.85 + 0.85)a = b + 1.7a, && \text{flanged} \\ L' &= L + (0.85 + 0.6)a = b + 1.4a. && \text{un-flanged} \quad . \end{aligned} \tag{3.85}$$

The impedance of a branch can be easily obtained by substituting the value of k and other parameters such as c, L' and a into Eq. 3.84.

3.4.4 Acoustic filter: high pass

Presence of a leak discussed in Section 3.4.3 behaves as a high pass filter. Attenuation of the energy of transmitted sound due to the side branch in the pipe is the basis of an *acoustic filter*. If a pipe has a short length of unflanged pipe as a branch, the radius a and length L of this branch are both small compared to the wavelength, then the pipe system is considered to act as an acoustic high pass filter, and the impedance is given by Eq. 3.84. The ratio of acoustic resistance to the reactance of this branch is given by,

$$\frac{R_1}{X_1} = \frac{ka^2}{4L'}. \tag{3.86}$$

Using Eqs. 3.64, 3.65 and replacing $\boldsymbol{Z}_0$ with the branch impedance $\boldsymbol{Z}_1$, the power transmission T_Π and the reflection coefficient R_Π in terms of R_1 and X_1 are given by,

$$\begin{aligned} T_\Pi &= \frac{R_1^2 + X_1^2}{(\frac{\rho_0 c}{2S} + R_1)^2 + X_1^2} \\ R_\Pi &= \frac{(\frac{\rho_0 c}{2S})^2}{(\frac{\rho_0 c}{2S} + R_1)^2 + X_1^2}. \end{aligned} \tag{3.87}$$

If the radius of the branch is small compared to the wavelength, R_1 is very small compared to X_1 in calculating the transmission coefficients, and hence can be neglected. Thus, using Eq. 3.84 and Eq. 3.87 and neglecting the resistance term, T_Π and R_Π can be computed using,

$$\begin{aligned} T_\Pi &= \frac{1}{1 + (\frac{\pi a^2}{2SL'k})^2} \\ R_\Pi &= 1 - T_\Pi. \end{aligned} \tag{3.88}$$

Therefore, with known section impedance $\boldsymbol{Z}_2$ and branch impedance $\boldsymbol{Z}_1$, the impedance $\boldsymbol{Z}_1$ can be determined using an equation similar to Eq. 3.83. With impedance, $\boldsymbol{Z}_1$ known, the impedance at the source $\boldsymbol{Z_{m0}}$ can be calculated using equation similar to Eq. 3.72. The impedance $\boldsymbol{Z}_{m0}$ combined with the driver impedance can be used to understand the resonance condition of the pipe system (formulation already shown in Eq. 3.78).

Experimentally, the impedance of the source is,

$$\boldsymbol{Z}_{m0} = \frac{S\boldsymbol{p}(0,t)}{\boldsymbol{u}(0,t)}, \tag{3.89}$$

if particle velocity is known, where $\boldsymbol{p}(0,t)$ is the pressure at $x = 0$. Experimentally, particle velocity is not easy measure. Therefore, techniques such as the two-sensor or the multi-sensor technique can be applied [112] to separate the waves into their constituent components. The separated incident and reflected parts of the wave can then be used to estimate the impedance of the system experimentally. This is further discussed in Section 4.1.3.

3.5 Basics of Signal Processing

This thesis relies heavily on processing digitally acquired acoustic signals, hence key ideas and algorithms in signal processing are presented here for the sake of completeness. Signal processing broadly refers to the science of analyzing time-variant physical processes [113]. Sophisticated tool boxes and commercial software that are available today enable digital signal processing techniques for complex applications reliably. The discrete-time signal analysis covered within this dissertation uses signals whose independent time variable is quantized. Thus, the discrete-time signal is represented by the sequence of values obtained by sampling a continuous signal at uniformly spaced time intervals as shown in Fig. 3.12. The signal in the figure is a 2 Hz sine wave with a sampling frequency f_s (the number of samples taken from a continuous signal per one-second interval) of 80 Hz. It also means the data is sampled once every 0.0125 seconds ($\Delta t = 1/f_s$). Dealing with such digital signals requires special tools and techniques, as described in this section.

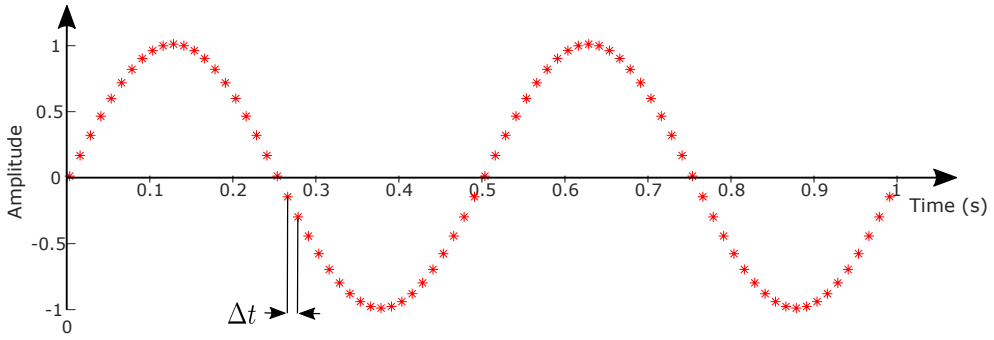

Figure 3.12: Discretization of a continuous signal sampled at uniformly spaced time intervals.

3.5.1 Fourier transform (FT)

Fourier analysis of signals is the most commonly used signal processing technique where the functions may be approximated by the sums of simpler trigonometric functions. The Fourier transform is a special transform which decompose the time dependent functions into functions depending on frequency. There is also a inverse Fourier transform that carrying out Fourier domain results to original domain. The analysis performed in Fourier domain is called the frequency domain analysis [113, 114].

Consider a periodic signal $f(t)$ which can be expressed as,

$$f(t) = a_o + \sum_{n=0}^{\infty} \left(a_n \cos n\omega_0 t + b_n \sin n\omega_0 t\right), \quad t_1 \leq t \leq t_1 + T_o, \tag{3.90}$$

where $\omega_0 = \frac{2\pi}{T_0}$ and T_o is the period of the signal $f(t)$,

$$\begin{aligned} a_o &= \frac{1}{T_o}\int_{t_1}^{t_1+T_o} f(t)dt \\ a_n &= \frac{2}{T_o}\int_{t_1}^{t_1+T_o} f(t)\cos n\omega_0 t dt, \quad n = 1, 2, \cdots \\ b_n &= \frac{2}{T_o}\int_{t_1}^{t_1+T_o} f(t)\sin n\omega_0 t dt, \quad n = 1, 2, \cdots \end{aligned}$$

in which the bias is represented by a_0 term.

Usually, the complex exponential functions are used to represent the sinusoids. Equation 3.90 shown in the form of complex exponential functions is,

$$f(t) = \sum_{n=-\infty}^{\infty} D_n e^{jn\omega_o t} \tag{3.91}$$

where,

$$D_n = \frac{1}{T_o}\int_{-T_o/2}^{T_o/2} f(t)e^{-jn\omega_o t}dt. \tag{3.92}$$

The equation above are the representative of periodic signal. For the non-periodic signal, the limits of the integral in Eq. 3.92 changes to $\pm\infty$ and the transform becomes,

$$F(n\omega_o) = \int_{n=-\infty}^{\infty} f(t)e^{-jn\omega_o t}dt, \tag{3.93}$$

and,

$$D_n = \frac{1}{T_o}F(n\omega_o). \tag{3.94}$$

The inverse Fourier transform is,

$$f(t) = \frac{1}{2\pi}\int_{-\infty}^{\infty} F(\omega)e^{-jn\omega t}d\omega$$

Discrete Fourier transform (DFT)

The discrete Fourier Transform (DFT) enables Fourier transformations for discretely sampled signals, as the process of converting from the continuous to the discrete domain introduces several challenges. Mathematically, DFT is computed from a finite number of samples treating the data as if it were periodic. The discrete Fourier transform is different from continuous in the sense that the continuous Fourier transform is an exact representation of the function, while in the case of discrete Fourier transform, only the periodic version of the function is captured.

The equation for a finite DFT is defined as [113],

$$F(n\Delta\omega) = \sum_{k=0}^{N-1} f(k\Delta t) e^{-j2\pi k\, n/N} \Delta t, \tag{3.95}$$

where, $\Delta\omega = \frac{2\pi}{T_0}$, $T_0 = N\Delta t$ and $f(t)$ is a function that has a sequence of N complex numbers.

The inverse pair of the Eq. 3.95 is given by,

$$f(n\Delta t) = \frac{1}{2\pi} \sum_{n=0}^{N-1} F(n\Delta\omega) e^{-j2\pi k\, n/N} \Delta\omega. \tag{3.96}$$

The evaluation of Eq. 3.96 gives the property $f((N+k)\Delta t) = f(k\Delta t)$. Equation 3.95 can be written in the form of real and imaginary term as shown in,

$$F(n\Delta\omega) = \sum_{k=0}^{N-1} f(k\Delta t) \cos(2\pi k\, n/N)\Delta t - j \sum_{k=0}^{N-1} f(k\Delta t) \sin(2\pi k\ n/N)\Delta t. \tag{3.97}$$

Nyquist frequency

The rate at which the function is sampled is given by $\Delta f = \frac{1}{T_0}$, where T_0 is the sampling time period in seconds. The highest frequency of interest for analysis—called the *Nyquist* frequency—is determined by the sampling rate, which is at least twice the Nyquist frequency (according to the Nyquist theorem) [114]. Typically to improve the resolution and preventing aliasing, oversampling of the signal is suggested. A signal is called over-sampled by a factor of N if the sampling frequency is N times the Nyquist frequency. Undersampling leads to aliasing or also called frequency folding [114], which leads to frequency ambiguity

as the signal reconstructed from samples is different from the original continuous signal. Fig. 3.13 shows the sampling of a 60 Hz sinewave at a sample rate of 800 Hz and 70 Hz. The red dot exactly captures the sine wave; however, when the same signal is undersampled at 70 Hz, the reconstructed signal actually looks like 10 Hz cosine wave.

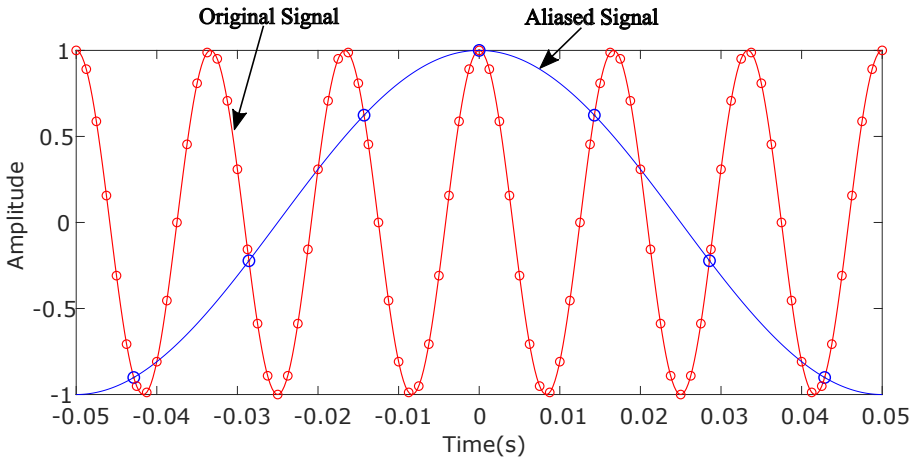

Figure 3.13: Comparison of actual signal with an aliased signal.

3.5.2 Signal filtering

Filtering in digital signal processing is performed to completely or partially suppress some aspect of the signal [114]. By removing the relevant frequency content from the spectrum, the interfering signals and/or background noise are reduced. Although filters block the energy in the band of frequencies they are designed for, they also attenuate signals in the passband frequency range. The task of filtering is simple yet invaluable in several fields. Some of the basic filter types are categorized into low-pass, high-pass, band-pass, and stopband, which are discussed next.

- **Low-pass filter**: This filter, as shown in Fig. 3.14(a) passes low frequencies and attenuates high frequencies, lower and higher than a selected cutoff frequency f_s, which is a part of the filter design.

- **High-pass filter**: Unlike a low pass filter, the high-pass filter shown in Fig. 3.14(b) passes high-frequency signal above the selected cutoff frequency f_s and attenuates signals with frequencies below the cutoff frequency.

- **Bandpass filter**: The bandpass filter passes the frequencies only in a specific region within the two cutoff frequencies f_1 and f_2 and attenuates frequencies outside this band. The filter information is shown in Fig. 3.14(c).

- **Stopband filter**: Unlike a bandpass filter, the stopband filter, which is shown in Fig. 3.14(d), attenuates the frequency within the cutoff frequency region f_1 and f_2 and passes the other frequencies unaltered.

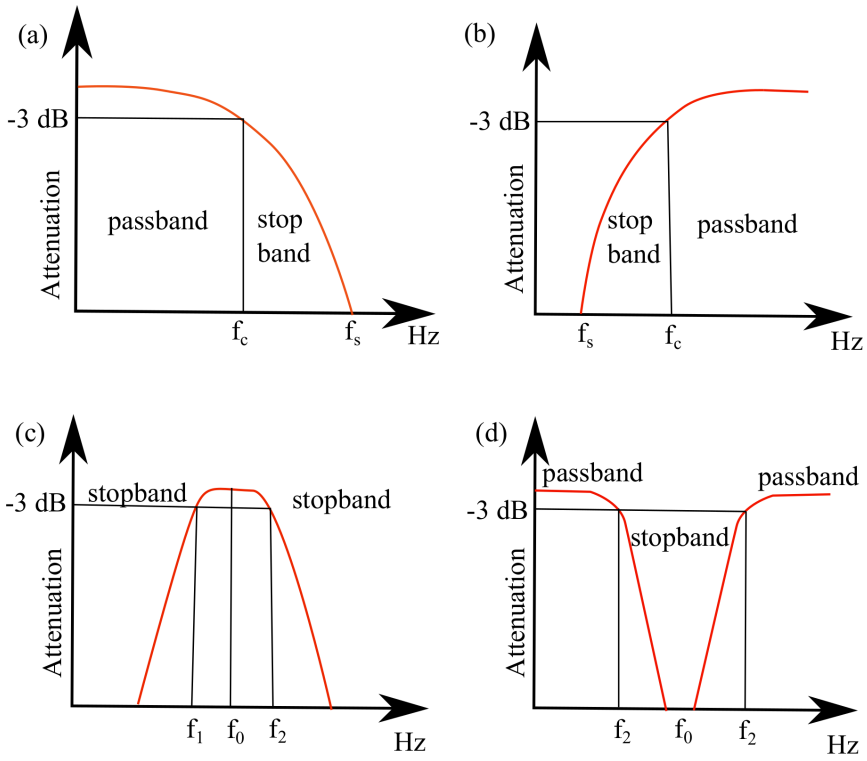

Figure 3.14: Schematic of the four basic Butterworth filters, (a) low pass; (b) high pass; (c) bandpass; (d) stopband

There are some terms used to describe the filter response cure [115]. The discussion of these terms are as follows:

- **-3 dB frequency**: This corresponds to the input frequency that causes the output signal to attenuate by -3dB compared to the input signal. The -3 dB frequency is also seen as a cutoff frequency where the output power is reduced by one-half (also called half-power frequency).

- **Center frequency** (f_0): This term is specifically used for bandpass and stopband filters to describe the frequency between the upper and lower cutoff frequencies. The central frequency f_0 is deduced from the geometric mean of lower f_1 and upper cutoff frequencies f_2.

- **Bandwidth**: This is the width of the passband (width of frequencies that does not experience significant attenuation).

- **Stopband frequency** f_s: The frequency at which the attenuation reaches a specified value is termed as stopband frequency. The frequency beyond the stopband frequency in the low pass and high pass filters is referred to as stopband, while the frequency between the two stopband frequencies in bandpass and stopband filters is known as stopband.

- **Quality factor** Q: The quality factor explains the damping characteristics of the filter. The damping refers to the number of oscillations in the system's step response in the time domain, whereas higher Q means more peaking in the system's magnitude. For bandpass and stopband filters, the Q is given by,

$$Q = \frac{f_0}{f_2 - f_1}. \tag{3.98}$$

3.5.3 Windowing

Windowing is the process of minimizing spectral leakage. Leakage happens when the signal information lies between two spectral lines in the DFT [114]. Such phenomena cause frequency content to move to other spectral regions and show discontinuities, resulting in spurious high frequency content. The window function smooths the signal over the edges, and windowing is the process of multiplying the signal by the window function of the same length [114]. There are many window functions used in signal processing. Some of the commonly used are discussed in this section.

The Rectangular window, also known as Dirichlet or boxcar window, is the simplest window and is equivalent to replacing all but N data points by zero. The function is given by,

$$w(n) = \left\{ \begin{array}{ll} 1, & \text{for } 0 \leq n \leq L-1 \\ 0, & \text{otherwise} \end{array} \right\},$$

where L is the length of the window.

The Hann window also referred to as Hanning, is given by,

$$w(n) = 0.5\,(1 - \cos(\frac{2\pi n}{L-1}),\ 0 \leq n \leq L-1. \tag{3.99}$$

The Hamming window with coefficients, α, and β are optimized to minimize the side lobe, resulting in a height of about one-fifth of the Hann window and is given by,

$$w(n) = \alpha - \beta\, cos(\frac{2\pi n}{L-1}), \tag{3.100}$$

where, $\alpha = 0.54$ and $\beta = 1 - \alpha = 0.46$.

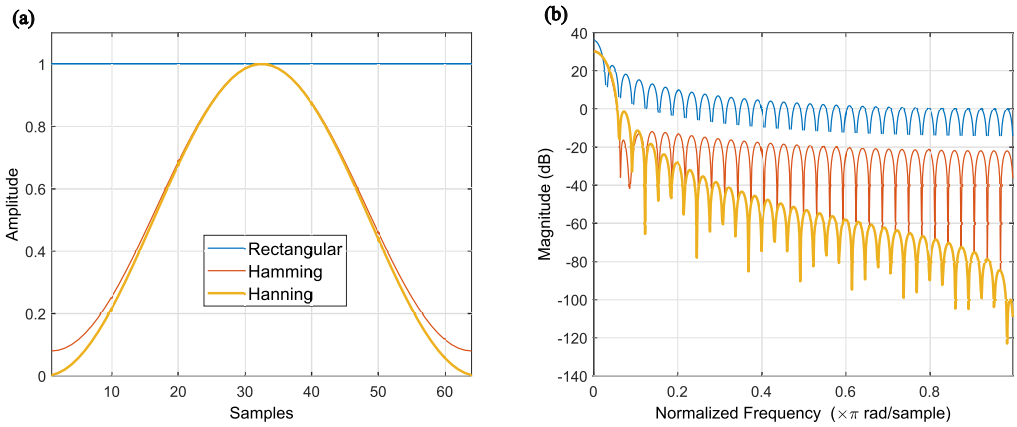

Figure 3.15: Comparison of three different window functions in (a) time domain; (b) frequency domain.

For a 64 point window length, the three window functions are shown in Fig. 3.15. The main lobe of the Hanning and Hamming windows is wider than the rectangular window, as seen in the frequency domain plot, and this reduces the energy of the leak frequency regions better. Hamming window is a commonly used window function because of the significant suppression of the first side lobe, which reduces the likelihood of losing individual peak in the spectrum.

3.5.4 Correlation and power spectral density (PSD)

Correlation techniques are powerful yet relatively easy to apply tools. The analysis based on autocorrelation and cross-correlation has been useful in many engineering fields to understand the spatial similarity between signals [116]. The power spectral density (PSD) typically used to characterize random broadband signals is a measure of the signal's power content in that frequency band. The amplitude of the PSD is generally normalized by the spectral resolution in the digitization the signal. For acoustic data, PSD has amplitude units of Pa^2/Hz. This section discusses the correlation functions and their relationship to spectral densities.

Auto-correlation and auto spectral density

The measure of the linear relationship of a variable with itself at differing time lags is the autocorrelation function [116]. Therefore, the peak of the autocorrelation function always occurs at zero lag. The autocorrelation function R_x in terms of expectations $E[\cdot]$ can be written as,

$$R_x(\tau) = E[x(t)x(t+\tau)], \tag{3.101}$$

where τ is the lag. In terms of integrals, this can be written as,

$$R_x(\tau) = \frac{1}{T_0}\int_{-\infty}^{\infty} x(t)x(t+\tau)dt, \tag{3.102}$$

The power spectral density (PSD) function $S_x(\omega)$ is defined as the Fourier transform of the auto-correlation function $R_x(\tau)$ and is given by,

$$S_x(\omega) = \int_{-\infty}^{\infty} R_x(\tau)e^{-j\omega\tau}d\tau. \tag{3.103}$$

Figure 3.16a shows the autocorrelation function of a 2 Hz sine wave with time lag exactly at zero, and the PSD of the autocorrelation is shown in Fig. 3.16b.

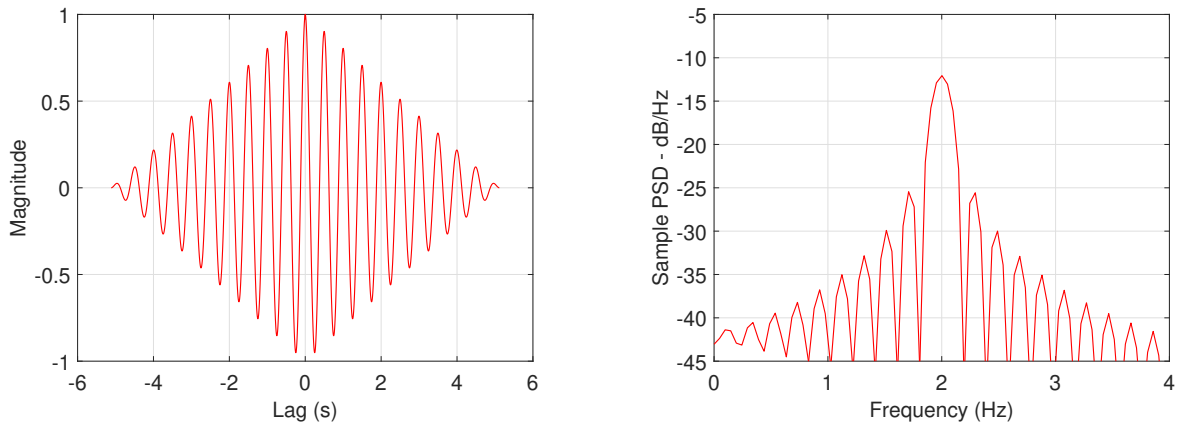

(a) (b)

Figure 3.16: Autocorrelation function of 2 Hz sine wave and the corresponding PSD

Cross-correlation and cross-spectral density

The correlation between two wave-forms represents the measure of similarity between them as a function of a time delay of one relative to the other [116]. The cross-correlation function $R_{xy}(\tau)$ between two time series $x(t)$ and $y(t)$ is given by,

$$\begin{aligned} R_{xy}(\tau) &= E[x(t)y(t+\tau)], \\ R_{yx}(\tau) &= E[y(t)x(t+\tau)], \end{aligned} \tag{3.104}$$

where τ is the lag. In terms of integrals, this can be written as,

$$R_{xy}(\tau) = \frac{1}{T_0}\int_{-\infty}^{\infty} x(t)y(t+\tau)dt, \tag{3.105}$$

As discussed later in the thesis, estimating τ is crucial to localizing leaks from acoustic data and is a part of most leak correlation algorithms in the literature.

The cross power spectral density $S_{xy}(\omega)$ is the Fourier transform of the cross-correlation function $R_{xy}(\tau)$ given by,

$$S_{xy}(\omega) = \int_{-\infty}^{\infty} R_{xy}(\tau)e^{-j\omega\tau}d\tau. \tag{3.106}$$

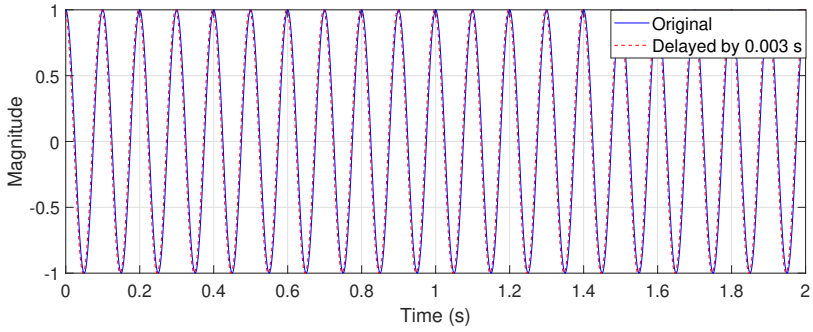

(a)

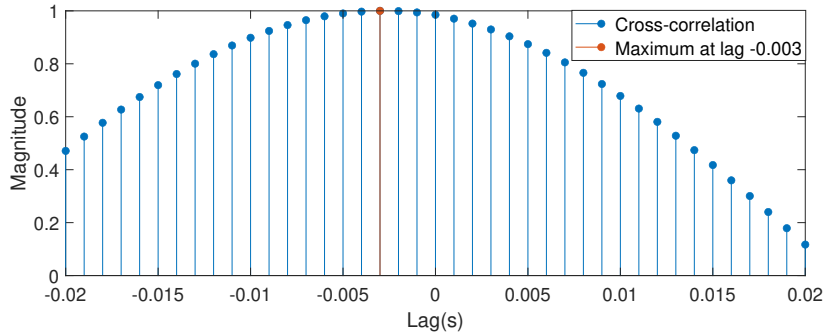

(b)

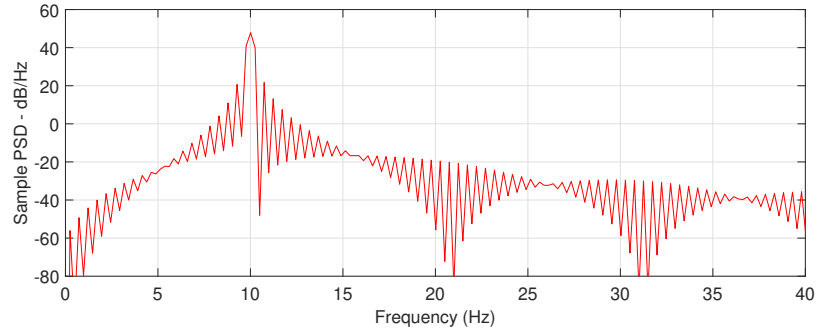

(c)

Figure 3.17: (a) Time series of 10 Hz cosine wave compared to its 0.003 s delayed version; (b) corresponding cross-correlation function; (c) PSD of the cross-correlation function

Figure 3.17 shows a sample of the cross-correlation function and the PSD associated with a 10 Hz cosine wave. The time series of the cosine wave with its delayed version (0.003 s)

is shown in Fig. 3.17a. The cross-correlation function shown in Fig. 3.17b exactly shows the delay with a maximum spike at 0.003 s. The signal power content can be observed in the PSD shown in Fig. 3.17c.

Parseval's theorem is one of the important theorems in signal processing, which states that the integrated energy in the time domain is equal to integrated energy in the frequency domain and is given by,

$$\int_{-\infty}^{\infty} x^2(t)dt = \int_{-\infty}^{\infty} |X(\omega)|^2 d\omega. \tag{3.107}$$

3.5.5 Coherence and unwrapped phase

Coherence is a statistic used to investigate the relationship between recorded signals [117]. The coherence function closer to 1 implies that the two signals are related and indicate a high signal to noise ratio [118]. The coherence between two signals $x(t)$ and $y(t)$ is a real-valued function which is defined as,

$$C_{xy}(\omega) = \frac{|S_{xy}(\omega)|^2}{S_x(\omega)S_y(\omega)}. \tag{3.108}$$

The amplitude of the spectral density is indicated by $|S|$. The coherence values are between $0 \leq C_{xy}(f) \leq 1$, and for an ideal constant parameter, single input $x(t)$ and single output $y(t)$ linear system, the coherence is always equal to one.

In the areas where there is signal modulation due to the presence of one or more signals, the phase unwrapping technique is used to extract the information of the signals. The wrapped phase is limited to the interval of 2π radians [117]. The phase can be unwrapped from the wrapped phase by removing 2π discontinuities [119]. The phase unwrapping uses a transfer function that gives the information of complex-valued pressure recorded at one location relative to the second one. The pressure $\boldsymbol{p}$ in terms of amplitude $\boldsymbol{P}$ and phase is given by:

$$\boldsymbol{p} = \boldsymbol{P}(\omega)e^{j\phi(\omega)}, \tag{3.109}$$

where ϕ is the relative shift of waves of the same frequency.

For illustration, the time signals shown in Fig. 3.17a, Eq. 3.108 are used to estimate the coherence function which is then used to estimate the unwrapped phase. The coherence function and the unwrapped phase of the time series are shown in Fig. 3.18. The maximum

coherence value in Fig. 3.18a can be seen at 10 Hz, and the unwrapped phase of the function is shown in Fig. 3.18b. The delay between the two signals can be estimated using the gradient of the unwrapped phase in the maximum coherence region, which is found as 0.003 s (this is the exact delay between two signals).

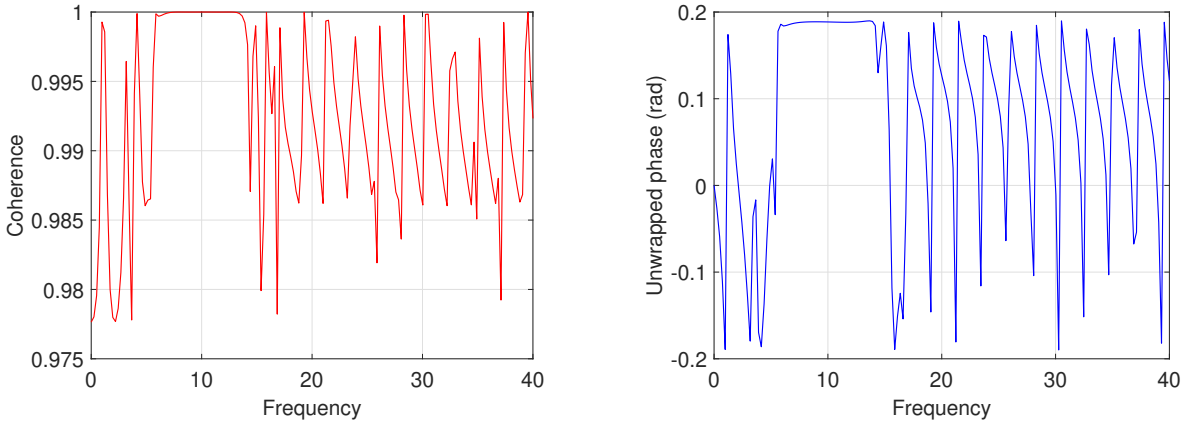

(a) (b)

Figure 3.18: (a) Coherence function; (b) unwrapped phase of the 10 Hz cosine wave auto-spectral and cross spectral density.

3.6 Summary

In this chapter, the theoretical framework for the acoustic wave equation is developed. First, the formulation for the speed of sound in pipes is shown, which is then used in obtaining normal modes and natural frequencies of the acoustic plane wave. The acoustic wave equation is then derived for studying the reflection and transmission of plane waves and their relationship to impedance. Several basics of signal processing that are used throughout the thesis are also presented.

Chapter 4

Methodology for Leak Detection and Localization

This thesis deals with the problem of leak detection and localization using acoustic signals in both single pipe and more complex pipe networks. While there are distinct differences in these cases and in active versus passive methods, there are also standard techniques and algorithms which have been developed in this thesis to facilitate key tasks such as time delay and wave speed estimation. These quantities are further processed to address the unique challenges in single pipe and pipe network situations.

This chapter will establish the theoretical framework of signal decomposition theories which allows for estimating time delays from the reflected waves, which is critical for the active case. Leak introduces an impedance discontinuity, which causes part of the incident wave to reflect. Quantities such as the power reflection coefficient, which is derived from leak impedance, can be used as a reliable leak indicator. Furthermore, from the decomposed wave, a comparison of estimates such as the reflected spectral waves and transmission loss with its baseline also yields other leak surrogates. Tools such as the two microphone technique can help with signal decomposition and extracting leak-sensitive features.

Moreover, the reflected waves due to leaks can be processed to extract relevant time delays due to impedance changes in the propagation path. Robust estimation of time delay(s) prevalent in the system is central to leak localization. Conventional means of localization is through the study of time difference obtained using the cross-correlation function. However, this technique is not suitable with the active method as the source generated signal dominates the acoustic energy received at the receivers, which renders delineating leak induced time delay from other time delays in the system challenging. Therefore, tech-

niques such as Prony's, matrix pencil method (MPM), and mean shift clustering (MSC) are employed, and with the statistical treatment of the time delays the prediction of a leak location is made possible.

Finally, the multilateration techniques widely employed in mobile networking and the global positioning systems, are applied to the problem of leak localization in lab-based WDNs. Due to the multiple acoustic paths in WDNs, using time delay alone is not sufficient to localize. Hence, combining numerous time delays obtained from Prony's or MPM method with multilateration is shown to improve the localization accuracy in such non-line of sight situations.

This chapter is divided into two main sections, detection and localization. The theoretical and algorithmic frameworks used for leak detection are discussed in Section 4.1, while for localization in Section 4.2.

4.1 Leak Detection Methods and Indicators

4.1.1 Power transmission and reflection coefficient

The power transmission T_{Π} and reflection coefficient R_{Π} are powerful leak indicators, which can be obtained from either one or two sensors to determine the presence of a leak. Background on these indicators have already been described in Sections 3.4.3 and 3.4.4. The coefficients are simply a function of the leak diameter a and cross-sectional area of the pipe S, as shown in Eq. 3.88. The underlying principle is that if there is a leak present in the system, then the fraction of the reflected or transmitted wave is a function of the leak and pipe dimensions. If the sensor is upstream of the leak, the total acoustic energy increases at that sensor and vice-versa. The power coefficients thus, serve as a leak indicator and also could provide information where the leak may be present (i.e., if the magnitude of acoustic pressure is higher when compared to the baseline, then the leak is downstream of the sensor position and vice versa).

4.1.2 Power spectral densities

The mechanical behavior of the pipe and the acoustic source affects the resonance of the combined system as shown in Eq. 3.77. The impedance change due to leak affects the overall impedance of the pipe $\boldsymbol{Z}_{m0}$, which in turn affects the overall pipe-driver system, requiring the driver to compensate with a change in the force $\boldsymbol{f}$ to drive the piezo-ceramic

of the acoustic source. The power spectral density (PSD) that measures the signal's power content at different frequencies can hence be used as a proxy for detecting a leak. The potential of PSD as a leak index in simple and moderately complex WDNs is verified using experiments in chapters 5 and 6.

4.1.3 Reflected spectral waves and transmission loss

Consider a driver-pipe system as shown in Fig. 4.1 where the pipe is driven at one end using a source and closed at the other end by a rigid cap whose impedance is given by Z_c. The end cap impedance reflects the incident wave, and the total acoustic pressure can be decomposed into the incident and reflected components. Similar to the end-cap impedance, the leak impedance also reflects the incident wave, and the reflected component due to leak can be used as a leak indicator. The two microphone technique (requires at least two sensors) is able to decompose the total pressure wave into its constituent parts and the details are shown next. The transmission loss, which is the ratio of the incident portion of the wave upstream to the downstream segment, is also a byproduct of this method which can be used to indicate the presence of a leak.

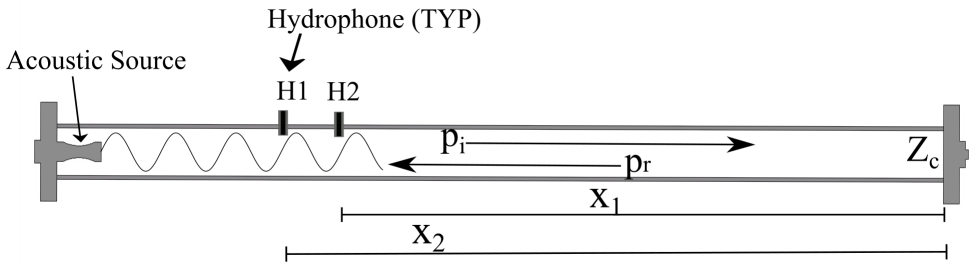

Figure 4.1: Schematic of pipe excited by a source for two microphone technique

Two microphone technique

The determination of acoustic properties, specifically the normal acoustic impedance and the reflection coefficient of a tube from acoustic measurements was first successfully performed using random excitation by Seybert et al. [112], called the two-microphone technique. At the core of this method is the estimation of the auto and cross-spectral densities of sound pressure measured using microphones at two measurement points, which are then used to solve for the acoustic impedance. Using Eq. 3.58, the total acoustic pressure at

two measurement locations given by x_1 x_2 shown in Fig. 4.1 can be written in the form of the incident and reflected pressures as Eq. 4.1. For the ease of expressing the equations later, $\boldsymbol{P}_i$ and $\boldsymbol{P}_r$ are written as $\tilde{i}(t)$ and $\tilde{r}(t)$, respectively.

$$\begin{aligned}\boldsymbol{p}(x_1,t) &= \boldsymbol{p}_i(x_1,t) + \boldsymbol{p}_r(x_1,t) = \left[\tilde{i}(t)e^{-jk_ix_1} + \tilde{r}(t)e^{jk_rx_1}\right]e^{j\omega t} \\ \boldsymbol{p}(x_2,t) &= \boldsymbol{p}_i(x_2,t) + \boldsymbol{p}_r(x_2,t) = \left[\tilde{i}(t)e^{-jk_ix_2} + \tilde{r}(t)e^{jk_rx_2}\right]e^{j\omega t}.\end{aligned} \tag{4.1}$$

The particle velocity is given by Eq. 3.55 and stated here again as,

$$\vec{\boldsymbol{u}} = \frac{\tilde{i}(t)e^{j(\omega t - k_+x)} - \tilde{r}(t)e^{j(\omega t + k_-x)}}{\rho_0 c}. \tag{4.2}$$

For flow with motion, the incident k_i and reflected k_r wave numbers are given as:

$$k_i = \frac{\omega}{c+v} = \frac{k}{1+M}, \quad \text{for wave motion with flow} \tag{4.3}$$

$$k_r = \frac{\omega}{c-v} = \frac{k}{1-M}, \quad \text{for wave motion against flow} \tag{4.4}$$

where, $M = v/c$ is the Mach number and v is the velocity of the flow.

The impedance $\boldsymbol{Z}_c(f)$ can be regarded as a linear system which is a function of particle velocity and total pressure. Thus, the impedance can be expressed in the form of spectral densities as,

$$\boldsymbol{Z}_c(f) = \frac{\hat{S}_{pu}(f)}{\hat{S}_{uu}(f)}, \tag{4.5}$$

where $\hat{S}_{pu}(f)$ is the cross-spectral density between pressure and particle velocity and $\hat{S}_{uu}(f)$ is the auto-spectral density of particle velocity.

These spectral are estimated as

$$\begin{aligned}\hat{S}_{pu}(f) &= \frac{1}{T}\left\{P_0(f,T)U_0^*(f,T)\right\}. \\ \hat{S}_{pp}(f) &= \frac{1}{T}\left\{P_0(f,T)P_0^*(f,T)\right\}. \\ \hat{S}_{uu}(f) &= \frac{1}{T}\left\{U_0(f,T)U_0^*(f,T)\right\}.\end{aligned} \tag{4.6}$$

The $P_0(f,T)$ and $U_0(f,T)$ are the Fourier transforms of the pressure and particle velocity time signal, T is the total recorded time signal length and the asterisk $*$ represents the complex conjugate.

The total pressure given by Eq. 4.1, and particle velocity shown in Eq. 4.2 is represented in the frequency domain in the form of,

$$\begin{aligned} \boldsymbol{P}(f,T) &= I(f,T) + R(f,T). \\ \boldsymbol{U}(f,T) &= (I(f,T) - R(f,T))\frac{1}{\rho_0 c}. \end{aligned} \tag{4.7}$$

Substituting Eq. 4.7 in Eq. 4.6 gives

$$\begin{aligned} \hat{S}_{pu}(f) &= \frac{1}{\rho_0 c}\Big[\hat{S}_{II}(f) - \hat{S}_{RR}(f) - j\,2\,\hat{Q}_{IR}(f)\Big], \\ \hat{S}_{pp}(f) &= \Big[\hat{S}_{II}(f) + \hat{S}_{RR}(f) + 2\,\hat{C}_{IR}(f)\Big], \\ \hat{S}_{uu}(f) &= \Big(\frac{1}{\rho_0 c}\Big)^2\Big[\hat{S}_{II}(f) - \hat{S}_{RR}(f) - 2\,\hat{C}_{IR}(f)\Big], \end{aligned} \tag{4.8}$$

where, $\hat{S}_{II}(f)$ and $\hat{S}_{RR}(f)$ are auto-spectral densities of the incident and reflected waves, respectively and $\hat{C}_{IR}(f)$ and $\hat{Q}_{IR}(f)$ are the real and imaginary components of the cross-spectral density $\hat{S}_{IR}(f)$ between the incident and the reflected waves.

Thus, substituting Eq. 4.8 in Eq. 4.5,

$$\frac{\boldsymbol{Z}_c(f)}{\rho_0 c} = \frac{\hat{S}_{II}(f) - \hat{S}_{RR}(f) - j\,2\,\hat{Q}_{IR}(f)}{\hat{S}_{II}(f) + \hat{S}_{RR}(f) - 2\,\hat{C}_{IR}(f)}, \tag{4.9}$$

$$\frac{\boldsymbol{R}_c(f)}{\rho_0 c} = \frac{\hat{S}_{II}(f) - \hat{S}_{RR}(f)}{\hat{S}_{II}(f) + \hat{S}_{RR}(f) - 2\,\hat{C}_{IR}(f)}, \tag{4.10}$$

$$\frac{\boldsymbol{X}_c(f)}{\rho_0 c} = \frac{-2\,\hat{Q}_{IR}(f)}{\hat{S}_{II}(f) + \hat{S}_{RR}(f) - 2\,\hat{C}_{IR}(f)}, \tag{4.11}$$

where $\boldsymbol{R}_c(f)$ and $\boldsymbol{X}_c(f)$ are the resistive and reactive impedance, respectively.

As shown in Fig. 4.1, if the measurements of acoustic pressure are conducted at two points x_1 and x_2, the quantities $\hat{S}_{11}(f)$, $\hat{S}_{22}(f)$, $\hat{C}_{12}(f)$ and $\hat{Q}_{12}(f)$ can be estimated from

time signal. $\hat{S}_{11}(f)$ and $\hat{S}_{22}(f)$ are the auto-spectral densities of pressure at x_1 and x_2, respectively while $\hat{S}_{12}(f)$ is the cross-spectral density between x_1 and x_2. The auto and cross spectral density estimates can be written in the frequency domain as,

$$\begin{aligned}
\hat{S}_{11}(f) &= \frac{1}{T}\left\{P_1(f,T)P_1^*(f,T)\right\}, \\
\hat{S}_{22}(f) &= \frac{1}{T}\left\{P_2(f,T)P_2^*(f,T)\right\}, \\
\hat{S}_{12}(f) &= \hat{C}_{12}(f) + j\,\hat{Q}_{12}(f) = \frac{1}{T}\left\{P_1(f,T)P_2^*(f,T),\right\},
\end{aligned} \tag{4.12}$$

where $P_1(f,T)$ and $P_2(f,T)$ are the finite Fourier transforms of the acoustic pressures at x_1 and x_2 and the asterisk $*$ represents the complex conjugate. $\hat{C}_{12}(f)$ and $\hat{Q}_{12}(f)$ are the real and imaginary components of the cross spectral density $\hat{S}_{12}(f)$.

Therefore, by taking the Fourier transform of Eq. 4.1 and combining with Eq. 4.12, the relationship between the auto and cross spectral densities at x_1 and x_2 and the reflected and incident spectral densities can be obtained which are shown in,

$$\begin{aligned}
\hat{S}_{11}(f) &= \hat{S}_{II}(f) + \hat{S}_{RR}(f) + 2\Big[\hat{C}_{IR}(f)\cos(k_i+k_r)x_1 + \hat{Q}_{IR}(f)\sin(k_i+k_r)x_1\Big] \\
\hat{S}_{22}(f) &= \hat{S}_{II}(f) + \hat{S}_{RR}(f) + 2\Big[\hat{C}_{IR}(f)\cos(k_i+k_r)x_2 + \hat{Q}_{IR}(f)\sin(k_i+k_r)x_2\Big] \\
\hat{C}_{12}(f) &= \hat{S}_{II}(f)\cos k_i(x_1-x_2) + \hat{S}_{RR}(f)\cos k_r(x_1-x_2) + \hat{C}_{IR}(f)\Big[\cos(k_r x_1 + \\
&\quad k_i x_2) + \cos(k_i x_1 + k_r x_2)\Big] + \hat{Q}_{IR}(f)\Big[\sin(k_r x_1 + k_i x_2) + \sin(k_i x_1 + k_r x_2)\Big] \\
\hat{Q}_{12}(f) &= -\hat{S}_{II}(f)\sin k_i(x_1-x_2) + \hat{S}_{RR}(f)\sin k_r(x_1-x_2) + \hat{C}_{IR}(f)\Big[-\sin(k_i x_1 + \\
&\quad k_r x_2) + \sin(k_r x_1 + k_i x_2)\Big] + \hat{Q}_{IR}(f)\Big[\cos(k_i x_1 + k_r x_2) - \cos(k_r x_1 + k_i x_2)\Big].
\end{aligned} \tag{4.13}$$

Solving the above equation for $\hat{S}_{II}(f)$, $\hat{S}_{RR}(f)$ and $\hat{S}_{IR}(f)$, the impedance of the system can be estimated using Eq. 4.9.

If the tube has an-echoic termination and a third microphone is located downstream of the system under study, the spectral density of the transmitted wave $\hat{S}_{TT}(f)$ can be measured directly, and the transmission loss can be obtained by taking the ratio of the two quantities, $\hat{S}_{II}(f)$ and $\hat{S}_{TT}(f)$. However, suppose the termination is not an-echoic. In that case, two microphones can be placed downstream, and their measurements can be processed using the previously described decomposition method to obtain the appropriate (incident

portions in the upstream and downstream segments) transmitted wave spectral density. The transmission loss then can be computed using,

$$TL = 10 \log_{10} \Big[\frac{\hat{S}_{II}(f)}{\hat{S}_{TT}(f)} \Big]. \tag{4.14}$$

Chung et al. [120, 121] proposed a transfer function formulation obtained from the sound pressure measurements for signal decomposition. In addition, a sensor switching method was proposed by the authors to calibrate the sensors automatically. In a subsequent paper by [122], it was shown that the transfer function method and the decomposition method where the incident and reflected wave auto and cross spectra are obtained from the set of decomposition equations yield identical results. In fact, the wave decomposition method provides more insight into the results of decomposition compared to the transfer function representation. The aforementioned papers were originally implemented on air-filled ducts; however, the techniques were later applied to water-filled pipes as well [123, 124], but not for leak detection. To the authors' knowledge, the application of these techniques for the leak detection application is new and is being proposed for the first time in this study. The results associated to this is discussed in Section 5.3.2.

That being said, the shortcoming of this method for use in leak detection is its very laborious experimental setup and the need for multiple sensors. The technique is successfully demonstrated in a single pipe setup; however, the idea is not carried forward to WDNs because of the complexity of the network and multiple impedance changes, each requiring at least two sensors.

The ensuing sections focus on localization. For typical experimental pipe configurations, the task of monitoring and pin-pointing the leak location can be accomplished once all the time delays in the system are estimated and the acoustic wave speed is known, provided the time delays associated with the reflections from the leak can be delineated from the remaining delays at various impedance changes, or with respect to a baseline without a leak present. The theory and the methodology associated with obtaining leak-induced time delay using Prony's, MPM, and time-frequency-based methods are discussed next.

4.2 Leak Localization Methods based on Time Delay Estimation

Time delay estimation is the primary goal and key to various localization techniques including for cross-correlation, which is used extensively in this thesis. The cross-correlation function between two measured signals (acceleration or acoustic pressure) approximates the time delay, which in conjunction with wave speed c and distance between two sensors, gives the location of a leak. Features such as cepstrum, which is the inverse of the Fourier transform of the logarithm of the Fourier transform, can be used to detect transient events and time of reflection, which can be used for localization [91, 90, 75, 93]. The importance of estimating this parameter has long been recognized in the literature [125, 126].

Unlike for the passive case, the source produces the excitation in the active approach, and hence the first peak in the cross-correlation cannot be assumed to be leak induced. If the two sensors are placed close to each other, then the highest spike in the cross-correlation may be associated with the direct transmission of the wave between the sensors. This poses a challenge as it is not trivial to unmask the time delay induced due to the leak; often, the approach is to compare leak data with the baseline data to determine the leak-induced time delay (which manifest as changes).

Assume that the acoustic path between two points inside a linear pipe segment (Fig. 4.2) corresponding to measurements $x_1(t)$ and $x_2(t)$ is non-dispersive (velocity independent of frequency) and that the paths are associated with constant gains, H_k. Assume that the plane waves are generated at one end using a device. The acoustic propagation in the fluid medium contains multi-paths, including direct transmission and reflections, and the various arrival times associated with these multiple paths are separated by τ_k. Assume that the signal x_2 can be described in terms of x_1 as a linear superposition of r time-delayed harmonics $x_1(t)$ and a random measurement error ϵ:

$$x_2(t) = \sum_{k=1}^{r} H_k x_1(t - \tau_k) + \epsilon \tag{4.15}$$

The cross-correlation between $x_1(t)$ and $x_2(t)$ can be written as (with the assumption ϵ is uncorrelated to x_1) as.

$$R_{x_1x_2}(\tau) = \sum_{k=1}^{r} H_k R_{x_1x_1}(t - \tau_k). \tag{4.16}$$

Eq. 4.16 states that the cross-correlation function is a linear superposition of autocorrelation function of x_1, each component offset by τ_k, $k = 1, \cdots, r$. For the case when x_1 is a

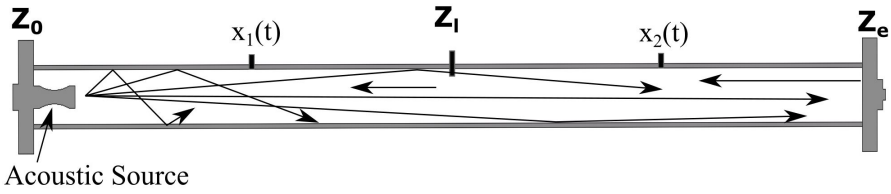

Figure 4.2: Sound propagation along multiple paths between x_1 and x_2

spectrally white, $R_{x_1x_2}(\tau)$ results in a linear combination of Dirac delta functions $\delta(t-\tau_k)$, localized at τ_k. This is a trivial case where the individual time delays in the linear mixture can be easily resolved. However, for the case of a plane wave traveling inside a pressurized pipe, x_1 is a narrow-band process, which is governed by the fundamental resonances of the fluid-pipe-driver system [103]. When the minimum separation time is greater than the time span of the autocorrelation function, the individual peaks in the cross-correlation function can be resolved by solving r individual estimation problems, each yielding a time delay.

The next section presents three methods and their theoretical background that resolves the signal containing multiple damped harmonics associated with reflections (due to various impedance change) to extract the time delay due to a leak. The three methods namely Prony's, matrix pencil and mean-shift clustering are discussed in Section 4.2.1, 4.2.2, and 4.2.3, respectively.

4.2.1 Prony's method

For a fluid-filled pipe excited by broadband or narrowband excitation, Prony's method provides a powerful estimation framework to express functions which are a superposition of a finite number of damped sinusoids [127]. Prony's method yields estimates for the magnitude, frequency, phase, and damping of each individual sinusoid comprising the filtered signal. Assume that $R_{x_1x_2}[n]$ $(n = 1, 2, ...N)$ is a sampled version of an equally spaced time series obtained using the cross-correlation between acoustic pressure measurements x_1 and x_2. Prony's approximation can be used for a time series with p damped harmonics written in the form of [127]:

$$R_{x_1x_2}[n] = \sum_{k=1}^{p} h_k.z_k^{(n-1)}, \tag{4.17}$$

where, $h_k = A_k e^{j\phi_k}$, $z_k^{(n-1)} = e^{(\alpha_k + j2\pi f_k)T_s(n-1)}$, T_s is the sample time; f_k is the frequency in cycles per second; ϕ_k is the phase of the k^{th} component; and α_k is the damping coefficient

of the k^{th} component. The vector A of length p represents the individual sinusoid amplitudes. The procedure to estimate these parameters, along with the frequencies, phase, and damping coefficients, are discussed next.

In general, several repetitions of the experiments are conducted, and identically shaped excitation is used to excite the fluid pipe system. As long as the time interval between such repetitions is long enough such that the acoustic energy in the medium has died out, each experiment can be considered as an independent trial, and the results can be treated using standard statistical techniques. Mathematically, such an ensemble of N experiments can be written using Prony's approximation as,

$$\{R_{x_1x_2}[n]\}_i = \{\sum_{k=1}^{p} h_k.z_k^{(n-1)}\}_i; \quad i = 1, \cdots, N. \tag{4.18}$$

The results then contain N estimates of the phase ϕ_k, which can be treated using standard statistical techniques. The Prony analysis computes h_k and z_k of Eq. 4.20 in basic four steps as shown below.

1. The first step is to solve the linear prediction model constructed by the observed data set and obtain coefficients $a[1]....a[p]$ of the characteristics polynomial. The p-order model assumes that the value of $x[n]$ depends linearly on the previous p values in x and can be written as,

$$x[n] = \sum_{k=1}^{p} a_k x[n-k], \tag{4.19}$$

and in the matrix form as:

$$\begin{bmatrix} x[p] & x[p-1] & \dots & x[1] \\ x[p+1] & x[p] & \dots & x[2] \\ \vdots & \vdots & \ddots & \vdots \\ x[2p-1] & x[2p-2] & \dots & x[p] \end{bmatrix} \begin{bmatrix} a_1 \\ a_2 \\ \vdots \\ a_p \end{bmatrix} = - \begin{bmatrix} x[p+1] \\ x[p+2] \\ \vdots \\ x[2p] \end{bmatrix}. \tag{4.20}$$

Solving the above equation gives the value of coefficient a of the Prony polynomial $\psi(z)$. If the above matrix is a square matrix, the backslash operator solves the above equation. With the over-determined system, the least squares (LS) or the total least square (TLS) scheme can be used.

2. Secondly, the roots of the characteristic or Prony polynomial formed from the linear prediction coefficients is obtained as.

$$\psi(z) = z^p + a_1 z^{p-1} + ... + a_p. \tag{4.21}$$

As vector a is known, the zeros of the polynomial $\psi(z)$ shown in Eq. 4.21 are solved whose roots are the unknown exponents z_k. Now, with known z_k, damping factor (α_k) and frequency (f_k) can be obtained using,

$$\alpha_k = \frac{ln|z_k|}{T_s}, \tag{4.22}$$

and

$$f_k = \frac{tan^{-1}[\frac{Im(z_k)}{Re(z_k)}]}{2\pi T_s}. \tag{4.23}$$

3. Then solve the original set of equations to obtain the estimates of the exponential amplitude and sinusoidal phase as shown in,

$$\begin{bmatrix} z_1^0 & z_2^0 & \dots & z_p^0 \\ z_1^1 & z_2^1 & \dots & z_p^1 \\ \vdots & \vdots & \ddots & \vdots \\ z_1^{p-1} & z_2^{p-1} & \dots & z_p^{p-1} \end{bmatrix} \begin{bmatrix} h_1 \\ h_2 \\ \vdots \\ h_p \end{bmatrix} = \begin{bmatrix} x[1] \\ x[2] \\ \vdots \\ x[p] \end{bmatrix}. \tag{4.24}$$

4. Finally, with known h_k, solve for the amplitude (A_k) and phase (ϕ_k) using equations shown in,

$$A_k = |h_k|, \tag{4.25}$$

and

$$\phi_k = \frac{Im(h_k)}{Re(h_k)}. \tag{4.26}$$

The order p of the polynomial, which is unknown, is estimated using minimum subset error [128]. While solving using Prony's method, the prediction order L, which is larger than the real order p is chosen. This gives a set of L exponentials out of which the best subset of size p is determined. The subset of p best approximates the observed data using the least-squares criterion. All the possible subset $\begin{bmatrix} L \\ p \end{bmatrix}$ of size p with the corresponding minimum error E_p can be obtained. The value of p for which E_p shows the significant drop in rate of decrease is taken as the correct order p.

4.2.2 Matrix pencil method (MPM)

MPM is a robust technique to decompose the superimposed signal into a sum of complex exponentials. Assume that x_m $(m = 0, 1, ...N-1)$ is a sampled version of an equally spaced time series (e.g., acoustic pressure). MPM can be used to estimate signal parameters from the response signal consisting of L damped harmonics described by ([129, 130]),

$$\begin{aligned} x_m &= y_m + n_m, \\ &= \sum_{k=1}^{L} A_k e^{((\alpha_k + j\omega_k)m + j\phi_k)} + n_m, \end{aligned} \tag{4.27}$$

where, y_m is the signal and n_m is the noise. The vector A of length L represents the sinusoid's complex amplitude. α_k is the damping coefficient of the k-th component; ω_k is the angular frequency in radians per second, and ϕ_k is the phase of the k-th component. These parameters are found using the generalized eigenvalue method, which can then be further studied for leak detection and localization.

Steps 1 and 2 of Prony's method generate the roots of the characteristic polynomial that coincide with the signal poles z_k. The other approach to arrive at the same solution is to use the MPM to find z_k directly by solving a generalized eigenvalue problem. To implement MPM, a rectangular Hankel matrix $\boldsymbol{Y}$ is constructed from the signal (x[n], n =1,... N), where L is the pencil parameter in this method.

$$\boldsymbol{Y} = \begin{bmatrix} x[1] & x[2] & \dots & x[L] & x[L+1] \\ x[2] & x[3] & \dots & x[L+1] & x[L+2] \\ \vdots & \vdots & \ddots & \vdots & \vdots \\ x[N-L] & x[N-L+1] & \dots & x[N-1] & x[N] \end{bmatrix}_{(N-L)\times(L+1)} \tag{4.28}$$

The matrix $\boldsymbol{Y}$ in Eq. 4.28 is used to create matrices $\boldsymbol{Y}_1$ and $\boldsymbol{Y}_2$. $\boldsymbol{Y}_1$ is formed by eliminating the last column of $\boldsymbol{Y}$ whereas while $\boldsymbol{Y}_2$ is obtained by eliminating the first column of $\boldsymbol{Y}$. The matrix $\boldsymbol{Y}_1$ and $\boldsymbol{Y}_2$ are shown in Eqs. 4.29 and 4.30, respectively.

$$\boldsymbol{Y}_1 = \begin{bmatrix} x[1] & x[2] & \dots & x[L] \\ x[2] & x[3] & \dots & x[L+1] \\ \vdots & \vdots & \ddots & \vdots \\ x[N-p] & x[N-L+1] & \dots & x[N-1] \end{bmatrix}_{(N-L)\times(L)} \tag{4.29}$$

$$\boldsymbol{Y}_2 = \begin{bmatrix} x[2] & \dots & x[L] & x[L+1] \\ x[3] & \dots & x[L+1] & x[L+2] \\ \vdots & \ddots & \vdots & \vdots \\ x[N-L+1] & \dots & x[N-1] & x[N] \end{bmatrix}_{(N-L)\times(L+1)} \tag{4.30}$$

The efficient way to solve the matrix is by solving the eigenvalue given by the expression,

$$z_k = eigenvalues(\boldsymbol{Y}_1^{+}\boldsymbol{Y}_1), \tag{4.31}$$

where $\boldsymbol{Y}_1^{+}$ is the Moore-Penrose pseudoinverse matrix of $\boldsymbol{Y}_1$, as defined in,

$$\boldsymbol{Y}_1^{+} = [\boldsymbol{Y}_1^{H}\boldsymbol{Y}_1]^{-1}\boldsymbol{Y}_1^{H}. \tag{4.32}$$

The values z_k, then yield the parameters α_k and frequency f_k similar to Prony's method. The final step coincides with Step 3 of the Prony polynomial method which is solving the system equation as shown in Eq. 4.24 to obtain A_k and θ_k.

Procedure for leak detection and localization using Prony's method and MPM

Prony's method or MPM can both be used to estimate the time delays in a signal containing multiple damped harmonics associated with reflections associated with various impedance changes and paths in a segment of a pipe. For a set of aggregated leak and no-leak hydrophone data, each signal is filtered to remove very low-frequency signal components (< 5 Hz) corresponding to operational pressure variations. The cross-correlation function from a pair of signals (x_1 and x_2) is obtained, and Prony's method or MPM is applied to decompose the signal into a series of complex exponentials. Prony's steps to estimate the parameters are summarized in Section 4.2.1 while the MPM steps are shown in Section 4.2.2. The flowchart for both the methodology for leak detection and localization is shown in Fig. 4.3. The order of p is determined based on the minimum subset error [128] and the value of p for which the minimum error shows a significant drop in the rate of decrease is used to calculate the frequency and phase of each exponential. The group time delays are then estimated to generate the histogram along with the cumulative distribution function (CDF) and the Kolmogorov-Smirnov (KS) statistics [131], which quantifies the maximum distance between the empirical distribution functions of two samples. These parameters for the leak case are compared with the no-leak baseline case for leak detection and localization. The time delay corresponding to the leak is used with the experimental

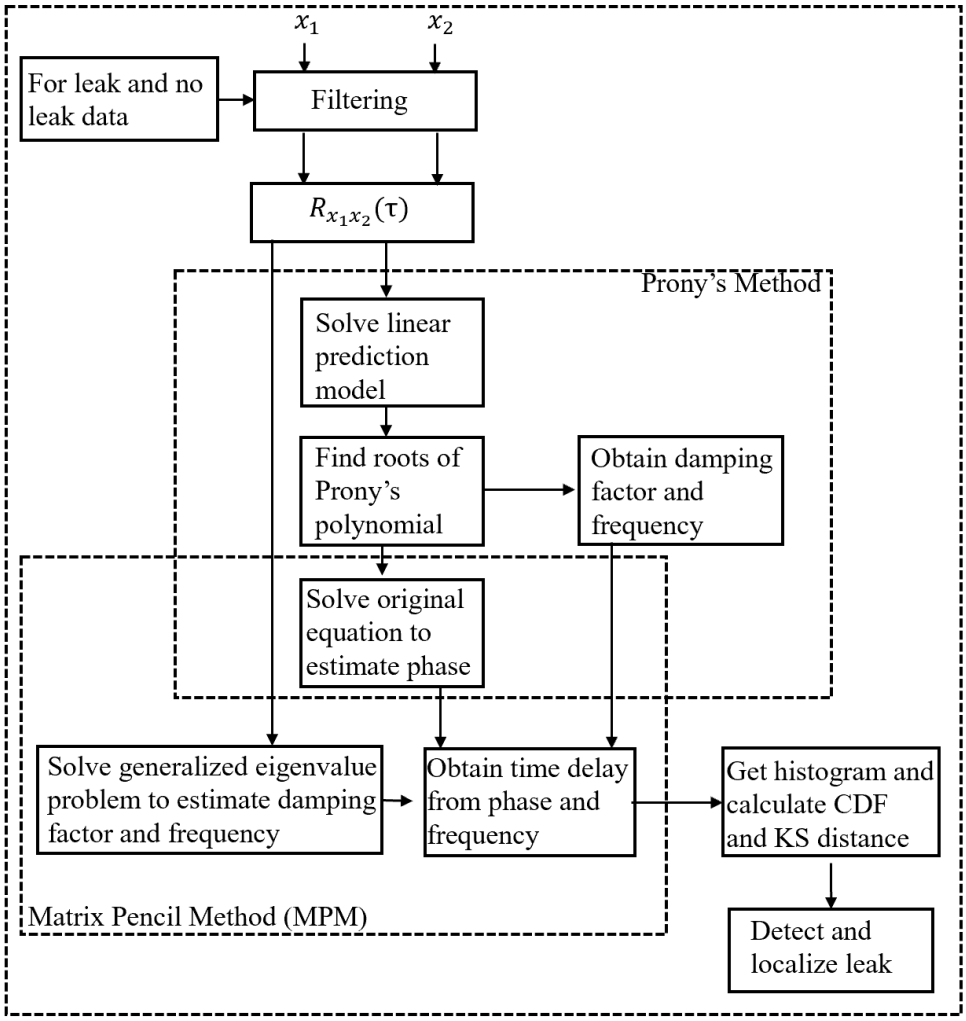

Figure 4.3: Prony's method for leak detection and localization

wave speed to determine the leak location. The detection and localization of a leak using Prony's method, as well as the application of CDF and KS statistics in a single pipe, are described in detail in the experimental results Section 5.4.2. If the pencil parameter L of the MPM is the same as the order P of the Prony's, the output of the method is identical. However, under noise, the results of the two methods may be different as the statistical variance of the MPM is always less than the Prony's [130]. For the active method, the SNR is high, and hence the MPM is used in WDNs for estimating time delays which are discussed in Section 6.3.4.

Prony's or the MPM, when applied to the cross-correlation of two signals, yields information regarding the presence of new impedance changes with respect to a baseline as well as its location, using the associated time delay(s). Due to the well-known issues regarding noise sensitivity, Prony's method works well on the cross-correlation, which requires two sensors in the proximity of the leak location. However, in many cases, especially when dealing with networks of pipes, the acoustic energy from a newly formed leak may manifest itself in only one location [91]. A new method based on time-frequency analysis that is robust to noise and can operate on measurements obtained from a single sensor is discussed next to address this case.

4.2.3 Time delay estimation based on time-frequency method

Short time Fourier transform (STFT)

The practical objective of using the time-frequency method is to extract the information from the data, which may be short in duration. Classical methods like Fourier transform cannot handle transient signal analysis. Therefore, a technique like time-frequency is suitable for analyzing and preserving high-frequency content carried by transient signals. The important application of this method is the detection and extraction of unknown signals in noise. The localization of time and frequency through time-frequency transform makes it possible for de-noising, signal detection and identification, and extraction of the feature in the time-frequency domain. The short-time Fourier transform (STFT), which generates the signal in a two-dimensional time-frequency plane, is defined as ([132]),

$$STFT(\tau, \omega) = \int_{-\infty}^{\infty} x(t) w(t-\tau) e^{-i\omega t} dt, \tag{4.33}$$

where $x(t)$ denotes the time waveform being analyzed, $g(\tau)$ is some window function, t is the analysis time instant, and ω is the angular frequency. However, the issue with the STFT is the length of the desired segment, where choosing a short analysis window may cause poor frequency resolution. On the contrary, a long analysis window may improve the frequency resolution but compromises the assumption of stationarity within the window.

For example, in the simple case where there is only one propagation path, the superposition of incident and reflected harmonic plane waves can be resolved in the time-frequency domain as a pair of energy clusters in the spectrogram (STFT map is referred to as the spectrogram) separated by a time difference of Δt. Fig. 4.4(a) shows the incident and reflected waves of 200 Hz sine wave (with additive Gaussian noise resulting in SNR of 17dB),

generated using Eq. 3.58 and the energy clusters of the incident and reflected waves separated by Δt are shown in Fig. 4.4b. The mean shift clustering (MSC) technique used to obtain the time difference due to the leak is based on the foundation of STFT, and the theoretical aspect of this methodology is shown next.

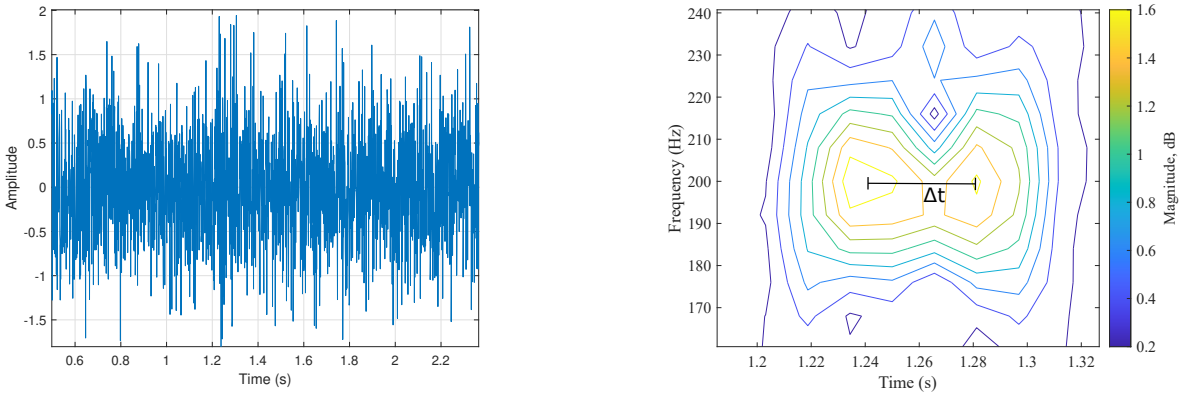

(a) (b)

Figure 4.4: (a) Numerically generated 200 Hz time signal; (b) pairs extracted using short time Fourier transform

Spectral mean shift clustering

The method presented for the case of a single sensor is a time-frequency technique that works on the principle of spectral decomposition using mean shift clustering (MSC), which is a non-parametric clustering technique based on the kernel density estimate (KDE) [133]. This time-frequency analysis technique works by blindly separating signal components in a signal containing multiple harmonics and transients polluted by an underlying noise process. Spectral MSC performs clustering with respect to the power spectral amplitude and allows for the extraction of buried, weak signal components or separation of signal components with similar amplitudes. Compared to traditional applications of MSC, such as image filtering and segmentation [134] the application of MSC for spectral decomposition is novel. However, it has been demonstrated to be a powerful pre-processing tool in the context of machinery diagnostics, where it was used for signal de-noising and extraction of key low-amplitude frequency components buried in a non-stationary signal [135]. As shown in this dissertation, spectral MSC provides a robust means of leak detection and localization using signals obtained from a single sensor as well.

The MSC spectral decomposition process takes place in two steps: the short-time Fourier transform (STFT) of the acoustic signal and MSC of the spectral energy, represented using the computed STFT power spectral amplitudes from the first step. When applied to the computed STFT spectrum, MSC acts as a pseudo-adaptive filter by grouping the components of the original spectrum into several sparser spectra, each containing signal components of similar amplitude. The non-parametric nature of spectral decomposition using MSC makes it a potent time-frequency analysis tool for non-stationary or transient-heavy signals—hydrophone signals utilized in this dissertation are non-stationary in nature, containing many time-varying signal components such as the transient waves emitted from the active source, wave reflections, network fluctuations, and other inherent noise processes—as well as for signals collected from systems with little to no a priori information available. Furthermore, MSC does not require knowledge regarding the shape or characteristics of the underlying data, allowing MSC to be applied to both arbitrary feature spaces as well as feature spaces that change with respect to time. Traditional time-frequency analysis techniques for these types of signals tend to be heavily parameter-dependent and computationally expensive, making them difficult to automate or implement within online frameworks. Contrary to these traditional approaches, MSC is computationally light and depends upon only a single parameter (the kernel bandwidth), which can be automatically determined [135], providing the added practical advantage of being conducive for both automated and online applications. The proposed pre-processing procedure consists of the following steps:

1. Windowing: The hydrophone signals of length L are first segmented into m equally sized, tightly overlapping windows (Hanning), followed by zero-padding prior to evaluating the STFT.

2. STFT and power spectral density: For a signal $x(t)$ and window function $w(\tau)$, the FFT algorithm is used to evaluate the Short-Time Fourier Transform (STFT) given by Eq. 4.33. From Eq. 4.33, the spectrogram representation of the power spectral density $|X(\tau, \omega)|^2$, which will be used for MSC, is obtained.

3. Kernel density estimate: For each window, the kernel density estimate (KDE) of the STFT power spectral amplitudes, denoted by X, is calculated. The KDE $p(X)$ using kernel $K(u)$ and bandwidth $h > 0$ is given by,

$$p(X) = \frac{1}{N} \sum_{n=1}^{N} K\left(\frac{X - X_n}{h}\right). \tag{4.34}$$

4. Mean shift clustering: Using the KDE p, the cluster centers, or modes of p can be obtained by applying the iterative mean shift transformation to each point in the KDE, given by $X_{\tau+1} = g(X_\tau)$, where $\tau = 0, 1, 2...$ denotes the iteration number. The corresponding gradient ascent function $g(f^+)$, is obtained by setting the gradient of p equal to zero, resulting in

$$g(X) = \frac{\sum_{n=1}^{N} X_n K' \left(\left\| \frac{X - X_n}{h} \right\|^2 \right)}{\sum_{n=1}^{N} K' \left(\left\| \frac{X - X_n}{h} \right\|^2 \right)} \tag{4.35}$$

   where $K' = dK/du$. At each iteration, each point in p is shifted towards and associated with a local mean until the magnitude of the "mean shift" vector $g(X) - X$ is less than the standard error. Once this convergence criteria is satisfied, the final locations at which all surrounding points have been shifted to are considered the modes of p. Each mode of p contains a subset of peaks of similar amplitude.

5. Separation of signal components: The resulting modes of the MSC decomposition are sorted in order of their size (i.e. number of points within the mode). As shown in [135], the largest cluster typically corresponds to the underlying noise as well as other low-energy components within the signal. In this application, isolation of this cluster results in a spectrum which contains only the low-amplitude, low-frequency components of interest.

6. Low-energy spectrogram: The lowest energy cluster from each STFT window are then combined to form a low-energy spectrogram.

Fig. 4.5 summarizes the steps of the pre-processing procedure.

Leak detection and localization is performed directly using the spectral information contained within the MSC low-energy spectrogram. The first step consists of extracting the time delays associated with pairs of peaks in the non-leak MSC low-energy spectrogram. This is achieved efficiently using a automatic pair finding algorithm which associates and extracts peaks of similar amplitude and frequency over a specified temporal window. Using these values, a baseline histogram associated with the non-leak case is created. When repeated across multiple runs, the mean and standard deviation of each histogram bin is used to set individual control limits for the bins. These control limits define a threshold in which an exceedance would indicate the presence of a leak located at that particular bin or time lag. Next, the pair finding and histogram building process is repeated for the leak data. The bin frequencies of the leak histograms are then be compared against the baseline

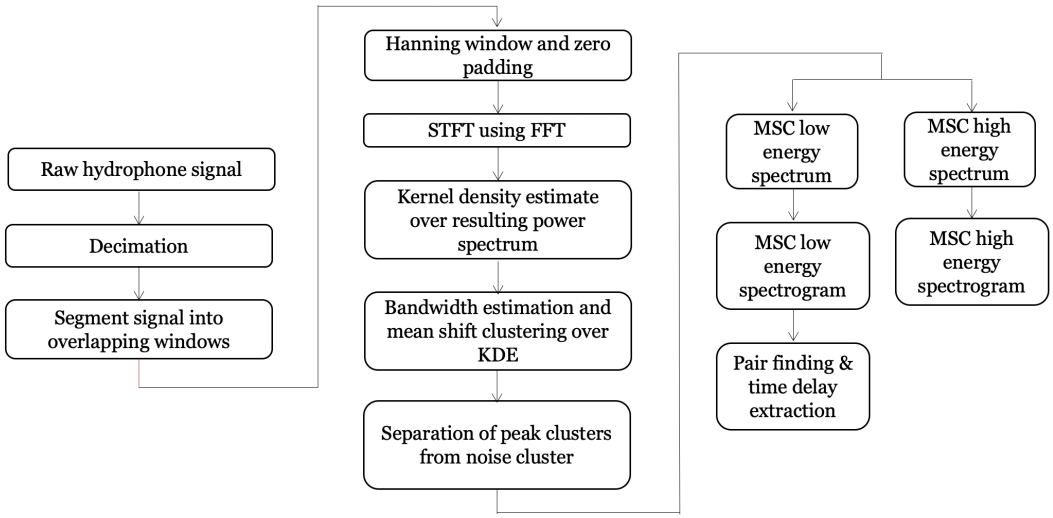

Figure 4.5: Flowchart for MSC pre-processing procedure

control limits. If the control limit is exceeded in a particular bin, a leak is suspected at that location. Finally, to incorporate localization uncertainty, the time lag in question is converted to an equivalent distance from the hydrophone, using the experimental wave speed. The detailed procedure is as follows:

1. Time delay extraction: for each non-leak hydrophone signal, the time lags associated with pairs of peaks in the MSC low-energy spectrogram is extracted. A peak pair is defined as a set of two peaks with similar amplitude and frequency, occurring within a set time frame which is determined based on known impedance discontinuities and the wave speed.

2. Non-leak baseline histogram: normalize the peak-pair time lag sets with respect to pair count, and aggregate MSC low-energy peak-pair information into histograms with bin size equal to the STFT time resolution.

3. Setting control limits for leak detection and localization: calculate the upper control limit for each histogram bin using the mean and standard deviation across all runs.

4. Leak histograms: Steps 1-2 are repeated for the leak hydrophone signals.

5. Detection: the bin frequencies of the leak histograms are compared against the non-leak control limits. A leak is detected when the upper control limit is exceeded at one or more of the histogram bins.

6. Localization: if a leak is detected in a bin, the time lag associated with that bin is converted into an equivalent distance from the hydrophone using the experimental wave speed.

This MSC detection and localization approached is summarized in Fig. 4.6 and the results attributed to this study are shown in Section 5.4.3.

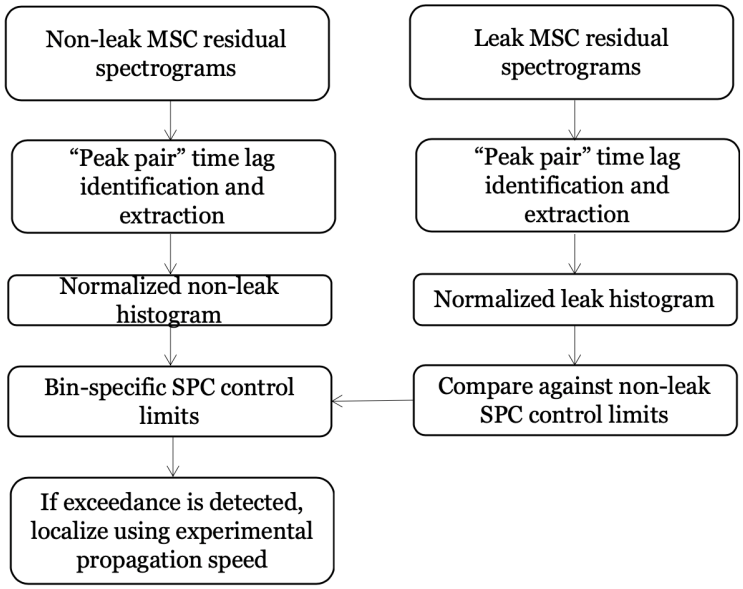

Figure 4.6: Flowchart for detection and localization procedure based on MSC low-energy spectrogram

4.2.4 Localization combining time delays with multilateration (MLAT) techniques

Multilateration (MLAT) is a technique mostly used in telecommunication and mobile networking today for determining the position of a source based on the times of arrival of signals between the source and the receiver. The receivers are located at known positions and carry a synchronized clock. This method assumes that the speed of the signal (radio or acoustic) wave from the source to the receivers is already known. Some of the popular MLAT techniques are the TOA and the TDOA [98, 99] which are also pursued in this dissertation.

The focus of this section and most of the content in chapter 6 is on the localization of leaks in complex WDNs, as most of the localization studies in the literature are limited to straight pipe sections or in very simple networks (say, a single junction). The experimental setup constructed for this study is shown in Fig. 6.1 and consists of multiple bends and terminations. The multiple acoustic paths possible for the acoustic waves render conventional methods not easy to employ for localization as they are based on line of sight (between the source and the receivers). This section establishes the theoretical framework and the procedure for MLAT application which extends to non-line-of-sight situations such as those addressed in this thesis.

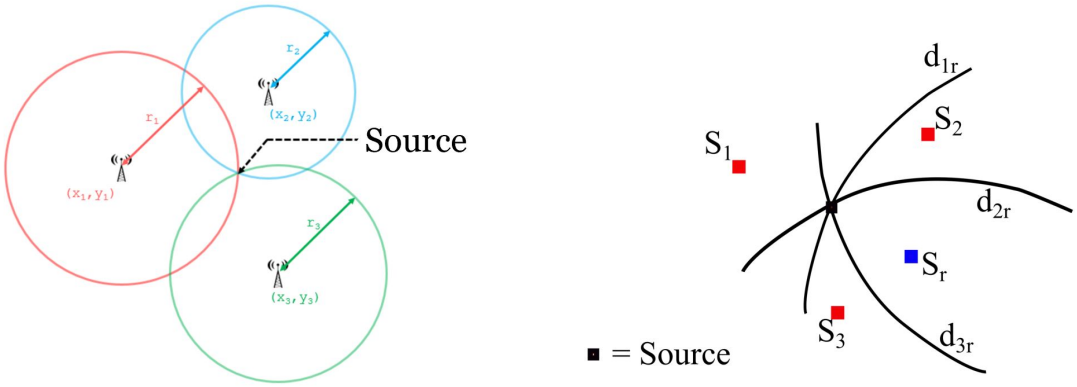

(a) (b)

Figure 4.7: The principle of (a) TOA method; (b) TDOA method for the 2-D case

Time of arrival

TOA is the absolute time difference between a signal emanating from the source and reaching the receiver. This time and the speed c yields the distance of a source from the receiver point [99]. Mathematically, this is given by:

$$d = c * (t_{arrival} - t_{sent}) = c * \Delta t, \tag{4.36}$$

where, Δt in Eq. 4.36 is the time difference between the time the signal is sent t_{sent} and the time the signal is received $t_{arrival}$. For the 2-dimensional case (source and receivers in the same plane), at least three sets of time differences are required to uniquely find the position of the source, while two sets can narrow down the position to two probable locations, and typically one of these two locations can be eliminated easily.

Time difference of arrival

TDOA is another popular technique used in the global positioning system (GPS). The TDOA algorithm locates the signal source using at least four non-reference receivers and one reference receiver to obtain different arrival times equations. Using D_r and D_m as a reference receiver distance and non-reference receivers distance respectively from the source position, the TDOA equation is given as ([98]),

$$\tau_{mr} = \frac{D_m - D_r}{c}, \tag{4.37}$$

$$d_{mr} = \tau_{mr} c = D_m - D_r, \tag{4.38}$$

where d_{mr} is the distance difference of arrival (DDOA).

$$D_m^2 - D_r^2 = |\boldsymbol{x}_m - \boldsymbol{x}_s|^2 - |\boldsymbol{x}_r - \boldsymbol{x}_s|^2 \tag{4.39}$$

Expanding Eq. 4.39 and grouping gives,

$$\begin{aligned} D_m^2 - D_r^2 = x_m^2 - x_r^2 - 2x_s(x_m - x_r) + y_m^2 - y_r^2 - 2y_s(y_m - y_s) \\ + z_m^2 - z_r^2 - 2z_s(z_m - z_s). \end{aligned} \tag{4.40}$$

The left term of Eq. 4.40 can be expressed in terms of just D_r and d_{mr} using Eq. 4.36. The equation then becomes,

$$\begin{aligned} d_{mr}^2 - 2D_r d_{mr} = x_m^2 - x_r^2 - 2x_s(x_m - x_r) + y_m^2 - y_r^2 - 2y_s(y_m - y_s) \\ + z_m^2 - z_r^2 - 2z_s(z_m - z_s). \end{aligned} \tag{4.41}$$

Grouping all known terms and defining it as w_{mr}, the above equation becomes,

$$d_{mr} D_r - (x_m - x_r)x_s - (y_m - y_r)y_s - (z_m - z_r)z_s = w_{mr}, \tag{4.42}$$

where $w_{mr} = 1/2(d_{mr}^2 - x_m^2 + x_r^2 - y_m^2 + y_r^2 - z_m^2 + z_r^2)$.

The location of the source x_s, y_s, z_s is solved as a function of the reference sensor x_r, y_r, z_r and non-reference sensor location x_m, y_m, z_m (m = 1..4) and the time delay of the sensors relative to the reference sensor τ_{m0}. The TDOA algorithm yields the position of the source x_s, y_s, z_s solving Eq. 4.42. Arranging above equation in matrix form gives,

$$\begin{bmatrix} x_r - x_1 & y_r - y_1 & z_r - z_1 & d_{1r} \\ x_r - x_2 & y_r - y_2 & z_r - z_2 & d_{2r} \\ x_r - x_3 & y_r - y_3 & z_r - z_3 & d_{3r} \\ x_r - x_4 & y_r - y_4 & z_r - z_4 & d_{4r} \end{bmatrix} \begin{bmatrix} x_s \\ y_s \\ z_s \\ D_r \end{bmatrix} = \begin{bmatrix} w_{1r} \\ w_{2r} \\ w_{3r} \\ w_{4r} \end{bmatrix}. \tag{4.43}$$

For the 2-dimensional case (where all the receivers and the source are in the same plane), there will not be any z term and at least three non-reference sensors are required to solve for the position of the source. The principle of the TDOA method is shown in Fig. 4.7b where S1-S3 are non-reference sensors, and Sr is a reference sensor, and the source is given by the intersection of three hyperbolas. As it is clear, one of the fundamental quantities required for the TOA and TDOA is the time delay τ_{mr} in Eq. 4.38 for TDOA and Δt in Eq. 4.36 for TOA, which are obtained through the MPM method described earlier in the thesis.

While TOA and TDOA methods work well when the source and receivers are within line of sight, in WDNs these methods result in significant errors due to NLOS conditions. The use of EKF to mitigate the NLOS errors and to accurately operate in complex indoor environments has been shown in other applications [136]. Garcia et al. [136] developed a framework that computes TDOA and uses it along with EKF for an indoor positioning system. The presence of furniture and different objects in an indoor environment cause obstructions to signal transmission and creates a NLOS scenario. The receiver works out its position using four emitting beacons, computing the TDOA, and using it with EKF to reduce NLOS errors. In this thesis, EKF is used with TDOA to localize a leak in the WDNs for both passive and active methods. The theoretical background of the EKF is presented in Appendix E and the results are shown in chapter 6 of this thesis.

4.3 Summary

In this chapter, the theoretical framework for signal decomposition based on two microphone techniques is established. Methodology for leak detection based on metrics such as reflected spectral density and transmission loss are presented. The procedure to extract time delays based on Prony's, MPM, and MSC methods is described. Lastly, the theory of multilateration for leak localization in complex WDNs is presented.

Chapter 5

Experimental Studies in a Single Pipe Segment

Experimental studies were conducted in a laboratory pipe test bed consisting of a single pipe segment closed at both ends to evaluate the methodology described in the previous chapter. Hydrophone data collected from tests conducted on a single straight pipe section using mono frequency and broadband signals were used to assess the performance of the proposed method. Passive and active methods were both studied to verify the theory of acoustic waves and to detect leaks located at various locations within the testbed. It is shown that low-frequency sound pressures with sufficient energy can be generated using the piezo device, and parameters such as the PSD, power transmission and reflection coefficients, reflected spectral density, and transmission loss can be used as an indicator to detect the presence of leaks.

For leak localization, two signal processing methods are studied; one requires two hydrophones as it operates on cross-correlation, while the other relies on just a single hydrophone. In the first method, Prony's method applied to the cross-correlation of two hydrophone signals is used to determine the in-situ wave speed and to locate (primarily localization, but also yields detection) the leak in the test section through the statistical treatment of the time delays. In the second method, a spectral mean shift clustering-based pre-processing approach is used in conjunction with a single hydrophone to localize (primarily localization, but also yields detection) the leak. The pre-processing approach aims to enhance the time-frequency representation of a hydrophone signal, while the time-delay information extracted from the enhanced time-frequency representation in conjunction with the estimated wave speed can robustly detect and localize leaks.

This chapter is organized as follows. Section 5.1 starts with a description of the experimental testbed where instruments used for carrying out experiments are described, and the test matrix is discussed. The results of leak detection based on the passive method is shown in Section 5.2. Detection and localization of leak using active method are shown in Section 5.3 and 5.4 respectively with the conclusion of the chapter described in Section 5.5.

5.1 Experimental Test-bed

In the following section, the laboratory test bed, instrumentation and test program used used for the experimental studies are described.

5.1.1 Test rig setup and layout

The laboratory testbed is located in the hydraulics lab at the University of Waterloo. Experimental results in this chapter are reported from a single length of a pressurized plastic pipe (schedule 80 grey PVC) 11.4 m long, with an internal diameter of 14.6 cm and a nominal wall thickness of 1 cm [137]. PVC pipe was selected here for experiments, as this is being commonly used in field applications and many passive leak detection methods do not work well in PVC pipes (due to high signal attenuation). The schematic of the experimental setup is shown in Fig. 5.1, where one end of the pipe is connected to a pressurized water inlet (55 psi of water pressure from the City of Waterloo's main distribution system), and an acoustic source was installed on the end cap located at the other end. A circular leak of diameter 6.5 mm, located at 6.4 m from the left flange, was simulated using a control knob, and when open, it translates to an average flow rate between 17 L/min-20 L/min, depending on the system pressure. There was no effort to control the system pressure as the objective was to simulate the actual hydraulic conditions to the extent possible in a laboratory setting.

5.1.2 Instrumentation and test program

The process of active acoustic leak detection involves introducing acoustic waves into a pipe network and measuring the acoustic response of the system. Analysis of the measured waves (acoustic response) reveals information pertaining to the state of the system. The instrumentation used to perform active acoustic leak detection is described next.

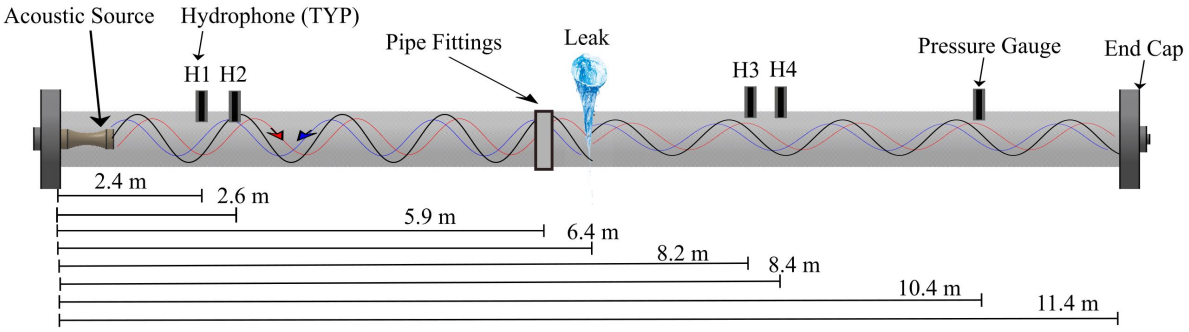

Figure 5.1: Schematic of experimental set-up used for mono-frequency and broadband tests; also shown is the acoustic source, the hydrophone receiver locations (for H1-H4) and the leak location.

The acoustic source used in the experiments is an acoustic projector. To date, this source has only been used by navy ships or submarines to track freely drifting floats, perform ocean mapping and acoustic communication [138]. However, its use for leak detection and localization is being reported for the first time. The source is oriented longitudinally within the pipe, and this is the desired orientation even in field settings. The initial construction and testing of this technology were performed by Anacostia Naval Research Laboratories in May of 1929 and was based on a design by Harvey C. Hayes [139]. More recently, acoustic projector technology has been used to develop advanced sonar techniques, underwater vehicle driving, and underwater imaging. [24].

The projector shown in Fig. 5.2a is a compact Class I barrel-stave flex-tensional, omnidirectional transducer primarily operated at low frequency fundamental flexural mode. As shown in Fig. 5.2b, the barrel stave consists of a piezo-ceramic stack which vibrates in the thickness mode in the longitudinal axis under electrical drive [140]. This then extends the end plate in the axial direction. The axial vibration excites the stave in a flexural mode. In the fundamental flexural mode i.e., at 1.6 kHz, all surfaces expand and contract in phase whereas in the higher frequency, i.e., 9.5 kHz, the end plate and stave are out of phase. This fundamental mode is below the plane wave cut-off frequency, which makes this device suitable for this application. However, the actual frequencies used in the ensuing experiments are much lower, and as seen later, the device can produce sufficient acoustic energy in the low region of the spectrum.

Voltage signal is generated by the Keysight: 33511B waveform generator and amplified through a power amplifier (APS 125 with maximum power of 450 VA@4Ω) and a step-up

(a) Acoustic source

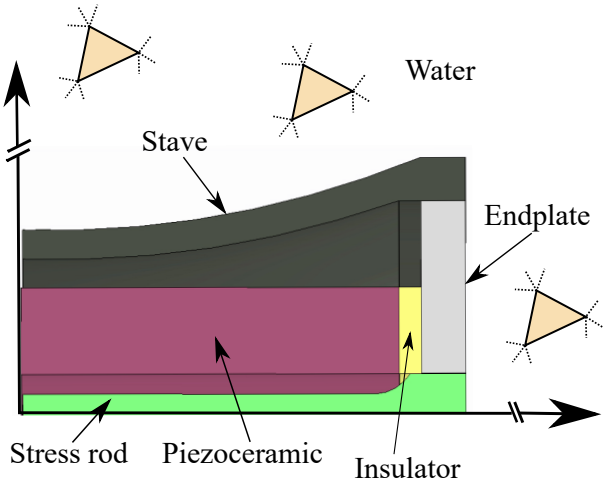

(b) Cross section of the source

Figure 5.2: Barrel-stave flex-tensional transducer schematic

transformer with turns ratio of 1:22.7 and primary rated voltage of 115 V RMS to inject energy much below the fundamental barrel-stave mode of the source.

(a) Keysight: 33511B Waveform Generator

(b) APS 125 Power Amplifier

Figure 5.3: Instruments used in the experimental studies

A total of four omnidirectional hydrophones (Teledyne RESON TC4013) labeled H1, H2, H3, and H4 in Fig. 5.1 are used for measurements. These hydrophones have a receiving sensitivity of -211 dB ±3dB re 1V/μPa and offer a usable frequency range of 1 Hz to 170 kHz (relatively flat response in these frequencies) and high sensitivity for their size. For the mono frequency tests, hydrophones H2 and H3 are used on either side straddling

the leak, while all four hydrophones are used for the test employing the two-microphone technique. The acoustic data from the hydrophones are collected using a 32 channel LMS SCADAS data acquisition system. All the measurements were taken at a sampling rate of 25.6 kHz, which was purposefully kept very high to take into account the second mode of the acoustic source near 9.5 kHz.

(a) Hydrophone TC4013 (b) LMS SCADAS for Data Acquisition

Figure 5.4: Instruments used for data acquisition

5.1.3 Test program

Several kinds of acoustic waves can be generated using the waveform generator shown in Fig. 5.3a. The first type includes pulses and sine waves of varying frequencies. The second type is continuous sines which create phase interference resulting in standing waves. The third type is the pseudo random binary sequence (PRBS) signals that are very robust to system noise, and other interference sources due to advantageous correlation properties [75]. The experiments carried in the experimental campaign comprises of two types of waves, and the test program are as follows:

1. continuous sine waves with different frequencies (mostly low frequency between 10 and 20 Hz, λ between 46.4 m and 23.2 m); and
2. broadband white noise between 1 - 100 Hz, λ between 464 m and 4.64 m.

Given that the second resonance frequency of the projector is 9.5 kHz, the sampling frequency is set to 25,600 Hz in all the experiments, which satisfies the Nyquist sampling theorem and prevents aliasing. However, the sampling frequency can be reduced considerably, given that the results showed most of the leak related information was contained

in the low frequency region. The test is conducted for 4 seconds in all the experiments as this duration was found to provide sufficient frequency resolution.

5.2 Passive Leak Detection Experiments

The first set of experiments consists of ambient measurements in order to capture the background noise characteristics in the pipe without any fluid. The test results show that the environmental noise present consists primarily of 60 Hz AC cycle noise (the rms of the signal is 0.68 Pa) and its harmonics and some sub-5Hz noise likely attributed to air pressure variations inside the pipe (see Fig. 5.5 and Fig. 5.6).

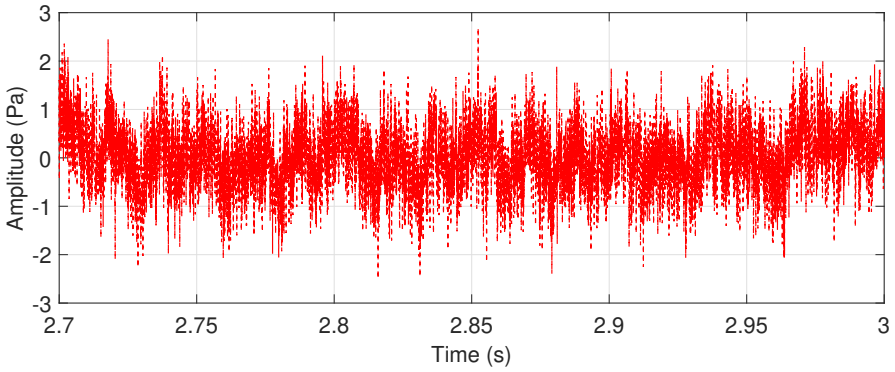

Figure 5.5: Time trace of background noise from hydrophone H2

Following the determination of noise-related frequencies, the second set of ambient tests are performed on a single pipe containing water pressurized to 55 psi. This case is called ambient as no external excitation is supplied to the pipe system. The waves produced in no-leak and leak conditions are recorded using hydrophones placed at the two ends as shown in Fig. 5.1. A high pass Butterworth filter is applied with a cutoff frequency of 5 Hz to remove the low-frequency harmonics present in the system. Time signatures obtained from both the hydrophones for the pipe containing a leak and no leak are shown in Fig. 5.7. The corresponding DFTs are shown in Fig. 5.8 and Fig. 5.9. Comparison of the two plots shows that the presence of a leak results in an increase in acoustic pressure amplitude in the signal in the low-frequency regions between 100 to 300 Hz and 500 to 800 Hz. The position of H2 and H3 from the leak are 3.8 m and 1.8 m, respectively. The DFT plot of H3 shows a significant difference between the leak and no leak spectra in all the entire frequency range. The difference in the spectral amplitude between H2 and H3 can be

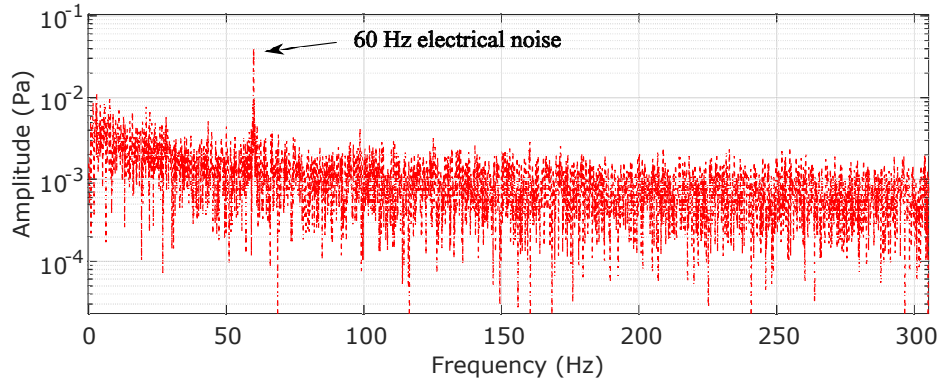

Figure 5.6: Single pipe: DFT of the background noise from hydrophone H2

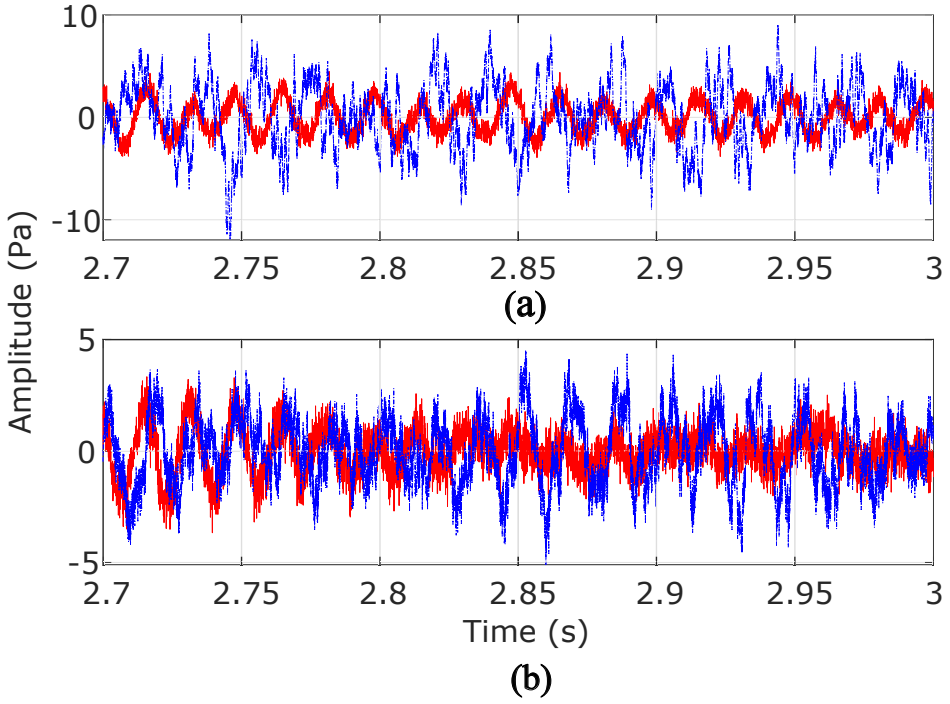

Figure 5.7: Time trace of ambient data from (a) H2; (b) H3; blue dotted line represents leak signal while red solid line represent no-leak signal

attributed to signal attenuation as H2 is more than twice the distance from the leak as H3.

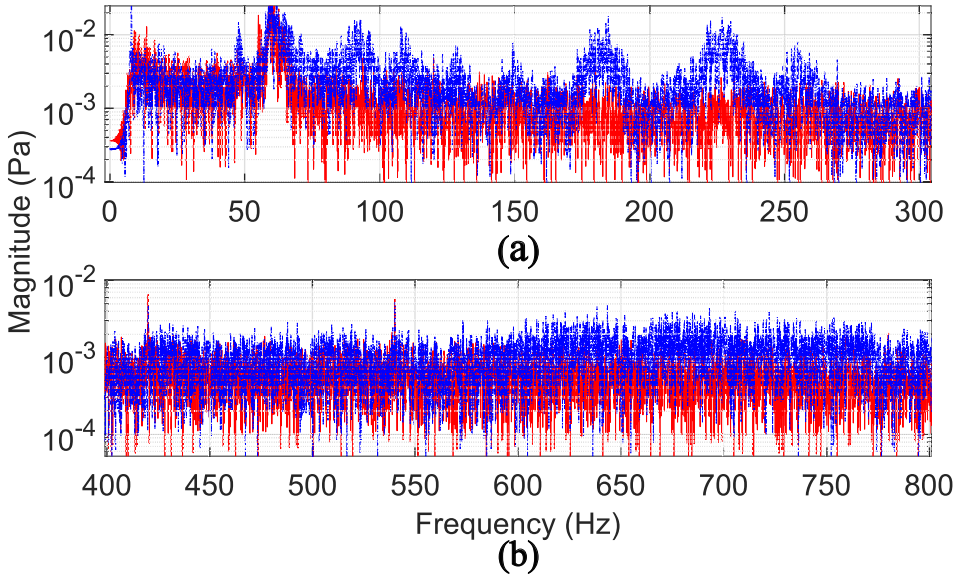

Figure 5.8: DFT of ambient data from H2 in the frequency range of (a) 0 - 300 Hz; (b) 400 - 800 Hz. Blue dotted line represents the signal with a leak present, while red solid line represent the case where there is no leak

5.3 Active Leak Detection Results

Initial tests were performed to evaluate the signal propagation through pipe walls as well as through the water column. A sine wave of mono frequency 1.6 kHz is used to excite the system, which corresponds to the resonant mode of the driver and within the theoretical frequency range (1-1863 Hz) for plane wave propagation with zero wave propagation angle, as shown in Fig. 3.6. Given these conditions, theoretically all of the acoustic signatures collected by the hydrophones are directly from the source and should not contain any reflections from the pipe wall.

Two sets of tests are conducted: one with water completely drained from the pipe and another with the pipe filled and pressurized to 55 psi. The time trace and the DFT of the response due to 1600 Hz sine wave ($\lambda = 0.29$ m) are shown in Fig. 5.10. Since the acoustic source is coupled with water, it is evident from the results that the wave propagating through the water has significantly higher energy (58 Pa RMS when pressurized compared to 3 Pa when empty) and is capable of propagating over long distances.

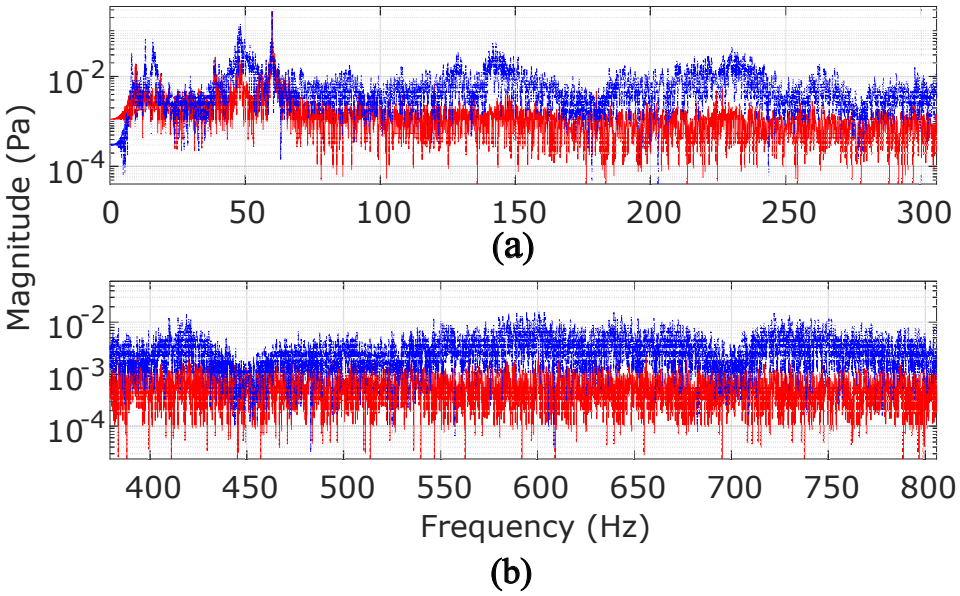

Figure 5.9: Single pipe: FFT of ambient data from H3 in the frequency range of (a) 0 - 300 Hz; (b) 400 - 800 Hz. Blue dotted line represents leak signal while red solid line represent no leak signal

5.3.1 Leak detection with mono-frequency excitation

For the test pipe section, plane-wave mode dominates below the frequency of approximately 1,860 Hz according to Eq. 3.23. However, the frequency range for which the incident wave gets reflected due to the leak is much lower than this cut-off frequency. The transmission and reflection coefficients shown in Fig. 5.11 (obtained using Eq. 3.88) show that for the leak diameter of 6.5 mm, 50% of the input energy reflects at $\approx$ 13 Hz. The side branch length is zero, which means the leak is flush with the pipe wall ($b = 0$ in Eq. 3.85). These results suggest that the range of frequencies for the tests where a leak of this size is discernible is roughly between 10-20 Hz.

To verify this, the pipe is excited with mono-frequency sine waves at various frequencies: 10, 12, 15, and 17 Hz. The test duration is 4 seconds, and a high-pass Butterworth filter is applied to the output measurements with a cut-off frequency of 5 Hz to remove low-frequency fluctuations prior to processing the data.

Theoretically, referring to Fig. 5.11, at 10 Hz ($\lambda = 46.4$ m), nearly 63 % of the energy should be reflected due to the leak, which is seen in the data for H2; time trace and the

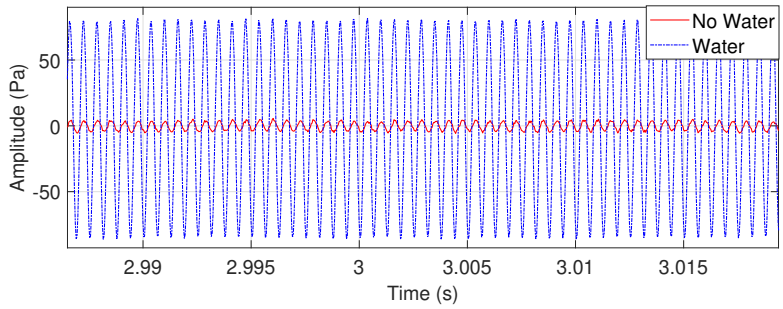

(a)

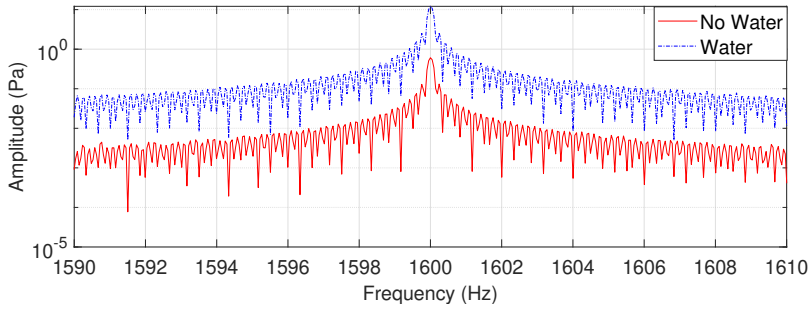

(b)

Figure 5.10: Comparison of signal propagation with and without water in the pipe at H1: (a) time trace of the 1,600 Hz sine wave; (b) DFT of the time trace

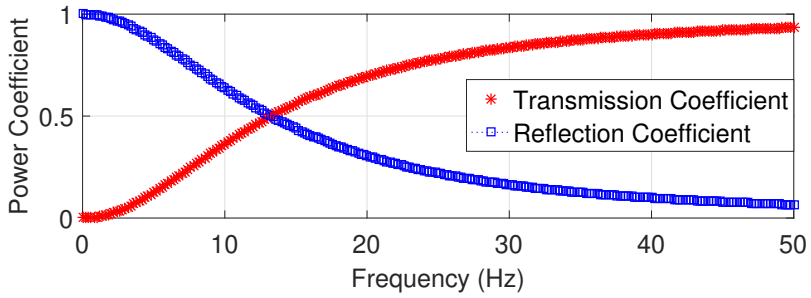

Figure 5.11: Comparison of transmission and reflection coefficient due to leak.

Fourier transform (FT) as shown in Fig. 5.12 (data from H1 shows a similar trend, but not shown for the sake of brevity). The results from H3 (Fig. 5.13) show that the overall acoustic energy is decreased in the presence of a leak when compared to the leak-free case

(theoretically, about 36% of the energy is lost due to a leak of this size). Additional tests are performed at 12, 15, and 17 Hz, (λ = 38.67 m, 30.93 m, 27.29 m respectively) and for each frequency, the test is repeated with and without the presence of a leak. The magnitude of acoustic energy at each driving frequency is obtained from the Fourier transform results at H2 for the leak and leak-free cases, and the results are shown in Fig. 5.14 in the form of frequency versus sound pressure amplitude. Results are consistent with the predictions, and the experimental results are compared with the analytical predictions and shown in Fig. 5.14. The analytically predicted magnitude of the acoustic level due to the leak is obtained by using the theoretical reflection coefficient in Eq. 3.88 together with the experimentally measured source energy when there is no leak. A third-order polynomial fit within the frequency range was used for interpolation as shown in Fig. 5.14 for illustration purposes.

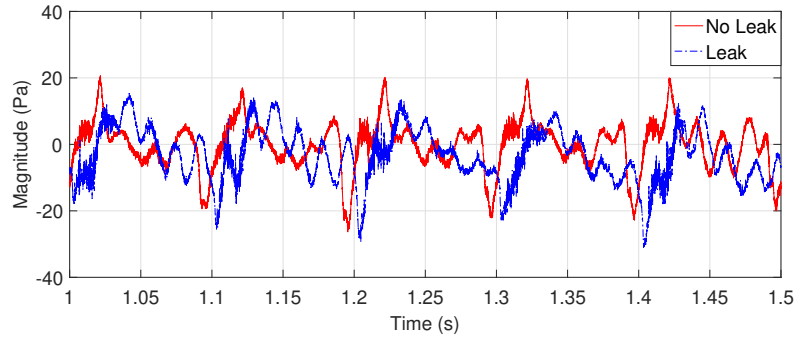

(a)

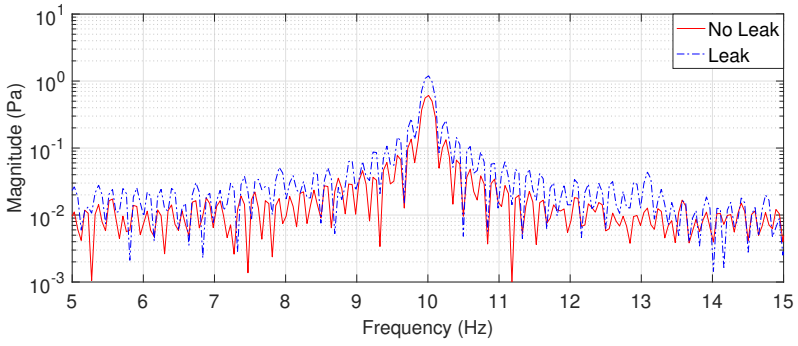

(b)

Figure 5.12: Comparison of leak and no leak responses recorded at H2 due to sine excitation from the source at 10 Hz: (a) time trace of the responses at H2; (b) FT of the response at H2.

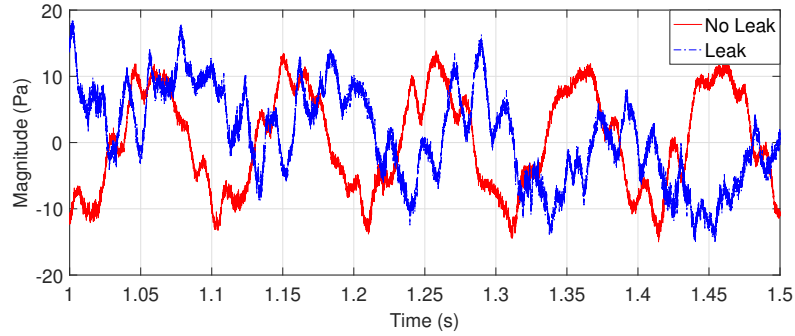

(a)

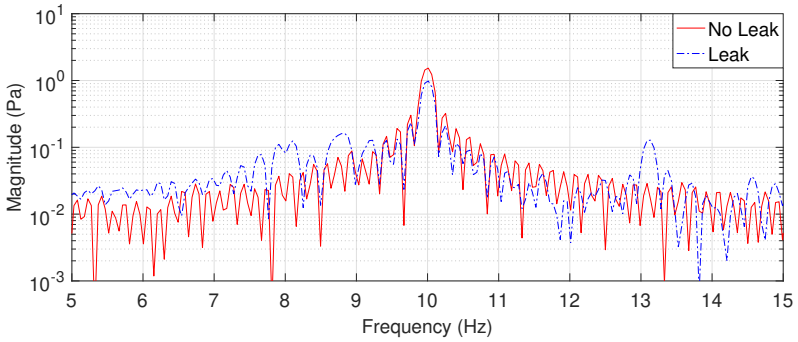

(b)

Figure 5.13: Comparison of leak and no leak responses recorded at H3 due to sine excitation from the source at 10 Hz: (a) time trace of the responses at H3; (b) FT of the response at H3.

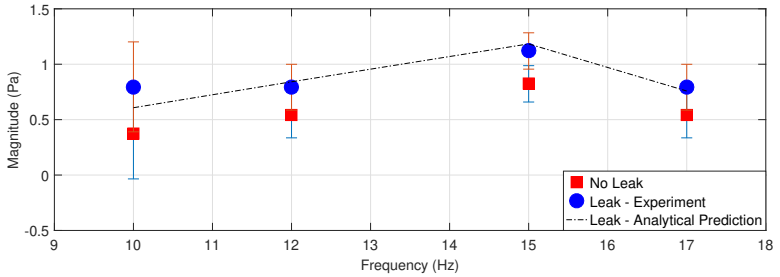

Figure 5.14: Error bar plot showing the leak and no leak magnitudes compared with analytically predicted values at H2

The magnitude of acoustic energy at each of these frequencies is obtained from the Fourier

transform results at both H2 and H3 in a single pipe. In the presence of a leak, it is found that the energy in H2 (sensor before leak) is always higher than H3 (downstream sensor) due to reflection [22]. This results in a ratio of magnitude being consistently higher at H2 and lower at H3 (actually greater than 1 at H2 and lower at H3). This trend is confirmed and present in Fig. 5.15. These results show that, when compared to the data corresponding to no leak, the energy at all the driving frequencies is enhanced at H2 and decreased at H3, which is consistent with the theoretical trends predicted. This shows that the filtering action due to the presence of the orifice is actually caused by the reflection of the wave to the source rather than the transmission of acoustic energy past the leak to the atmosphere.

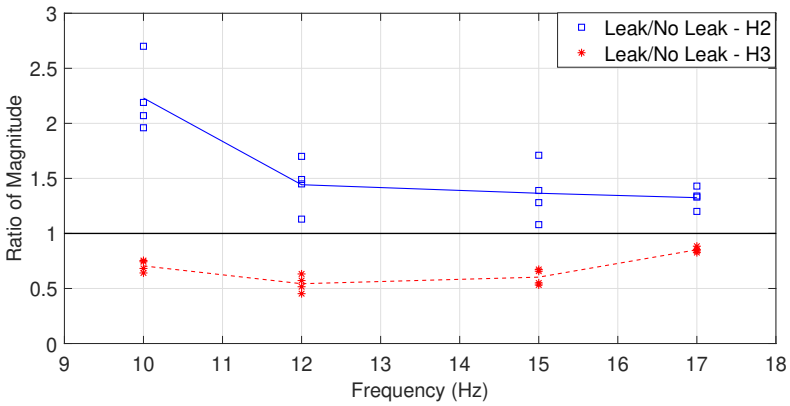

Figure 5.15: Leak detection in single pipe using ratio of FFT magnitude of mono frequency

Moreover, further testing is conducted at 40 Hz to determine the wave behavior at H2 and H3. The resulting plots shown in Figs. 5.16 and 5.17 confirm that there is little to no reflection, indicating that most of the wave is transmitted past the leak at that frequency. This also means that most of the leak energy is reflected well below 40 Hz, which is consistent with the theoretical prediction.

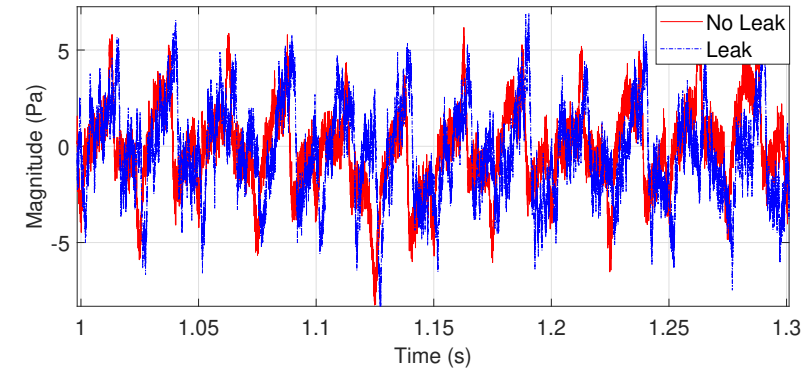

(a)

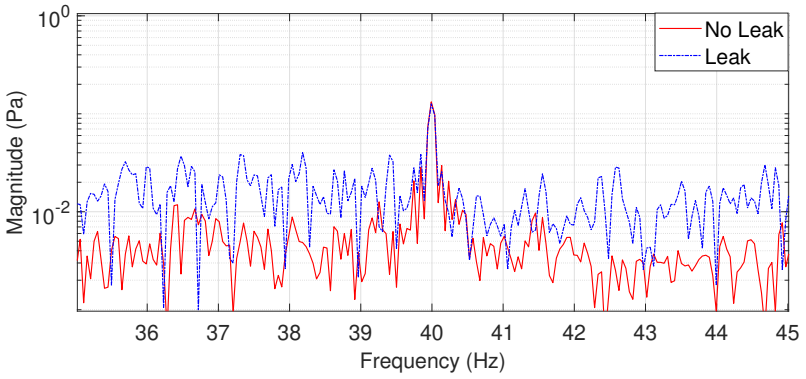

(b)

Figure 5.16: Comparison of leak and no leak responses recorded at H2 due to sine excitation from the source at 40 Hz: (a) time trace of the responses at H2; (b) FT of the response at H2.

5.3.2 Broad-band test results

Experiments are carried out using broadband excitation with frequencies between 1 to 100 Hz (λ = 464 to 4.64 m). The signal is also filtered with a 5th order high pass filter similar to the mono-frequency tests. The PSD of the signal sampled at H2 with a leak is compared with the baseline data in the same frequency range (between 10 Hz and 20 Hz). The overall higher magnitude observed in Fig. 5.18 due to leak is evidence that the detection is relatively easy with just with a simple measure such as PSD.

The piezo-ceramic driver is characterized by a high stiffness value. Using the known mass of

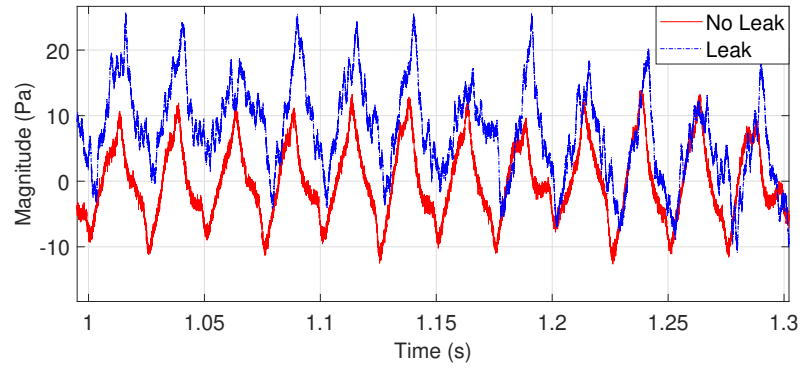

(a)

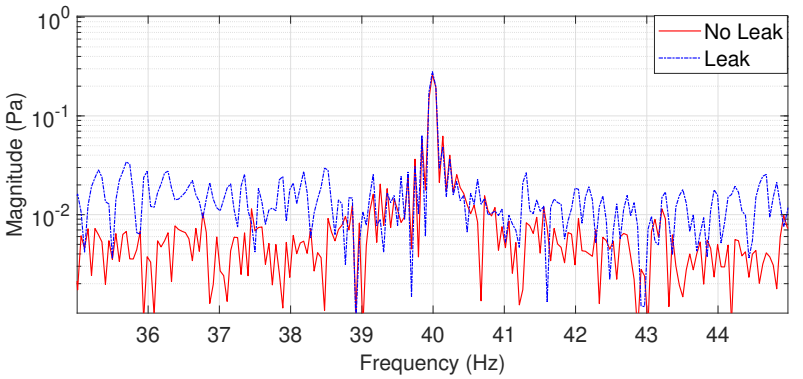

(b)

Figure 5.17: Comparison of leak and no leak responses recorded at H3 due to sine excitation from the source at 40 Hz: (a) time trace of the responses at H3; (b) FT of the response at H3.

the driver (1.3 kg) and the fundamental frequency, the stiffness is estimated as 132 $N/\mu m$ by solving Eq. 3.78. Plotting both sides of Eq. 3.78 against the frequency shows the resonant frequency as shown in Fig. 5.19a. The frequency where the two curves intersect is the combined mechanical resonance of the system and is approximately at 1600 Hz. At relatively low frequencies, i.e., below 50 Hz as shown in Fig. 5.19b, the two curves do not intersect (spectrally well separated) and are characterized by the pipe resonances ($\mathrm{Im}(\boldsymbol{Z_2}) = 0$), which is at 10 Hz and its odd multiples.

The experimental resistive and reactive impedances are estimated using the procedure described earlier in Section 4.1.3. A comparison of experimental and theoretical impedances

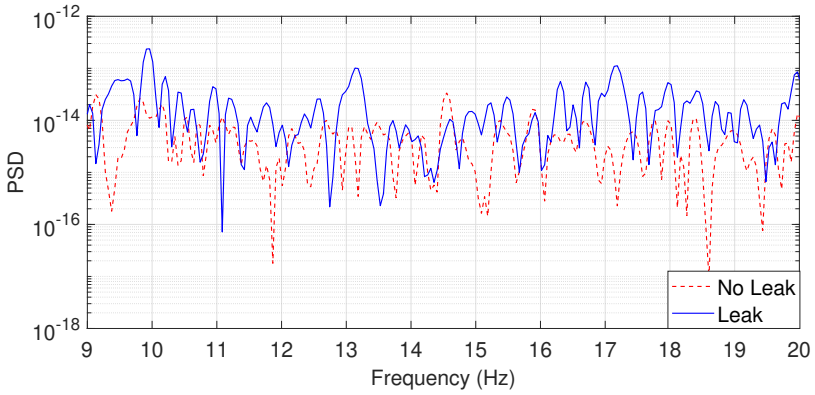

Figure 5.18: Leak detection in single pipe using power spectral density of white noise at H2

below 50 Hz is shown in Fig. 5.20, where the theoretical impedance of the pipe system is obtained by solving Eq. 3.74.

The experimental results obtained are in excellent agreement with theory except for frequencies below 4 Hz, primarily due to the application of the high-pass filter. At around 10 Hz and its odd multiples, the reactance is zero, denoting resonance. Conversely, anti-resonance is characterized by large impedance values at 20 Hz and its integer multiples. At other frequencies, the impedance is close to zero, and the system may show characteristics of resonance. The absorption coefficient, α in Eq. 3.74 is assumed to be small ($\alpha/k << 1$) so that the impedance magnitude is not singular and the magnitude of impedance reduces with increasing frequency.

In order to better visualize the effect of the leaks, the auto-spectral density of the reflected wave $\hat{S}_{RR}(f)$ is extracted from the leak and leak-free case impedances (Eq. 4.9). The comparison of the two plots as shown in Fig. 5.21 clearly shows the presence of a leak by enhancing the overall energy in the spectral region below 50 Hz. Furthermore, the resonant frequency around 10 Hz is also evident in the auto spectrum, as predicted. Five repetitions of the test were performed and the average of the area under the PSD of these five sets are calculated for each case, which results in 11.9 Pa^2 and 3.6 Pa^2 respectively for the leak and no-leak cases. The difference in the leak and no-leak spectral energy is clearly evident from these results.

Transmission loss can also be a good indicator for leak detection. The incident spectrum, $\hat{S}_{II}$, obtained by decomposing H1 and H2 and the transmitted spectrum, $\hat{S}_{TT}$, obtained from the downstream hydrophones H3 and H4 (by decomposition) can be used to calculate

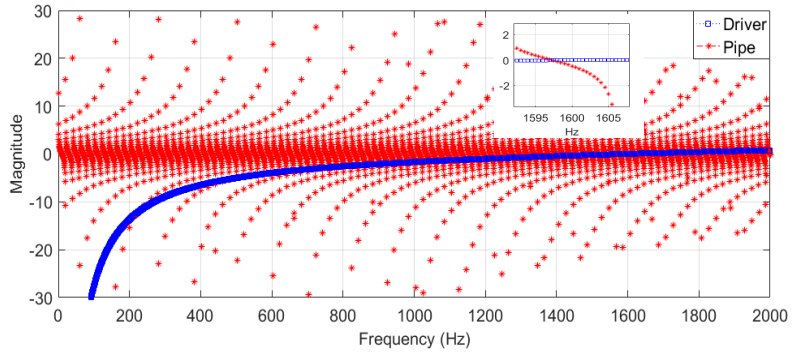

(a)

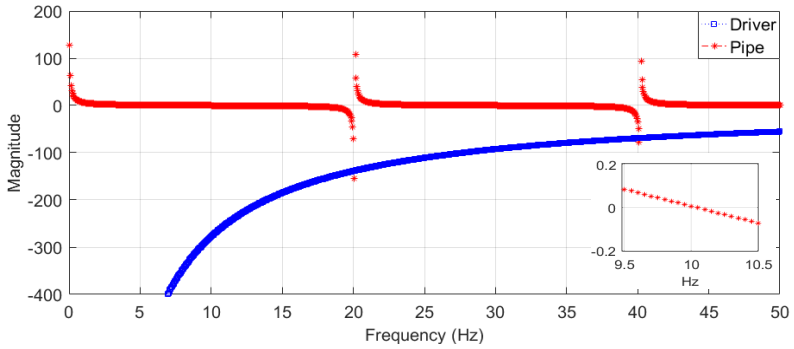

(b)

Figure 5.19: Pipe-driver resonance: (a) for frequency between 0 and 2000 Hz; and (b) for frequency between 0 and 50 Hz.

this quantity as defined in Eq. 4.14. However, the resultant raw data shown in Fig. 5.22 show heavy scattering. Therefore, a locally weighted smoothing (loess) [141] non-parametric procedure using a span of 10% is employed to smooth this data for the leak and leak-free cases. It is clear from the transmission loss trend shown in Fig. 5.22 that the presence of leak enhances the transmission loss at most frequencies, except at 20 Hz and at 40 Hz (and beyond), where anti-resonances occur. At other frequencies, the presence of a leak increases the transmission loss as sound energy is attenuated past the leak location. This also confirms that transmission loss can be used as an indicator to detect the presence of a leak in the pipe.

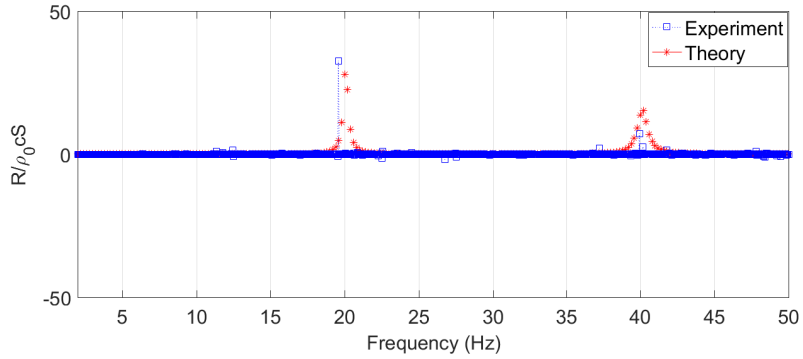

(a)

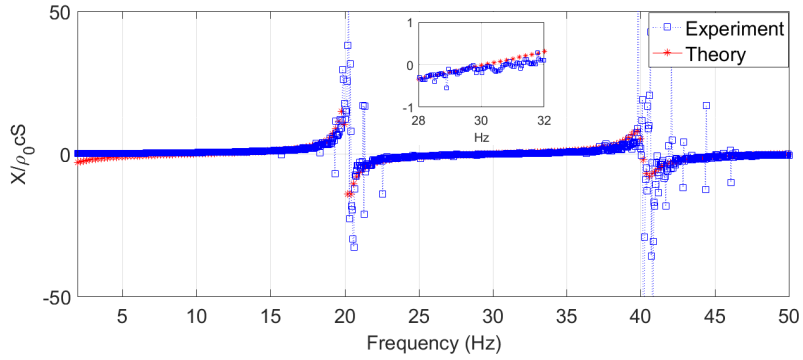

(b)

Figure 5.20: Comparison of estimated and theoretical results for: (a) the resistive part of the impedance; and (b) reactive part of the impedance.

5.4 Active Acoustic Leak Localization Results

This section discusses the experimental findings on localization conducted in a single pipe setup. The estimation of time delay using cross-correlation has been a go-to approach to localization for the study involving the passive method. However, this is not straightforward when working with the active method because of the dominant acoustic field; hence, the traditional method of extracting time delay is unsuitable. Fig. 5.24 shows the cross-correlation function when there is no leak in the system. As shown in the figure, the highest peak is not due to leak but from the direct transmission of the wave. Now, if there is a leak in the system, the cross-correlation function as shown in Fig. 5.25a will have additional peak and additional time delays, and obtaining the leak-induced time delay from

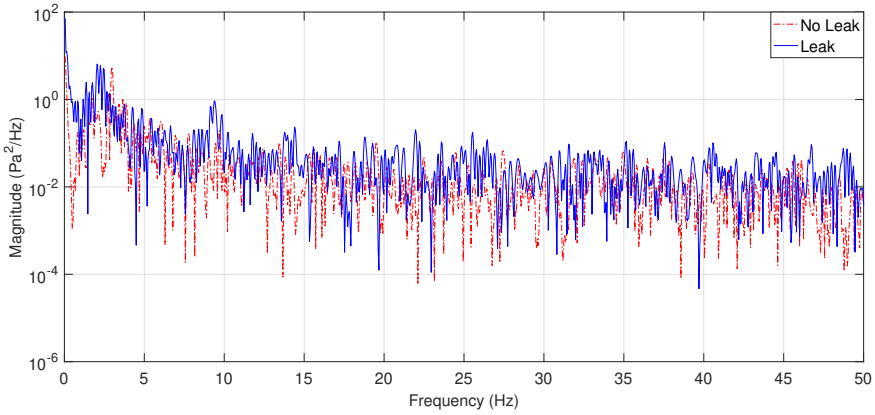

Figure 5.21: Comparison of reflected spectral waves with and without leak

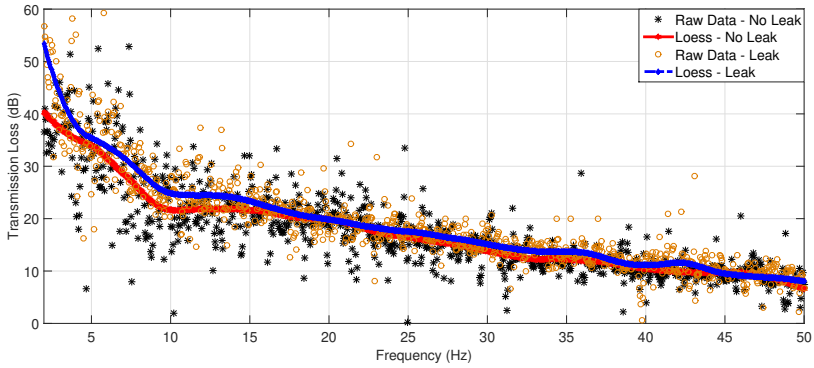

Figure 5.22: Transmission loss as a function of frequency

cross-correlation alone is difficult. For the disambiguation of leak-induced time delay from other time delays, methods like Prony's, MPM, and MSC are employed, and the results from these techniques are shown in this section.

5.4.1 Estimation of experimental wave speed

A comparison of the cross-correlation functions between the passive method and the active method for a straight pipe (schematic shown in Fig. 5.23) is shown in Fig. 5.24. The pipe is excited using white noise containing frequencies 1-100 Hz, and the cross correlation function is obtained after passing through a 5th order high-pass Butterworth filter with

cut-off frequencies set to 5 Hz. The maximum value of the correlation function is used to normalize the results.

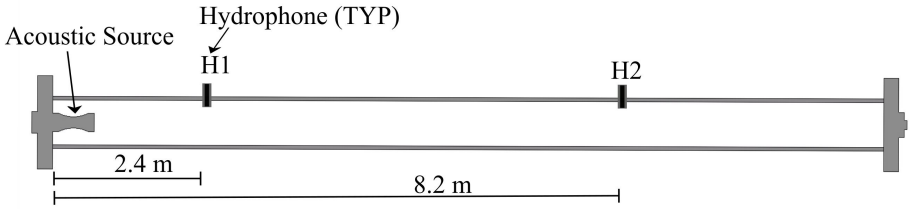

Figure 5.23: Schematic of a single pipe with two hydrophones H1 and H2.

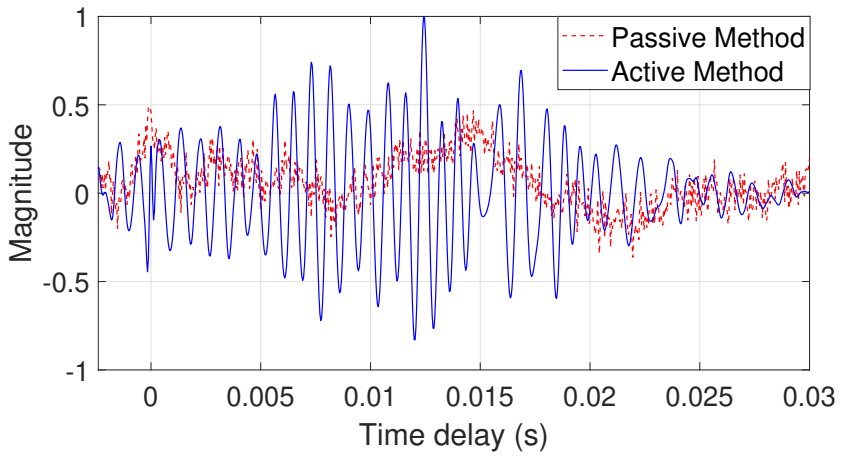

Figure 5.24: Comparison of active and passive cross-correlation functions obtained in this set up.

The comparison of the cross-correlation function between the active and passive methods is shown in Fig. 5.24. The cross-correlation of the passive approach shows the presence of several harmonic components, including the background pressure fluctuation, which may obfuscate results. However, for the active method, the most significant spike can be seen at 0.0124 s. This peak is attributed to the signal generated by the active source, which traveled a distance of 5.8 m between H1 to H2. The experimental wave speed can be estimated using these two pieces of information, which is crucial to estimate some of the parameters of the pipe system accurately (many equations in chapter 3 are the function of c). Moreover, it is also essential in the localization of leaks; the experimental speed of sound is determined to be 464 m/s, compared to the theoretical speed of sound of 458 m/s.

5.4.2 Prony's method

According to Eq. 3.88, 50% of the wave is reflected at a frequency of approximately 13 Hz for the leak diameter of 6.5 mm and reduces to zero at 50 Hz [22] (all of the acoustic energy is transmitted). For smaller diameters, (e.g., 3 mm, 50% wave reflection occurs at around 6 Hz) due to the physical size limitations of the transducer and the amplifier used, adequate driving energy cannot be achieved in the low end of the frequency range (less than 10 Hz). Hence, all the experiments were conducted at the smallest leak diameter of 6.5 mm, which was possible using this hardware. The acoustic source is excited using 1-100 Hz broadband white noise for 4 seconds, and Prony's method is applied to the resulting acoustic pressure measurements at H1 and H3. This experiment is repeated for $N = 50$ trials (25 trials for each leak and no leak case), with sufficient time between each trial to ensure that there is no residual acoustic energy left from the previous before starting a new one. The measured signals at H1 and H3 are passed through a fifth-order high pass Butterworth filter with a cut-off frequency set at 5 Hz. A typical normalized cross-correlation function of the sensor responses for the leak case is shown in Fig. 5.25a, which clearly exhibits the first peak at a time delay of 0.0125 s. Also evident in this cross-correlation function are several other peaks corresponding to various time delays, which may be of significance (e.g., end cap, sidewalls), but cannot be easily isolated in the cross-correlation function. Prony's method is applied to each signal in the test set to obtain the frequency and relative phase and all of the time delays (also termed as group delay) for each exponential. The group delay obtained from the analysis is shown in Fig. 5.25b. The model order $p = 14$ is obtained using the minimum subset error method [128].

While the time delays are primarily used for localization, they can readily provide a means to detect leaks as well. The histogram shown in Fig. 5.26 shows the time delays associated with known impedances in the pipe. The first peak around 0.0125 sec in the cross-correlation function in Fig. 5.25a corresponds to the direct transmission of the source signal from H1 to H3, which is also evident in the histograms (clearly in the no-leak case, less so in the leak case) at 0.0125 s. Using this time delay along with the known distance of 5.8 m between H1 and H3 yields the experimental speed of sound as 464 m/s as compared to theoretical speed of 458 m/s. The impedance discontinuity caused by the leak produces reflections of the incident signal back to H1, manifested by the time delay in the histogram bounded by [0.0179 0.0189] s and centered at 0.0184 s, which is a function of the bin size. This translates to the leak location range [4.15 4.384] m centered at 4.26 m from H1, based on the experiment determined speed of sound. The localization error in this case is less than 10%. Moreover, the values centered around 0.015 s corresponds to the pipe fittings located at 3.5 m from the location of H1. Similarly, the delays centered at 0.022 s and

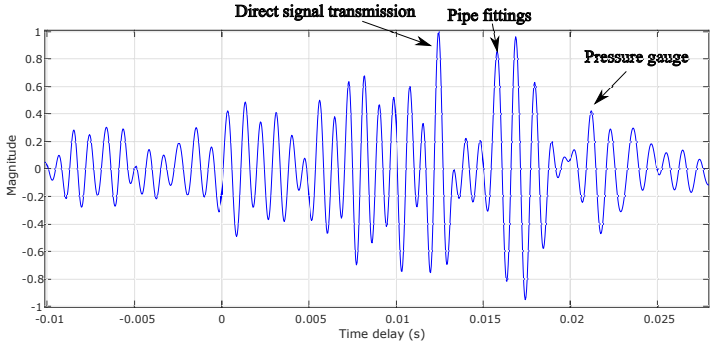

(a)

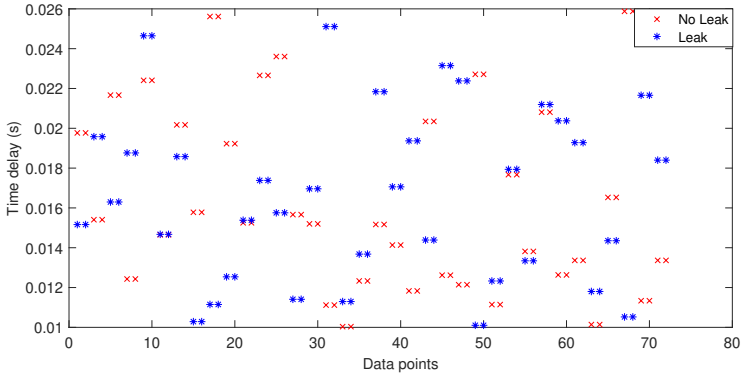

(b)

Figure 5.25: (a) A cross correlation function of an active signal; (b) group delays extracted using Prony's method

0.025 s are associated with the locations of pressure gauge and the end cap, respectively from H1.

The presence of the leak is also evident by comparing the empirical CDFs for the leak and no-leak cases, as shown in Fig. 5.27(a). Using the empirical CDFs, the location of the leak is represented by the region where the maximum deviation between the no-leak and leak CDFs occur. In Fig. 5.27(a), the impedance discontinuity caused by the leak is evident in the region [0.015 0.019]s. Fig. 5.27(b) shows the comparison of the empirical CDFs for the no-leak case, which does not exhibit similar divergence at the leak location. The Kolmogorov-Smirnov (KS) distance can be used to obtain a quantitative measure for the distance between two empirical CDFs (i.e., leak and no leak time delay data). Fig. 5.28 shows the KS distance between the leak and no-leak case in Fig. 5.27(a) and (b),

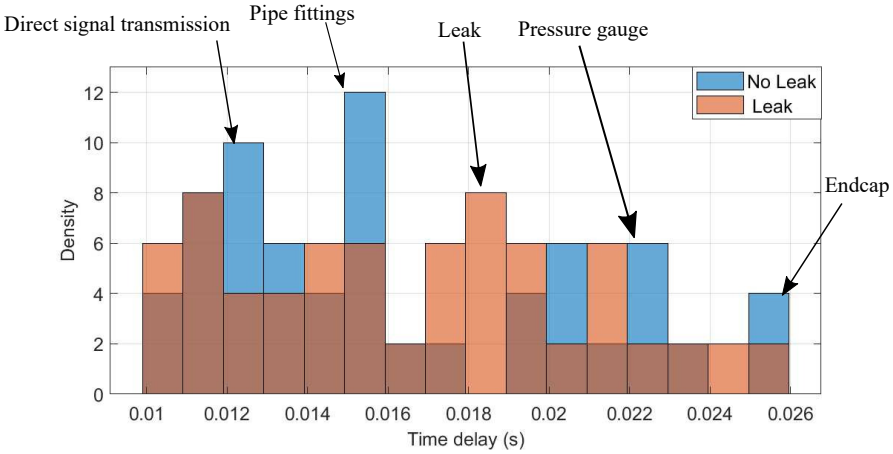

Figure 5.26: Comparison of time delay histogram between leak and no leak

computed at each time delay. The KS distance in Fig. 5.28 is maximum between t = [0.0158 0.0165]s, with the maximum value KS(max) = 0.1667. For comparison, for the no-leak case in Fig. 5.27(b) the KS distance is relatively small, KS = 0.079. Using the experimental wave speed (464 m/s), the leak is localized within the range [3.66 3.82]m, which means the leak is localized within 10% error of the actual leak location using the KS distance metric.

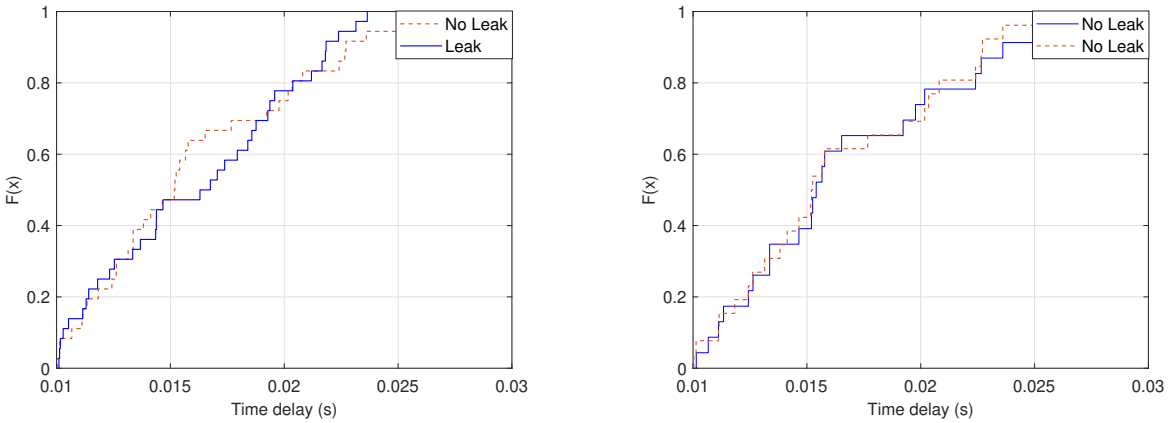

Figure 5.27: Comparison of empirical CDF between (a) a leak and no leak; (b) two leak-free time delay data

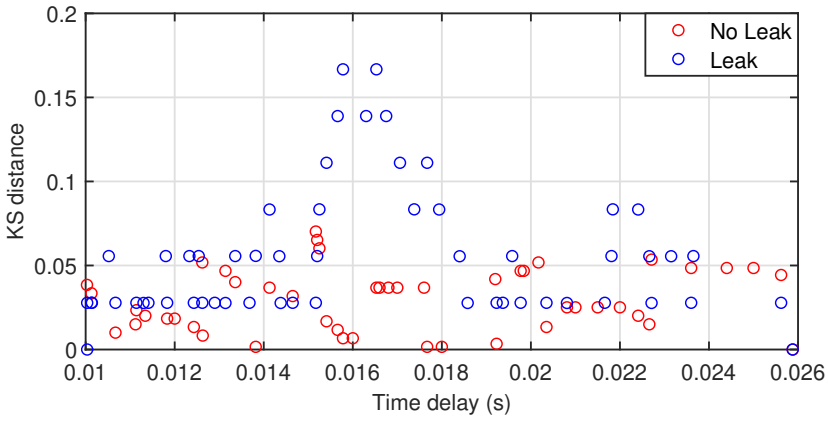

Figure 5.28: KS distance computed between leak and no leak at different time delay

For validation, the experimental data (same data was used with high pass filter, and the results are shown in Fig. 5.26) is again treated with a second-order bandpass Butterworth filter. The effective bandwidth and the lower and upper support frequencies of the bandpass filter are typically defined using coherence and the frequency range where the phase is linear with frequency [142], which is between 5-50 Hz. The coherence function and the unwrapped phase for the leak case are shown in Fig. 5.29. Prony's method is applied to each signal in the test set to obtain the frequency and relative phase and all of the time delays for each exponential. The group delay obtained from the analysis is shown in Fig. 5.30.

The histogram shown in Fig. 5.30(a) shows the time delays associated with known impedances in the pipe. Most reflections occur for the frequency range between 5 and 50 Hz because of impedance change due to leak. Therefore, the impedance discontinuity caused by the leak produces reflections of the incident signal back to H1, manifested by the time delay in the histogram bounded by [0.0167 0.0179] s and centered at 0.0174 s is a function of the bin size. This translates to the leak location range [3.89 4.16] m centered at 4.02 m from H1, based on the experiment determined speed of sound. The localization error, in this case, is less than 5%. The other time delay due to impedance change related to end cap or pipe fittings is not as clear as when a high pass filter is applied. The presence of the leak is also evident by comparing the empirical CDFs in this case as well, which is shown in Fig. 5.30(b). Using the empirical CDFs, the location of the leak is represented by the region where the maximum deviation between the no-leak and leak CDFs occurs. In the figure, the impedance discontinuity caused by the leak is evident in the region [0.015 0.019] s.

It is worth noting here that band-pass filtering (using the supports at 5Hz and 50 Hz) identified using coherence and unwrapped phase yield similar results for the leak location,

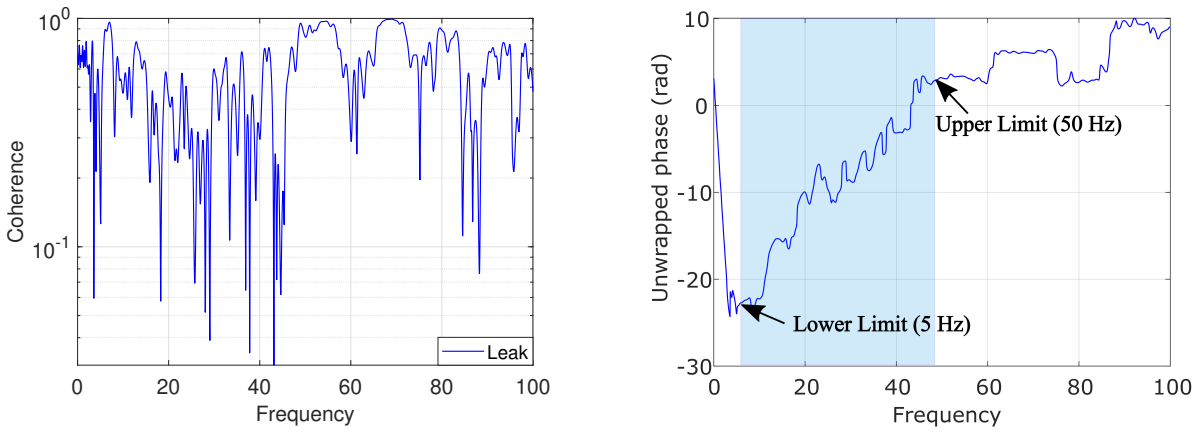

(a) (b)

Figure 5.29: (a) Coherence function ; (b) unwrapped phase of the leak signal

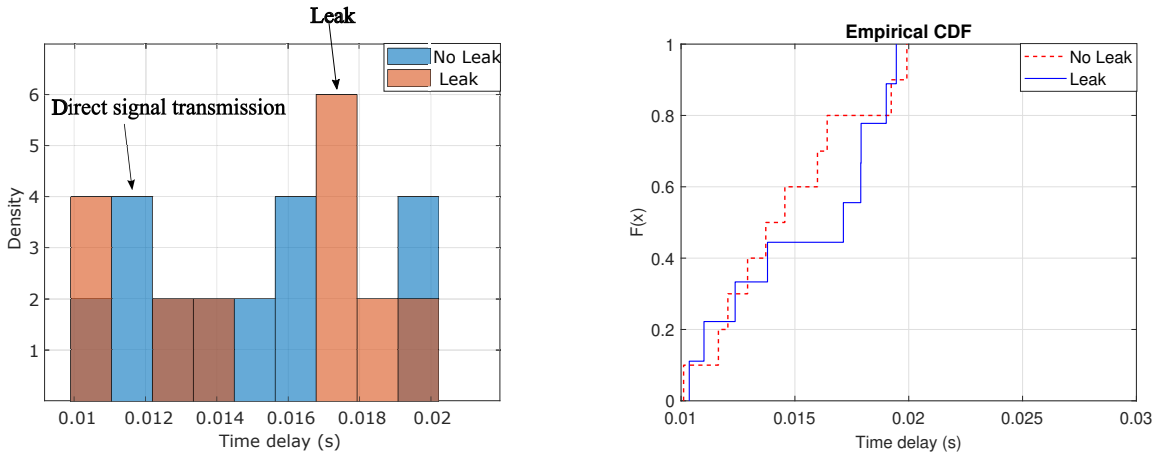

(a) (b)

Figure 5.30: Comparison of (a) time delay histogram ; (b) empirical CDF between two no leak data of a band-passed signal

however cannot reliably detect the presence of end cap as this information is contained in the transmitted frequencies beyond 50 Hz.

5.4.3 Mean shift clustering

Detection and localization

While the Prony's method described in the previous section utilizes two sensors for time delay estimation, this section shows that time delay estimates can be obtained using a single sensor. The MSC pre-processing approach, as summarized in Section 4.2.3 and Fig. 4.6 was applied to the case of a single channel of acoustic data. Fig. 5.31 illustrates a sample spectrogram obtained from the hydrophone data at H1, with no leak. Fig. 5.31a corresponds to the raw signal, while Fig. 5.31b and 5.31c are the spectrograms corresponding to the MSC high energy and low energy components, respectively. The spectrogram of the raw signal shows that the spectral content of the hydrophone signal is non-stationary as a result of the active source and typical network fluctuations. The raw spectrogram shows there are many small, low-energy regions that are masked by surrounding peaks and higher-energy regions, rendering them difficult to identify directly on the raw spectrogram. However, these low-energy regions are successfully decomposed and isolated in the low-energy spectrum shown in shown Fig. 5.31c.

Using the methodology described in Section 5.4.3, the time lags associated with the peak pairs found in the MSC low-energy spectrograms were extracted and aggregated into histogram representations. Fig. 5.32 illustrates a sample histogram using data from hydrophone H1, which contains the aggregated time lags from a leak and no-leak run. Labels corresponding to the theoretical location of known impedances are also identified on the histogram. Fig. 5.32 shows that at the leak location, the identified instances of delay pairs in the leak case are larger compared to that of the non-leak case. It is important to note here that for the case of no-leak, there should theoretically be no delay pairs associated with the leak location; however, since the same experimental set up was used both for the leak and no leak cases, the valve insert produces impedance discontinuity in both cases, which results in delay pairs in both the spectrograms. Additionally, the frequency of pairs at the endcap location, hydrophone H3 and the pressure gauge are also evident in both cases, however the density decreases for the leak case compared to the no leak case, due to the reduction in the acoustic energy associated with the reflections from these impedance discontinuities.

The detection and localization methodology described in Section 5.4.3 across several data sets can produce a normalized histogram with non-leak control limits, such as the one shown in Fig. 5.33. In Fig. 5.33, the normalized bin frequency of the leak case is shown to exceed the control limit at only one bin: 0.0175s. Using the experimental speed of sound (464 m/s) determined previously, this time lag is converted into an equivalent distance

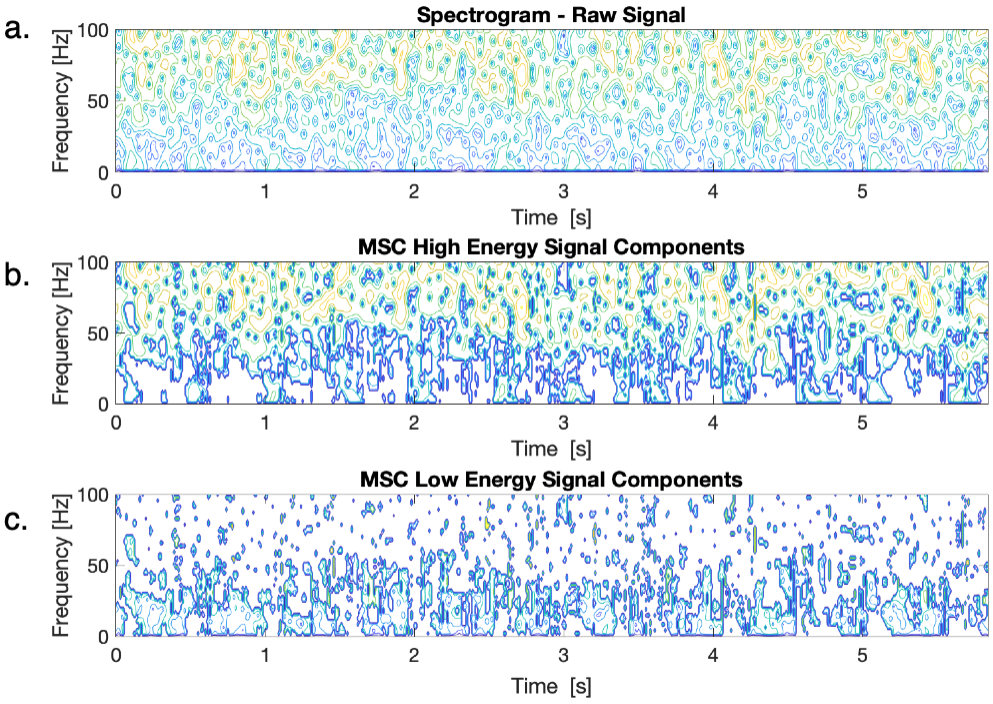

Figure 5.31: Sample spectrograms for no-leak single pipe hydrophone: (a) raw signal, (b) MSC high energy components, (c) MSC low energy components

from hydrophone H1, resulting in an estimated leak location bounded by [3.77 m, 4.35 m] and centered at 4.06 m from H1. Using the mean distance of 4.06 m produces an estimate within 2% error of the actual leak location. Considering the boundaries of this region produces estimates within 9% of the actual leak location, similar to the results obtained for the two sensor case.

The estimation error is a function of the choice of histogram bin size, as well as the quality of the time-frequency map used to extract the time delays. Theoretically, given a sufficiently large sample size and time-frequency information (peak pairs), the uncertainty of the estimate will reduce to a very small number as the bin size is reduced. However, it is clear from Fig. 5.31 that the time frequency pairs in practice are not of similar amplitude or sharply-defined. Oftentimes, in practical applications, the peak-finding criteria must be relaxed in order to obtain a sufficient amount of time delay pairs. For example, using a more relaxed temporal search window or relaxed constraint on the relative amplitude in a

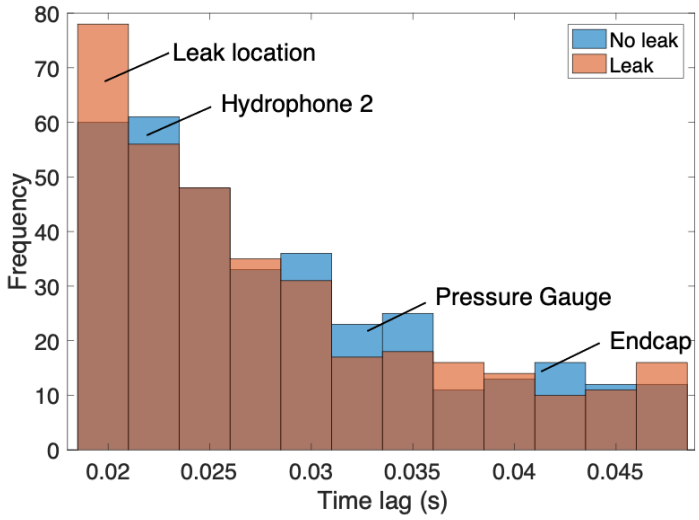

Figure 5.32: Aggregated histogram of pairs extracted from MSC low-energy spectrogram with known impedances labelled - Hydrophone H1 (n = 350)

pair of peaks will typically allow for the identification of more pairs at the cost of increasing the localization error.

Overall, these results demonstrate that the MSC pre-processing approach, coupled with a histogram and upper control limit can be used to efficiently and accurately detect and localize leaks using just a single channel of acoustic measurements. For detection, confidence in the detection result is a function the control limit used. In terms of localization, accuracy is dependent upon the time resolution chosen for the STFT in the pre-processing step, overall quality of the time-frequency information and choice of the bin parameter. For any given pipe system, the values of parameters can be determined iteratively based on data to maximize the confidence in the localization and detection result prior to full scale deployment. While the MSC approach can work with just one sensor, the methodology is more complex than Prony's and hence the latter is pursued for the network experiments.

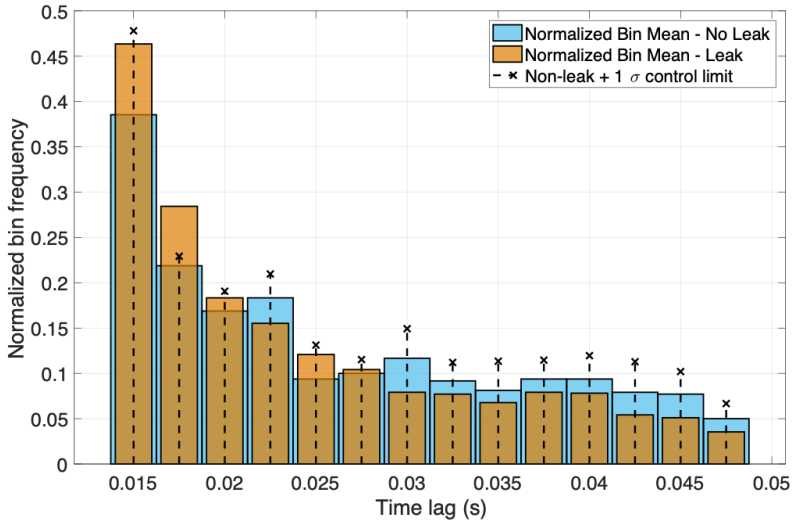

Figure 5.33: SPC control chart based on normalized leak vs. no leak histograms - 100 hz bandwidth excitation - Hydrophone H1

5.5 Summary

In this chapter, experimental results of detection and localization are reported from the single pipe segment laboratory setup. A comprehensive set of tests were conducted to assess the performance of the active acoustic method using low-frequency and broadband acoustic waves. Using low mono-frequency waves, the theoretical trend of power transmission and reflection coefficient coincide with the experimental data in the sense that the acoustic waves are reflected in the presence of a leak. From the broadband tests, the reflected wave power spectral density obtained from the two microphone techniques and the transmission loss are shown to be good indicators to suggest the presence of leaks in pressurized plastic water pipes.

Localization of leak in the single pipe is demonstrated using two methods, Prony's and MSC. The former utilizes two sensors to perform cross-correlation and extract time-delays, while the latter utilizes just one sensor at the cost of increased complexity. Using the experimentally determined wave speed, the dual sensor approach using Prony's method, and the spectral mean shift clustering that uses a single sensor were able to localize the simulated leak in the pipe within 10% error. Given the increased complexity of the MSC approach, cross-correlation based methods are pursued for the distribution system.

Chapter 6

Leak Detection and Localization in Water Distribution Networks

This chapter presents the experimental results for leak detection and localization in more complex laboratory-scale WDNs with tees and bends, and simulated leaks at several locations (even though leaks are simulated one at a time). As with the single pipe, experiments are carried out using both mono-frequency components and broadband excitation. Spectrum comparison and the theoretical power reflection coefficient trends used as surrogates for detection are shown in these experiments to work well. For localization, due to NLOS condition prevailing in the tests, the use of multilateration is explored. TOA and TDOA are two of the multilateration techniques used in this study, and EKF and ML methods are used to improve the localization error due to NLOS. This approach requires the estimation of at least three-time delays. The localization is pursued following two different approaches; first utilizes the passive method to data from three hydrophone pairs to obtain the time delays in the presence of a leak using the cross-correlation function. The time delays are then processed with multilateration augmented using EKF and ML methods. In the second approach, the active method is used to estimate the time delays from the matrix pencil method (MPM) [129] that disambiguates multiple acoustic paths in a system of pipes. The MPM applied to the cross-correlation of the signals is used to delineate time delays caused by impedance changes at junctions and leak(s). Finally, the time delays obtained are used together with multilateration as well as EKF and ML methods to predict the location of the leak.

This chapter is organized into four sections. The experimental details are presented in Section 6.1 and the frequency bandwidth selection process for passive testing is shown in Section 6.2. The results of leak detection and localization for both the passive and the

active method are described in Sections 6.2.2 and 6.3, respectively with the conclusions in Section 6.4.

6.1 Experimental Details

As with the single pipe, the experimental test bed for the network is also located in the hydraulics lab at the University of Waterloo. The pipes are made from schedule 80 grey PVC, with a diameter of 145 mm and a nominal wall thickness of 10 mm, which resembles the size and material used in many modern WDNs [137]. The setup shown in Fig 6.1 is a pipe network consisting of several junctions, outfitted with a pressurized water inlet, outlet valve, and leaks at several locations along the pipes.

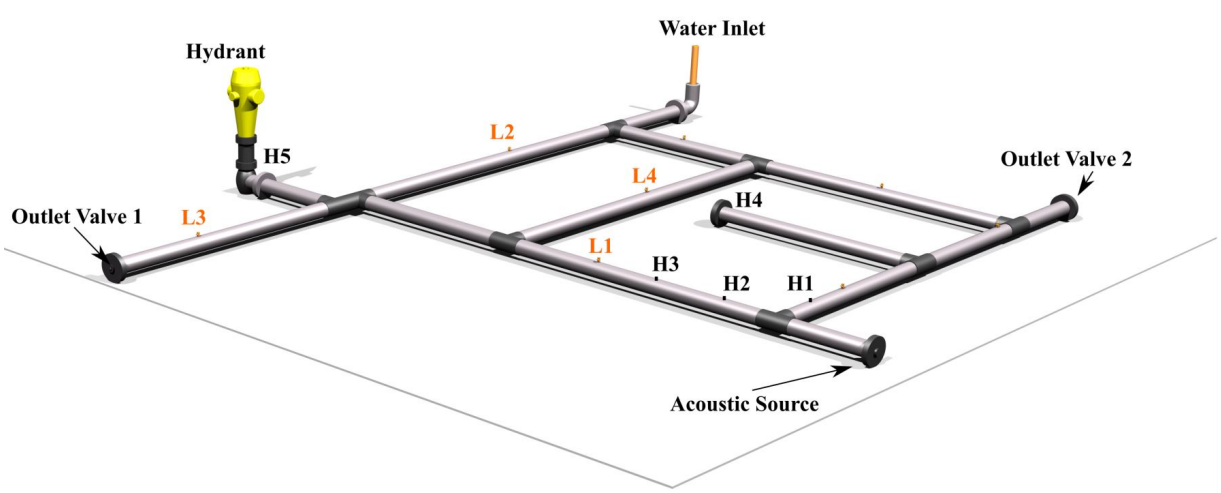

Figure 6.1: Schematic of the WDNs testbed used in the experiments

The pipe network configuration contains four valve-controlled 4 mm diameter leaks (pinhole) open to the atmosphere to simulate leaks (presented by L1-L4 in Fig 6.1) and a full-size hydrant located at one end. Sensors are inserted directly into the water column using this hydrant, along with other locations in the network. The pipe network is connected to the City of Waterloo's water distribution system, with a nominal pressure of around 55 psi while allowing the water pressure of the pipe network to be manually controlled via an inlet valve, regulator, and pressure gauge. In addition, there are several outlet valves positioned throughout the pipe network to simulate large leaks and drainage.

The dimensions of the WDNs are shown in Appendix B. The pipe network is instrumented with five hydrophones; hydrophone H5 is placed inside the hydrant, while hydrophone H1 - H4 are retrofitted in the pipe section as shown in Fig. 6.1.

The acoustic source used in the experiments is the same compact Class I barrel-stave flextensional omnidirectional transducer with a fundamental frequency at 1.6 kHz. The source is retrofitted to the flange of the pipe and attached at one end of the pipe as shown in the setup in Fig. 6.1. The detailed information of the source is given in Section 5.1.2 of this dissertation. As described previously, the source is excited using a signal generated by a waveform generator (Keysight: 33511B), amplified through a power amplifier (APS 125 with a maximum power of 450 VA@4Ω) and a step-up transformer (turns ratio of 1:22.7). This dynamic amplification allows for lower fundamental mode energy to be generated in the pipe system. Teledyne RESON TC4013 hydrophone receivers, represented by H1-H5 (H5 located in the hydrant), are connected to a 32 channel LMS SCADAS data acquisition system for acquiring acoustic data.

6.2 Passive Detection and Localization

6.2.1 Bandwidth selection

In order to perform cross correlations in the passive method, it is important to identify the regions in the frequency spectrum—using coherence and unwrapped phase—where time delays are to be estimated. The coherence function due to the leak at L4 and measured at H2 and H3 is shown in Fig. 6.2, after passing it through a 5th order butter-worth high pass filter with a cutoff frequency of 5 Hz. Muggleton et al. [143] showed that, if the coherence [144] is greater than 0.001 then the phase can be successfully unwrapped. Examination of data by Almeida et al. [142] showed that for plastic pipes, the phase can be unwrapped consistently if the coherence is greater than 0.01. This value of coherence is thus used to define the bandwidth called total bandwidth in which to analyse the sensor data to determine the time delay. However, in Fig. 6.2, the coherence value is higher than threshold value throughout the frequency region.

Although the coherence is used to define the frequency range over which the analysis can be performed, it has to be refined further when resonances are present in the system. This is because coherence does not take into account the resonance effects (peak in the modulus of the CSD and additional phase shift in the phase spectra) within its limits, thereby affecting the time delay estimate. The frequency in the cross-spectral density (CSD) over

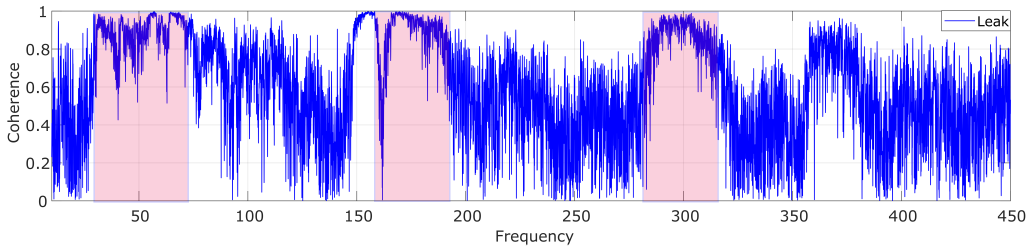

Figure 6.2: Comparison of coherence function between H2 and H3 for the leak case

which the un-wrapped phase is linear with frequency is defined as the effective bandwidth (EB). In the CSD shown in Fig. 6.3, the frequency between 160 Hz and 190 Hz or 280 and 314 Hz is selected as an effective bandwidth. Previous studies have shown that most of the leak signatures are present only in the low-frequency region, say below 500 Hz [77, 67] and the leak signatures in this study were found to be consistent with these previous findings (around 150 to 300 Hz).

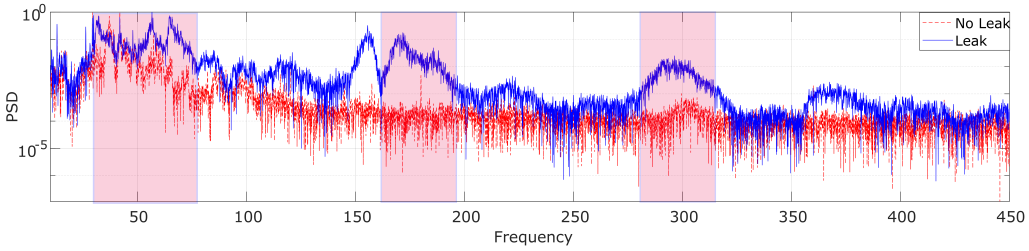

Figure 6.3: Comparison of cross power spectral density for the leak and no leak cases

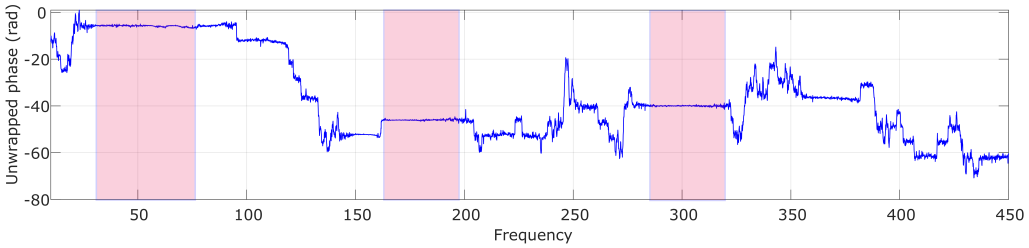

Figure 6.4: Unwrapped phase obtained from the coherence function of H2 and H3

Phase data in the effective bandwidth provides the time delay estimate between two hydrophone signals, which avoids the need for peak-picking in the correlation signal. If

the signal is stationary and non-dispersive, e.g. leak signals in plastic pipes, then the unwrapped phase has a linear behaviour, whose slope gives the time delay between two sensors. The gradient of the unwrapped phase in the shaded area in Fig. 6.4 gives the time delay of the leak which is also equivalent to the time delay estimated from the peak in the cross-correlation function of the same hydrophone pair, ie. H2 and H3.

6.2.2 Detection and localization in the passive case

The leak detection is conducted with the passive method to verify whether the leak signature is manifest in the same frequency region (as in the single pipe case) when the pipe length or leak distance is increased, or when more junctions are added, as shown in Fig. 6.1. The Fourier transform of the time traces obtained from the three hydrophones in ambient conditions with and without leak L3 are shown in Fig. 6.5. In the figure, the frequencies associated with the leak signature are clearly visible throughout the frequency range of 150 to 300 Hz at hydrophone H5, which is the closest to L3. For hydrophones located further away from the leak location, the leak signature attenuates significantly. For instance, the leak signature at H4 shown in Fig. 6.5(a) has diminished leak information above 250 Hz and below 170 Hz.

For localization using a passive method, the most common approach is to estimate the time delay using the cross-correlation method. Depending on the objective of the study, the signals have to be filtered prior to correlation to improve the performance. This filtering process filters the signal at frequencies where the SNR is the highest. For, e.g., if the objective is to obtain the time delays due to the leak, it is best to band-pass the signal in the frequency region where the leak is present. The filtering effect on the cross-correlation function is shown in Fig. 6.7. Based on the coherence plot and the CSD plot for the hydrophone pair H2-H3 shown in Fig. 6.2 and 6.3, respectively, the leak information is dominant in the three regions marked by the pink area. The difference in the cross-correlation function when the signals are filtered with the high pass filter versus the band-pass filter using the effective bandwidth is shown in Fig. 6.6. The difference between the leak and no leak cases is clearly visible in Fig. 6.6 (b) when the band-pass filter is applied.

For three hydrophone pairs: H1-H2, H2-H3, and H2-H5, the cross-correlation function due to L4 is shown in Fig. 6.7. For the scenario where the leak does not lie between hydrophone pairs, H1-H2 and H2-H3, the second peak in the cross-correlation function denoted by the circle in the figure give the time delay induced due to the leak. The first peak, in this case, represents the distance between two hydrophones. *(Side note - the speed*

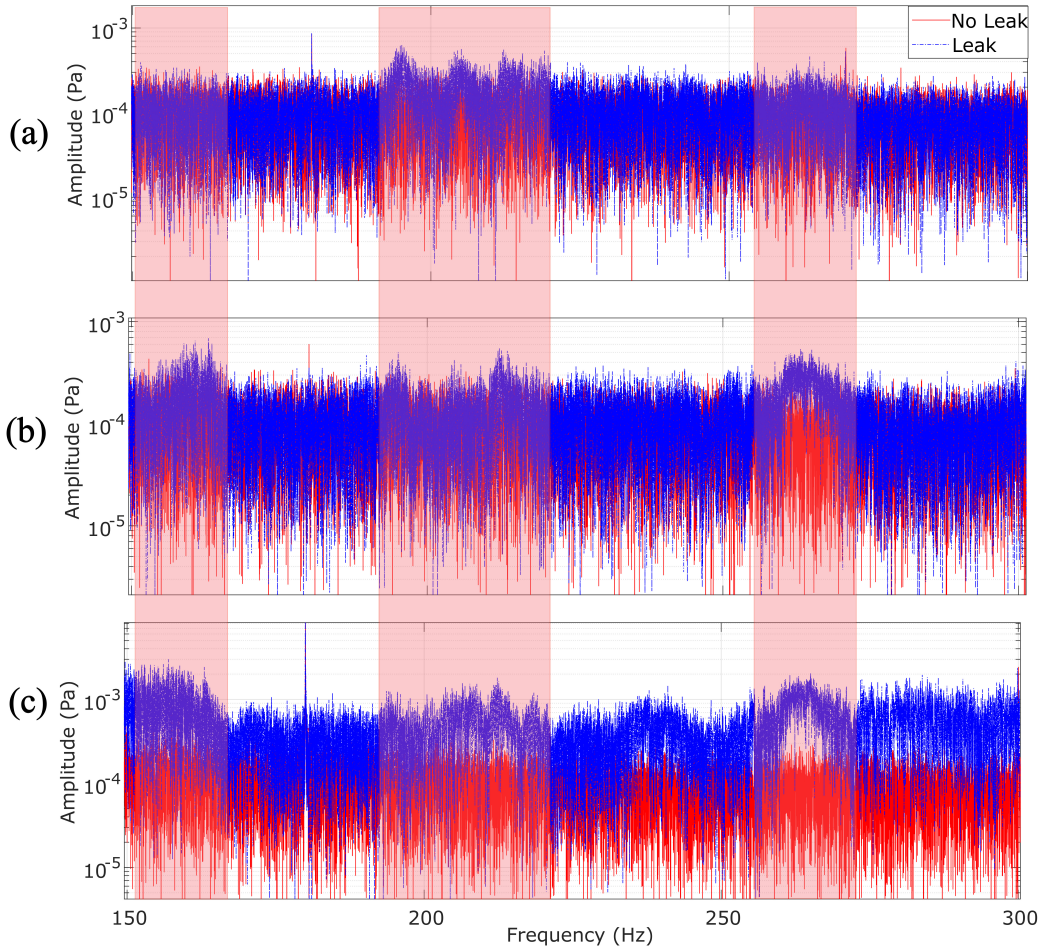

Figure 6.5: FT plot showing attenuation of L3 leak signature with data collection at; (a) H4 (13.56 m from L3); (b) H2 (6.76 m from L3); (c) H5 (2.86 m from L3)

of sound can be estimated using the time delay representative of this peak and the distance between two hydrophones, or if theoretical speed is used, the distance between hydrophone can be obtained for cross-reference.) For the hydrophone pair between H2-H5, the leak is technically between two hydrophones, and the highest peak in the cross-correlation as shown in Fig. 6.7(c) represent the leak time delay. The three-time delays corresponding to H1-H2, H2-H3, and H2-H5 are 0.0087, 0.0078, and 0.011 s. The same time delay value of 0.0078 s is also obtained from the gradient of the unwrapped phase in the frequency range of 160 and 190 Hz, which is used here for validation purposes.

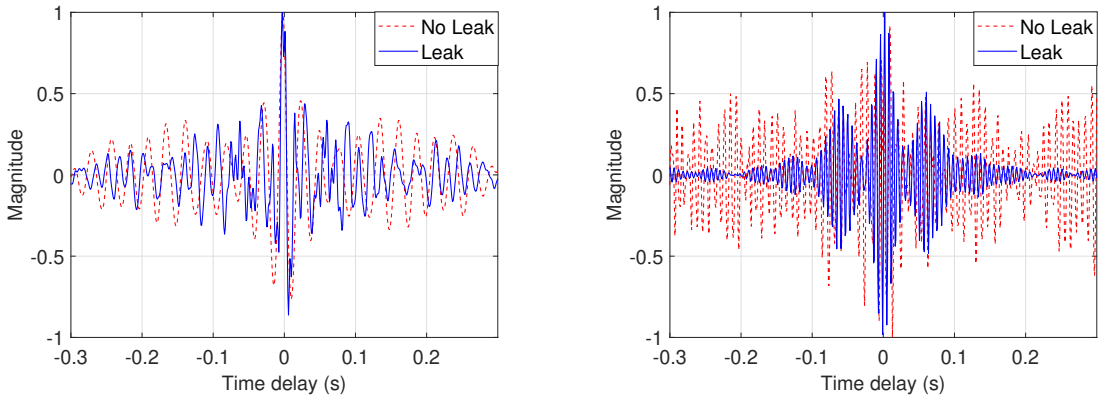

Figure 6.6: Comparison of cross-correlation function (H2-H3 pair) due to L4 when the signals are (a) high-passed at 5 Hz; (b) band-passed in the effective bandwidth of 160 and 190 Hz

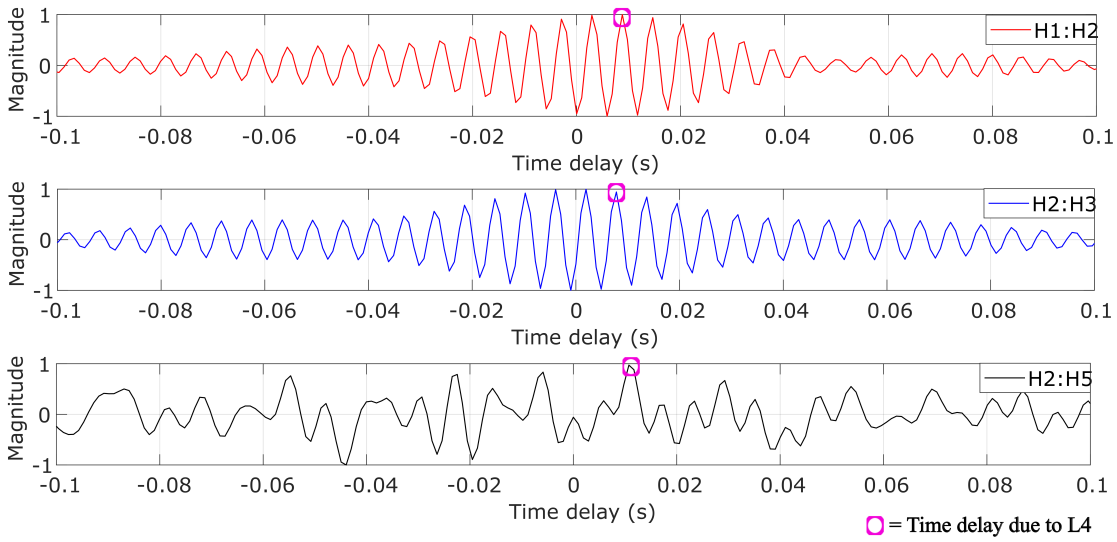

Figure 6.7: Cross-correlation function for different hydrophone pairs due to L4

After the time delays are computed for the three hydrophone pairs, the TOA method can be applied to estimate the location of L4 using Eq. 4.36. The speed of sound c in PVC

pipe setup is experimentally determined to be 464 m/s. The estimation of c is critical in the approximation of leak location as relatively small deviations could result in significant localization error. As pointed out by Almeida et al. [77], a 10% error in the estimate of c could translate to as large as 5% error in the leak localization. The intersection of the three circles as shown in Fig. 6.8a provides the estimated location of the leak. Comparison of the estimated and the actual locations shows accurate localization in the x-coordinate, but error in the y-coordinate. Similarly, for L3, the same three hydrophone pairs are used to obtain the time delays, and the TOA method is applied to locate the leak position. The comparison of actual versus estimated location is shown in Fig. 6.8b. The TDOA method using the same time delays yield similar accuracy in the location of L4, while worse for L3 localization.

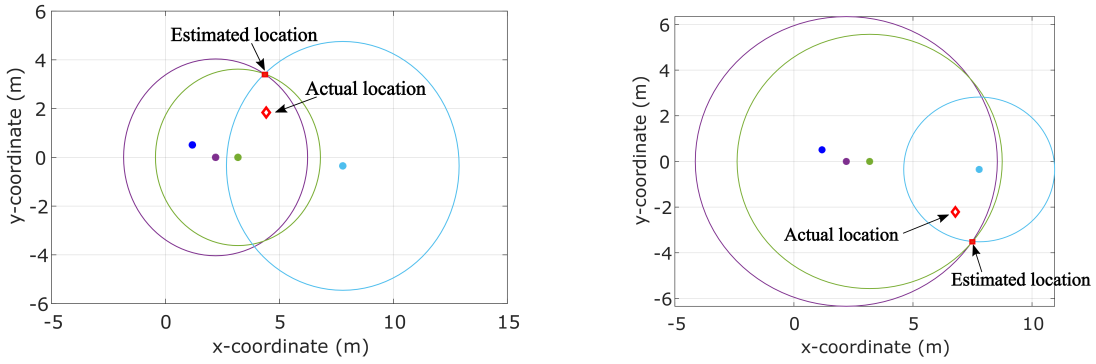

Figure 6.8: TOA based localization of (a) L4; (b) L3, using passive method

The EKF combined with TDOA is applied to localize two leaks L3 and L4. For the passive method, the time delay represents the time the leak signal takes to travel the length from the leak position to the hydrophone location. Therefore, the vector $h_i(\hat{x}_k^-)$ in this case is given by Eq. E.9. The Jacobian and the observation matrix R for each transmission line H1-H2, H2-H3, and H2-H5 are found using Eqs. E.10 and E.11, respectively. The initialization of the analysis is done with $\hat{\boldsymbol{x}}_k^-$ set at $\begin{bmatrix}10\\5\end{bmatrix}$ m (initial x and y value). The a priori covariance matrix, $\boldsymbol{P}_k^-$ is a 3X3 diagonal matrix with diagonal entries of 10. The location of the leak is then obtained using Eq. E.5. The true leak location (L3 and L4) compared to the estimated position by EKF is shown in Fig. 6.9. The result of the EKF with TDOA shows improved localization for both leaks compared to the TOA or TDOA approaches alone. For both L3 and L4, in the x-axis, the error is less than 5%, whereas,

in the y-axis, the error is reduced by more than 50%.

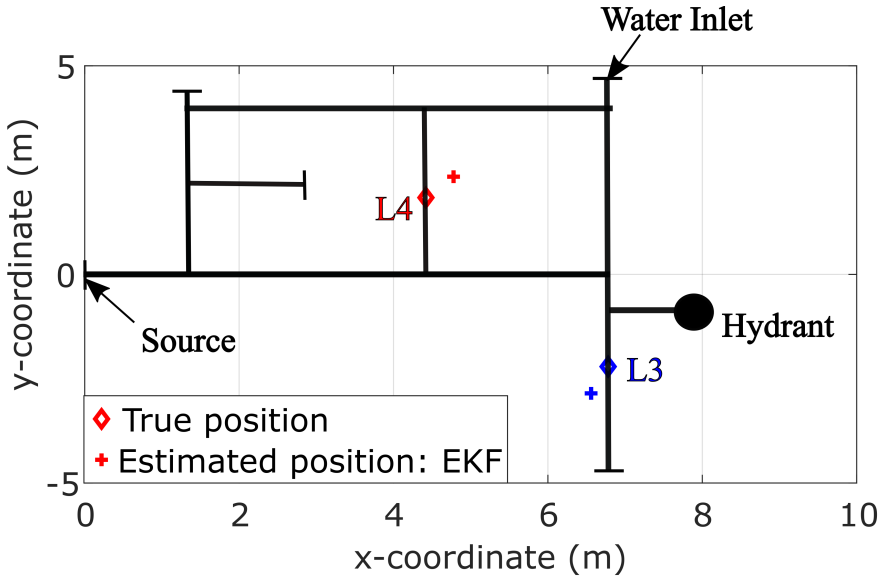

Figure 6.9: EKF applied as a smoother to TDOA technique to mitigate NLOS erros for estimation of L3 and L4 for the passive case

The ML method whose theoretical background is shown in Section E.2 can also be applied to improve the errors due to NLOS. For the passive method, the estimation of L4 using ML methods is shown in Fig. 6.10. The same time delay computed from the cross-correlation function are used alongside c to obtain the measured distance ($\hat{d}_i$) given in Eq. E.12. For all the x and y values with the increment of 0.1 m along the section of the pipe, the conditional probability density function (PDF) is found, and the value of x and y which maximizes the PDF expressed by Eq. E.15 is taken as the location of a leak in this case. The results in Figs. 6.10a and 6.10b shows the estimation of x and y coordinate in the WDNs. The comparison of ML estimation with EKF yields a similar conclusion.

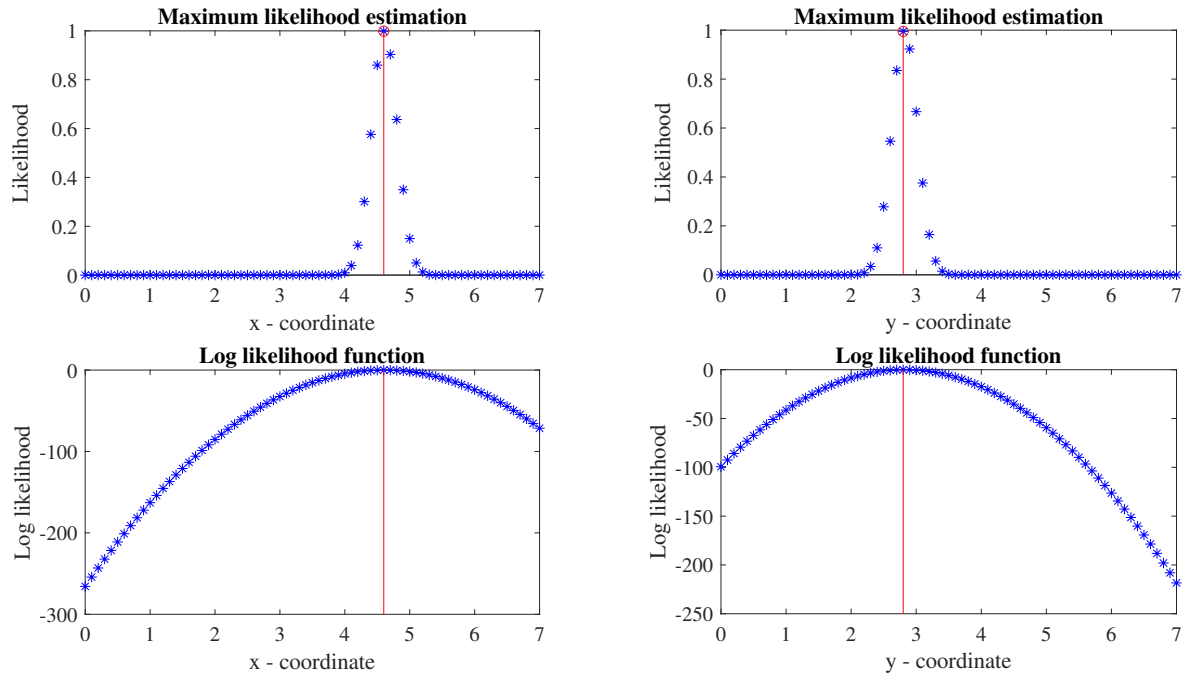

(a) (b)

Figure 6.10: L4 localization using ML method for passive method in the (a) x-coordinate; (b) y-coordinate

6.3 Active Method: Detection and Localization

The passive approach is susceptible to signal attenuation and external environmental factors and hence can be challenging when dealing with large WDNs. The active method can alleviate such issues as the input energy and the frequency bandwidth can be controlled to follow plane wave assumption and to reduce signal attenuation. This section, therefore, discusses the detection and localization of leaks using the active method where transmission and reflection coefficients and PSDs are used as a detection indicator of the leak while TOA, TDOA, and EKF are used as localization techniques. Relative performance of the active method versus the passive method is also discussed.

6.3.1 Validating power transmission and reflection coefficient as leak indicator in WDNs

With the successful implementation of power transmission and reflection coefficient as a leak indicator in a single pipe setup, the method is validated in WDN testbed. As previously mentioned in Section 5.3.1, 50% of the wave reflection occurs at approximately 13 Hz in the presence of leak based on Eq. 3.88. Furthermore, the leak is open to the environment so that the condition of the effective length L' ($L' = 1.7a$) is satisfied. This means that the range of frequencies where the leak can be detected using the reflected portion of the wave is approximately between 10 and 20 Hz (lower limit is due to the system harmonics present and the high-pass filter used). For validation, for L1 open, the pipe is excited with mono-frequency sine waves at 10 Hz. The test lasts 4 seconds and the signal is filtered using a high-pass Butterworth filter with a cutoff frequency of 5 Hz to remove low-frequency fluctuations before processing the data.

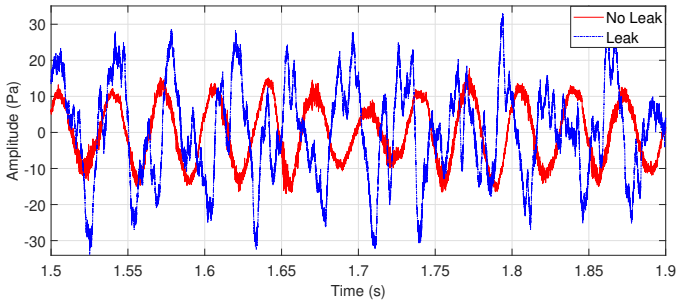

(a)

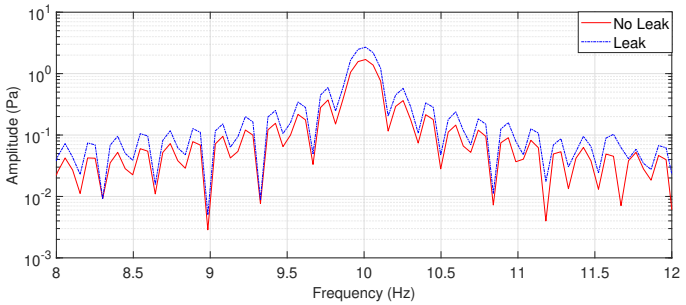

(b)

Figure 6.11: Comparison of leak L1 and no-leak responses recorded at H2 due to sine excitation from the source at 10 Hz: (a) time response; (b) Fourier transform

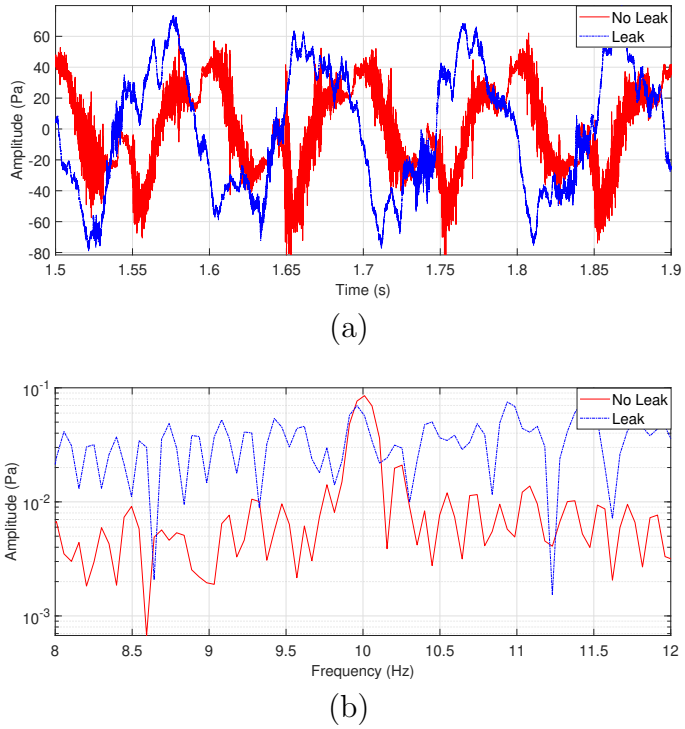

Figure 6.12: Comparison of leak and no-leak responses recorded at H5 due to sine excitation from the source at 10 Hz: (a) time response; (b) Fourier transform

For the 10 Hz sine harmonic, approximately 63% of the energy should theoretically be reflected at H2 due to the leak at L1. The resulting time trace and the FT of the data at H2 are shown in Fig. 6.11. The time trace and the FT due to the same leak collected at H5 are shown in Fig. 6.12. The results show that the energy of the 10 Hz wave is enhanced at the upstream sensor (H2) and decreased at the downstream sensor (H5), which is consistent with the single pipe case and the theoretical predictions. Apart from this, an additional test is performed with leak L3 open (results not shown here). In this test, it is observed that the magnitude of acoustic pressure is increased at both H2 and H5 locations, as both of these locations are upstream of the leak where the reflected component is measured.

6.3.2 Power spectral density (PSD) as a leak indicator

To test PSD as a leak indicator, one leak is assumed to be present at a time and open to the environment, while being excited using band-limited white noise, 1 to 100 Hz. The received signals are filtered using a 5th order high-pass Butter-worth filter with the cutoff frequency of 5 Hz to remove background noise due to water fluctuations prior to data processing. For each leak, a total of 18 tests each of duration 4 seconds are conducted, and the data is sampled at 4096 Hz.

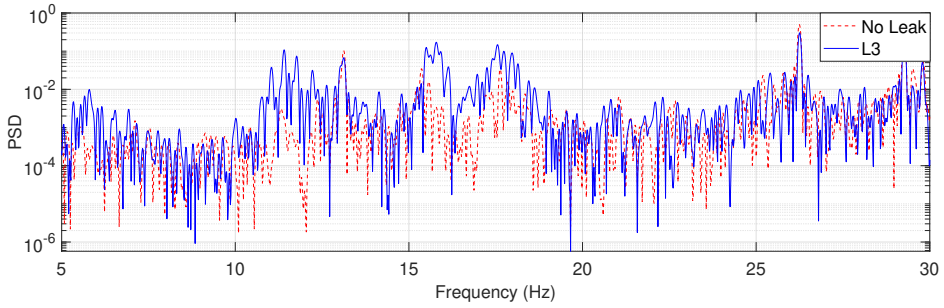

(a)

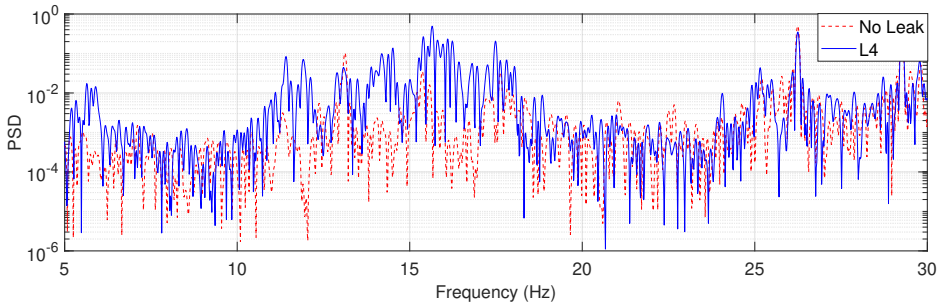

(b)

Figure 6.13: Comparison between PSD (H3) of no leak case and (a) L3; (b) L4

Since most of the leak signatures are observed in the low-frequency region (< 50 Hz), for leaks L3 and L4 (position shown in Fig. 6.1), the comparison of the PSD in the frequency range of 10 Hz and 30 Hz, with/without a leak, is shown in Fig. 6.13. For a coupled driver-pipe system, the properties of the driver are tightly linked to the properties of the pipe system. As mentioned previously in Section 3.4.2, the combined behavior of both pipe and driver influence the resonance of the system, as they are impedance-matched. If the behavior of the pipe changes, then this affects the driver's impedance. For instance, the

leak changes the impedance of the system, and this affects the impedance of the combined system, defined in Eq. 3.77. This change manifests in the spectral power when there is a leak in the system.

The spectral power difference between the leak and no leak cases can be easily distinguished even for a leak located at a significant distance from H3 such as L3. As expected, the difference in the PSD for the L4 case is even more pronounced. In general, leak results in the lifting of the spectrum, with the higher values associated with the leak case compared to when there is no leak present. The presence of junctions and the distance from H3 to both L3 and L4 are significantly different. However, the leak information is visible in frequency below 20 Hz, irrespective of the leak location. This difference in the PSD is directly related to the leak (due to the presence of reflections from the leak) and the change in the dynamics of the overall pipe-driver system. The test is repeated for 18 trials, and a consistent trend is observed in all the cases. This shows the effectiveness of using PSD as a simple detector even in a moderately complex system such as shown in Fig. 6.1.

6.3.3 Matrix pencil method (MPM) for time delay estimation

The fundamental quantity used for localization is the time delay at various receiver locations associated with the leak. This time delay is not easy to estimate, as the problem is one of disambiguation amongst various delays associated with the multi-path and direct acoustic path delays, which includes the leak-induced delay. The cross-correlation of two signals received at H1 and H2 can be treated using MPM to estimate the time delays associated with various propagation paths and impedance discontinuities. For the shown WDNs testbed, four hydrophones H1, H2, H3, and H5, are used to collect acoustic pressure data, and the cross-correlation functions between H1 and H2, H2 and H3, and H2 and H5 are calculated. The parameters such as phase and frequencies are extracted for each cross-correlation pair using MPM, which results in time delays corresponding to the exponentials in the discrete sum. The process is repeated for a total of 36 signals which consist of 18 leak and 18 no-leak signals, and the time delays corresponding to each hydrophone pair are aggregated. The histogram of time delays between the leak (L3) and no leak case for each hydrophone pair is shown in Fig. 6.14. As is evident, this disambiguation of the delays associated with leaks in a complex WDNs is only possible when a base case (when no leak is present) is available.

Fig. 6.14(a) shows the histogram of time delays estimated from the cross-correlation between H1 and H2 for both baseline data and the L3 leak case. Referring to Fig. 6.1, the signal from the source travels and is reflected to H2 due to the leak, resulting in a total real

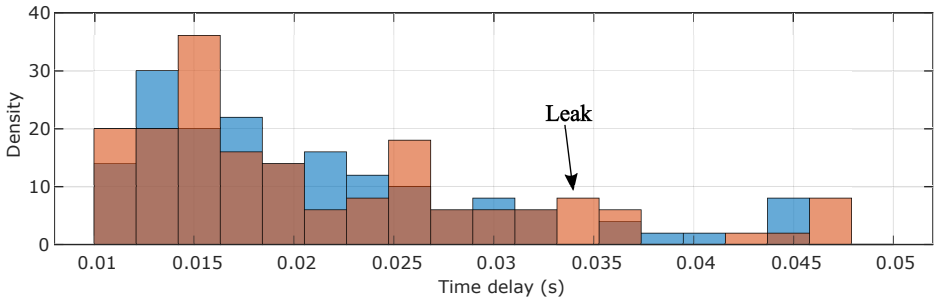

(a)

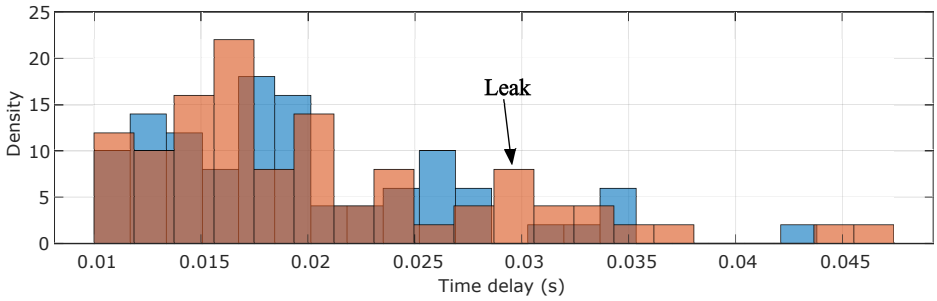

(b)

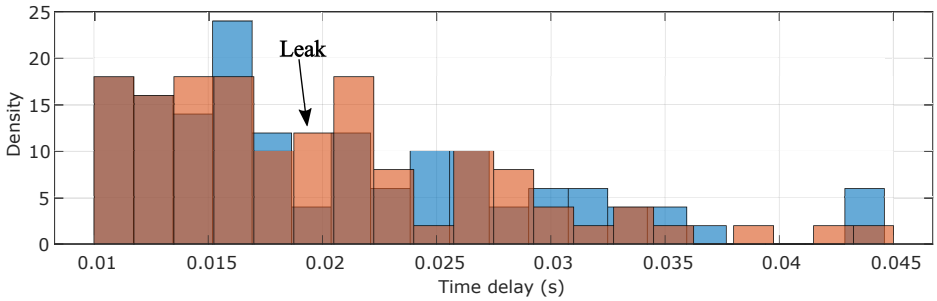

(b)

Figure 6.14: Comparison of leak and no-leak time delay responses when L3 is operated using data from: (a) H1 and H2; (b) H2 and H3; (b) H2 and H5

travel distance of 15.08 m. The histogram bar in Fig. 6.14(a) bounded by [0.033 0.035]s and centered at 0.034s locates the leak, which translates to a estimated distance bounded by [15.31 16.24] m and centered at 15.77 m. The histogram of time-delays between the leak and no leak cases using the cross-correlation function from H2 and H3 is shown in

Fig. 6.14(b). The signal travels from H2 to leak and gets reflected to H3, traveling a total true distance of 12.57 m. The bar in Fig. 6.14(b) bounded by [0.0287 0.0305]s and centered at 0.0296 s signifies the leak location, which gives the estimated distance bounded by [13.32 14.15] m and centered at 13.73 m. Similarly, for hydrophone pair H2 and H5, the bar in Fig. 6.14(c) bounded by [0.0187 0.0205]s and centered at 0.0196 s signifies the leak location, which gives the estimated distance bounded by [8.67 9.51] m and centered at 9.09 m. The actual traveling distance, in this case, is 9.6 m. The results show that the leak can be localized within 10% of the exact location. The time delay obtained for the L3 discussed in this paragraph for various hydrophone pairs is presented in table 6.1.

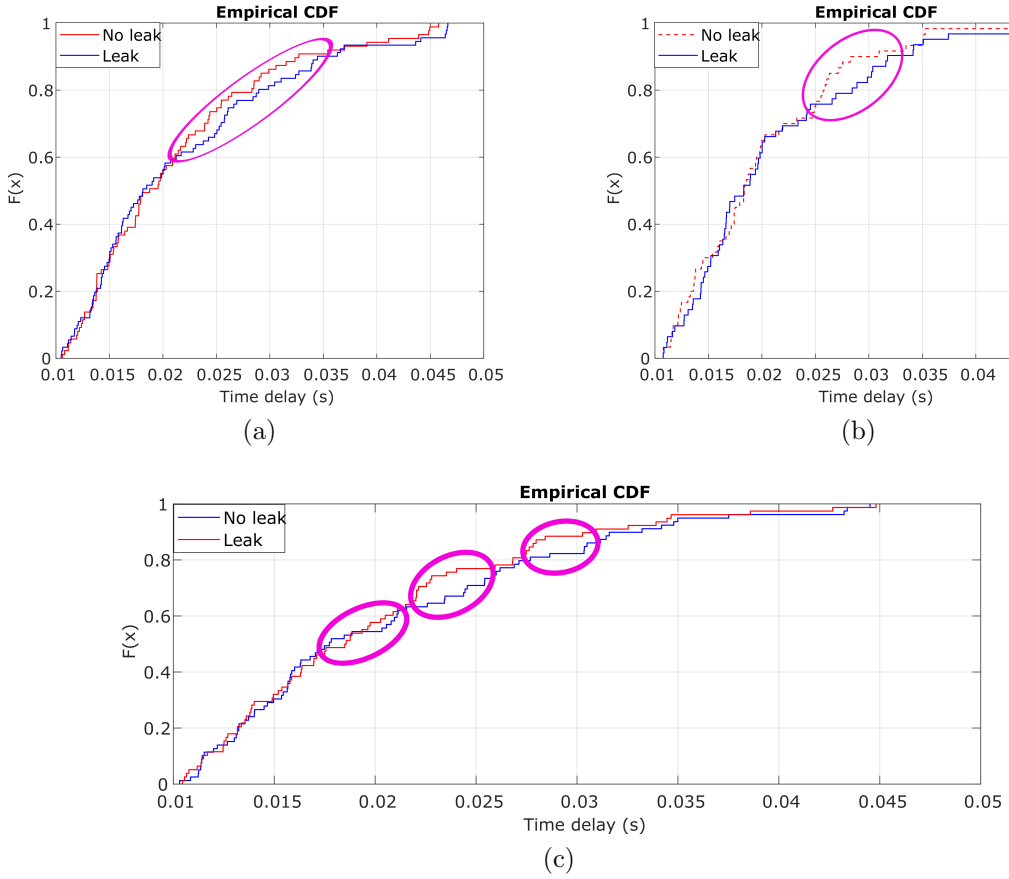

Figure 6.15: Comparison of empirical CDFs of the time delays between leak and no-leak time delay for L3 from: (a) H1 and H2; (b) H2 and H3; (b) H2 and H5

Table 6.1: Time delays for different hydrophone pairs in the WDNs

Hydrophone pair	H2 and H1	H2 and H3	H2 and H5
Time delay for L3	0.034	0.029	0.0196
Time delay for L4	0.018	0.015	0.0194

Furthermore, the comparison of empirical CDFs also indicates the presence of a leak. The empirical CDF associated with L3 for the same hydrophone pairs are shown in Fig. 6.15. Using the empirical CDFs, the location of the leak is represented by the region where the maximum deviation between the no-leak and leak CDFs occurs. Fig. 6.15(b) from H2 and H3 pair clearly represents the time delay introduced by the leak in the region [0.025 0.030]s, with the maximum deviation around 0.029 s. However, it is quite challenging for other hydrophone pairs to distinguish the exact time delay from the CDF plot alone. In the subsequent section, the study for leak localization is conducted employing the time delays obtained from the MPM.

6.3.4 Leak localization using multilateration techniques

For the case of single straight pipe section, the distance calculated using the time delay is sufficient to locate the leak. However, for complex WDNs, the localization is complicated due to multi-paths (NLOS condition), and hence distance alone is not sufficient to localize. Thus, MLAT methods such as TOA and TDOA are proposed with EKF smoothing as a means to localize the leak in WDNs.

MLAT techniques for the localization of L3 and L4 are explored using time delays obtained from different hydrophone pairs (reported in Table 6.1). Firstly, the TOA method is studied with data collected at the four hydrophone locations, H1, H2, H3, and H5. The time delays obtained using MPM from H1-H2, H2-H3, and H2-H5 pairs are used to draw three circles with centers at H2, H3, and H5, respectively. The intersection of the three circles (shown in Fig. 6.16) gives the probable leak location. Since the time delay represents the total distance the signal takes to travel, for, e.g., the time delay obtained from the H1-H2 pair due to L4 represents the time the signal takes to travel from H1 to L4 and reflect back to H2, opposed to the case in the passive method where the time delay represents the distance from the leak to the sensor location only. Therefore, the intersection of the three circles as shown in Fig. 6.16 represents a plane as opposed to point in the passive method. In this case, the quantity center of area is used as a metric to pinpoint the probable leak location from the area contained in the intersection. The comparison of probable leak location

corresponding to L3 and L4 compared to the actual position is shown in Fig. 6.17.

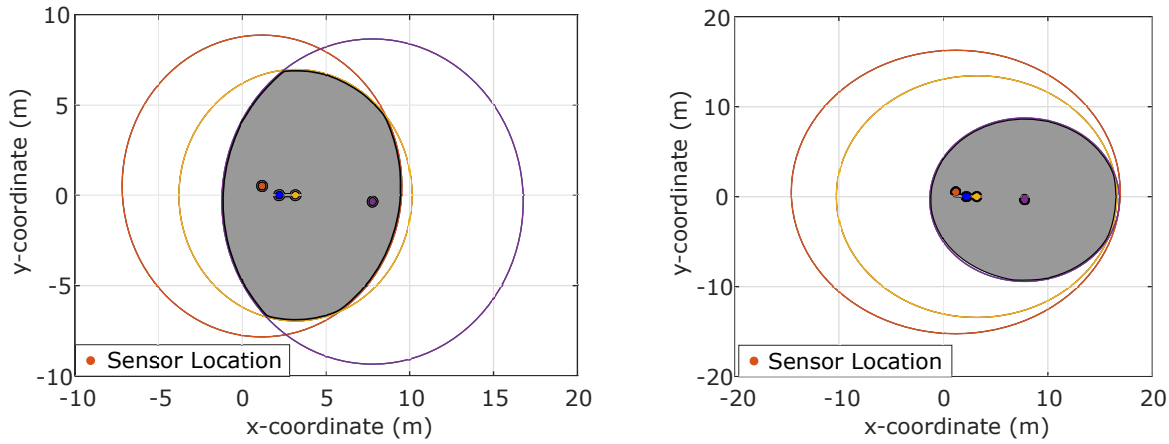

Figure 6.16: Intersection of the circles for localization of (a) L4; (b) L3 in WDNs using TOA method

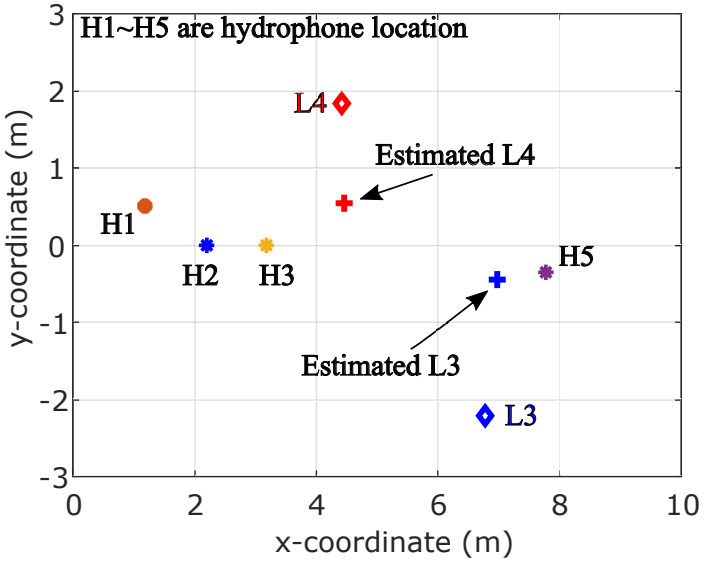

Figure 6.17: Localization of true and estimated leak location using TOA method

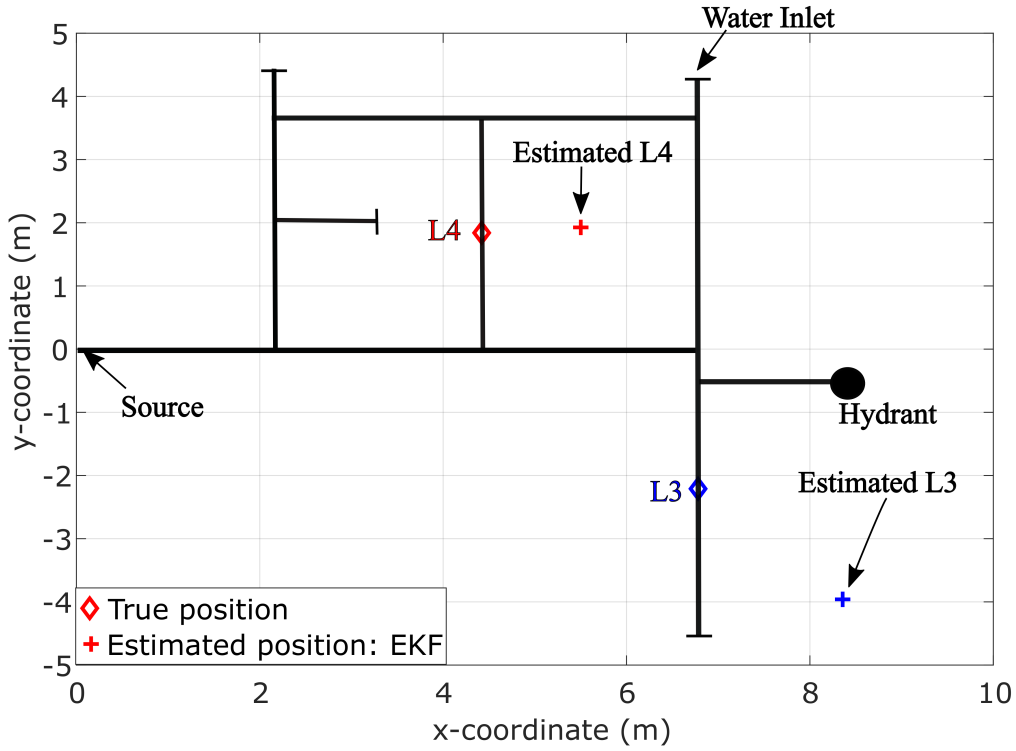

Figure 6.18: EKF applied as a smoother to TDOA technique to mitigate NLOS erros for estimation of L3 and L4 for active method

Similar to the passive method, EKF combined with TDOA is used to localize the two leaks L3 and L4. In this case, the time delay represents the time the signal generated by the source takes to travel from one hydrophone to leak and to another hydrophone. Therefore, the vector $h_i(\hat{x}_k^-)$ for this case is given by Eq. 21. The Jacobian and the observation matrix R for each transmission path H1-H2, H2-H3, and H2-H5 is found using Eqs. E.10 and E.11, respectively, in a process similar to the one used for the passive method. The initialization of the analysis is performed with $\hat{\boldsymbol{x}}_k^-$ set at $\begin{bmatrix}10\\5\end{bmatrix}$ m (initial x and y value). The a priori covariance matrix, $\boldsymbol{P}_k^-$ is a 3×3 diagonal matrix with diagonal entries of 10. The location of the leak is then obtained using Eq. E.5. The true leak location (L3 and L4) compared to the estimated position by EKF is shown in Fig. 6.18. From the results, it can be said that the localization error when applying the active method is higher compared to the estimates using the passive method. However, the attenuation issue prevalent in the

passive approach could favor the active method when dealing with large WDNs.

The localization accuracy can be improved using the insights gained from TOA and EKF analysis. The leak is already localized within 10% error using just the time delay. Combining EKF and TOA and using the total distance obtained from the hydrophone pairs, and taking into account the physical geometry of the WDNs, the error can be further reduced. For example, based on earlier multilateration analysis, the probable L3 location is likely in the fourth quadrant. Using the H1-H2 pair from the MPM study, the signal travels 15.77 m from H1 before returning to H2 due to reflection from L3. Similarly, for L4, the probable location is likely in the first quadrant. Using the same H1-H2 pair from the MPM study, the signal traveled 8.35 m from H1 before returning to H2 due to reflection from L4. Tracing the distance for both L3 and L4 obtained from MPM along the physical acoustic path towards the fourth and first quadrant, respectively, yields the location of the leak within 5% of the actual leak location.

Similar to the passive method, the maximum likelihood (ML) method is also used with the active method to improve the localization. Figure 6.16 shows the intersection of the circles based on the TOA method, and the region bounded by the circles gives the probable location of the leak. The ML method can be applied in that region, and for each x and y value, the PDF can be found. The value for which the PDF is maximum is the estimated leak location. The result of the active method is shown in Fig. 6.19. Unlike the passive method, the bias b_i, in this case, is tuned with a parameter $\lambda = 2.8$, and the x and y coordinate estimation are shown in Figs. 6.19a and 6.19b, respectively.

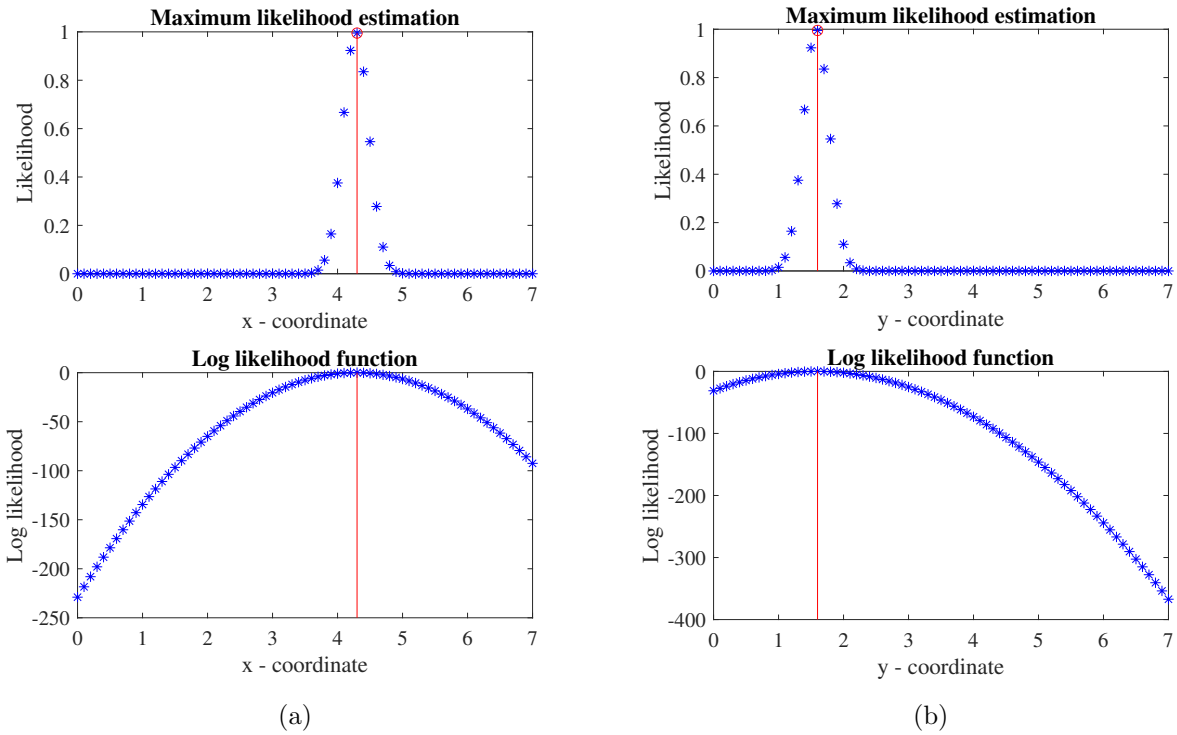

(a) (b)

Figure 6.19: L4 localization using ML method for active method in the (a) x-coordinate; (b) y-coordinate

6.4 Summary

This chapter presents the experimental implementation of localization in WDNs using both passive and active approaches. The PSDs and power coefficients are shown as simple leak indicators, even when the sensors are located relatively distant from the measurement locations. Techniques of multilateration using TOA and TDOA, which have thus far been used in telecommunication and mobile networking fields, are shown here to be effective for leak localization as well. Furthermore, EKF, when used with TDOA, can reduce the localization error due to NLOS prevailing in WDNs. Also, the ML method for mitigating errors due to NLOS is also studied for both passive and active methods. However, estimating bias parameters for localization is essential, and further study is required to refine this method.

Chapter 7

Concluding Remarks

7.1 Summary of Contributions

While the physics of acoustic wave behavior is well understood, there is relatively scarce literature on their application to leak detection in water-filled pipes and pipe networks. This thesis is perhaps the first to investigate active acoustics for leak detection and localization in water-filled pipes in a network. This method involves injecting acoustic waves into a pipe network, which makes it robust to signal energy attenuation and ambient noise. The frequency content of acoustic waves can be controlled to reduce interference with background noise, while input power can be varied to compensate for attenuation. The underlying principle in this approach is that a traveling wave interacts with defects such as leaks causing reflections at impedance discontinuities, which can then be probed at the source or within a pipe network to detect and locate leaks. For the development of the methods and their validation, first a single straight pipe which is representative of those found in the field in terms of material and diameter is used. This is then enlarged to a more realistic WDNs with junctions and multiple leaks to validate the detection and localization methods developed on the straight section. The following are claimed as the main contributions to the field resulting from this thesis work.

In terms of primary contribution, this dissertation presents for the first time—to the knowledge of the author—active leak-detection and localization using an acoustic source in water-filled pipes. The use of active acoustics as a means of leak detection and localization in PVC WDNs is novel and has been shown in this thesis to offer significant potential in terms of outperforming their passive counterparts. Previous applications of similar approaches have been limited to air-filled ducts, not in the field of water distribution systems to moni-

tor for leaks. Also, the source used for generating acoustic signals can be placed directly in the water column, and the leak monitoring technique relies entirely on sound waves propagating within the fluid medium. Unlike solenoid devices, applied in many of the studies in the literature, the source does not produce perceptible motions of the fluid. This makes the approach developed in this thesis attractive from a practical implementation standpoint.

The primary conclusions stemming from this thesis can be summarized as follows:

1. The use of acoustic wave theory and its application to fluid-filled pipe systems for leak detection and localization, which has not been shown before, is demonstrated in this thesis. The main conclusions of this work are as follows:

   (a) The detection method based on power transmission and reflection coefficient obtained from the impedance due to the leak is shown to be a powerful indicator. Theory on power transmission and reflection suggests that in order for reflections to be observed, the excitation frequencies should be quite low, as low as 13 Hz for the pipe experiments shown. The method relies on reflected or transmitted signal components and comparing it with the baseline data from a single sensor and results from several low-frequency tests showed good agreement with predictions from theory. This is shown to be a relatively easy and cost-effective detection technique that can be placed either upstream or downstream of the leak.

   (b) The two microphones based technique was also demonstrated in this thesis as a viable means to obtaining system resonance conditions and for developing a powerful leak indicator based on reflected wave spectral density and transmission loss. However, this method was deemed quite cumbersome for large scale WDNs.

2. The traditional cross-correlation method used in passive methods cannot be used to localize leaks for the active case, as the active source signal involved in direct transmission dominates the acoustic field, which renders separating the leak-induced time delay from the time delay due to this direct transmission part quite challenging.

3. Time-delay estimation techniques such as the Prony's method and the MPM were found to be powerful tools in the detection and localization of impedance changes. The highlights from this development are as follows:

   (a) The sensitivity of reflected waves due to the leak is well captured by Prony's method when applied to the cross-correlation obtained from two hydrophone signals. The statistical analysis of the time delays helps in detection, localization and to estimating the experimental wave speed simultaneously.

(b) The MPM developed by solving the generalized eigenvalue problems results in similar estimates compared to Prony's. The implementation of these techniques in laboratory-based single and relatively complex WDNs established that this approach is robust and computationally efficient for leak monitoring and can be scaled to more extensive networks.

4. A novel spectral mean shift clustering-based pre-processing approach is also shown as a powerful technique that just requires a single hydrophone to detect and localize leaks. The pre-processing approach aims to enhance the time-frequency representation of a hydrophone signal and the time-delay information extracted from the enhanced time-frequency representation is used in conjunction with the wave speed to detect and localize leaks. The efficacy of this method is verified in an experiment using a single pipe setup.

5. The water distribution network is a combination of several pipes that has several elbows, junctions, end-cap, etc. The localization in the network is not as simple as in a single pipe, as there are multiple acoustic paths in the network. Therefore, relying on time delay alone is not adequate to locate leaks. Thus the multilateration (MLAT) commonly used in networking and global positioning is considered for water leak monitoring. The main conclusions from this study are as follows:

   (a) TOA and TDOA are are shown to contain leak location information and can enable leak localization in both simple and complex pipe configurations.

   (b) The EKF is shown to reduce errors due to NLOS condition when used with TDOA.

7.2 Limitations of the Study

There are some limitations in this study which are highlighted below:

1. The analysis conducted in this thesis is limited to lab experiments. Although a lot of attention was given to constructing the test setup to closely replicate real-life WDNs, few conditions such as burial conditions which can affect signal energy loss could not be simulated. For the passive method, the problem of attenuation was observed even in the lab WDNs. For the active method, however, the effect of attenuation could not be studied because of the limited size WDNs.

2. Only one leak (pinhole type) was simulated during experimental studies at a time, and the effect of multiple leaks occurring simultaneously was not addressed in this study. Moreover, the studies associated with a crack or other leak, such as one occurring due to inadequate sealing between components and/or leak operating at a variable flow rate was not covered in this thesis.

3. The detection and localization was based on comparing the experimental results with the baseline characteristics. This means that the framework as presented in this thesis can only detect newly forming leaks and not existing leak(s).

4. The study is conducted on a setup with fixed diameter pipes throughout and is constructed out of PVC. Variable diameter pipes and heterogeneous pipe materials were not studied, despite being a part of the initial experimental plan (which was scaled back due to COVID).

5. Leak quantification from acoustic data was also not pursued in this thesis.

6. The source is oriented longitudinally within the pipe, and this is the desired orientation even in field settings. This may pose implementation challenges and will potentially require careful placement considerations and additional hardware design.

7. In the real-world water distribution network, pipelines constructed out of different materials and variable diameters are used depending on the need. This makes the localization challenging as the acoustic wave traveling in those pipe sections results in varying time differences due to changes in c. Therefore, tackling this issue is one of the challenges in this method. Action like selecting the pipe network or area with similar pipe geometry and material and working in that particular section one at a time may be a way to address this problem, but this approach is laborious and tedious.

7.3 Ongoing Work and Directions for Future Study

Unarguably, there are many gaps in this thesis work which remain to be addressed. While experiments on a single pipe and lab-based WDNs have yielded promising results, it is unclear how this method would perform in real-life WDNs which are comprised of more complex geometries and not homogeneous. While the following list is not expected to be comprehensive, here are some of the main directions which can pursued in the future:

1. Despite best efforts to reproduce field conditions, the experimental set up in this thesis is still fairly simple. An obvious next step is to validate and further develop these methods in field experiments comprising of varying material and geometries.

2. More laboratory experiments to study the effect on leak signatures due to variable leak diameter, water pressure, or multiple leaks running simultaneously could be valuable extensions of this work.

3. Furthermore, there is a need to develop new active methods to identify existing leaks, rather than relying on a baseline. This should theoretically be possible if the pipe layout, materials and geometries are know; however, as seen in the experimental data, processing acoustic date and inferring impedance related information from it can be quite challenging.

4. Multilateration techniques for leak localization in complex WDNs which are associated with NLOS conditions is still a very new area (this is the first thesis which has explored this application) and is worthy of exploring further. There is potential to reduce the NLOS induced errors further, for example using more advanced filtering techniques such as particle filters.

Bibliography

[1] Sunil Sinha, Preet Singh, Irving Oppenhiem, David Iseley, Anne Khademian, Marc Edwards, Jose Perdomo, and Walter Graf. Smart pipeline infrastructure network for energy and water (spine). In *Pipelines 2015*, pages 1825–1834. 2015.

[2] Yaqing Tu and Huabo Chen. Design of oil pipeline leak detection and communication system based on optical fiber technology. In *Design and Engineering of Optical Systems II*, volume 3737, pages 584–593. International Society for Optics and Photonics, 1999.

[3] Pal Stefan Murvay and Ioan Silea. A survey on gas leak detection and localization techniques. *Journal of Loss Prevention in the Process Industries*, 25(6):966–973, 2012.

[4] R. Puust, Z. Kapelan, D. A. Savic, and T. Koppel. A review of methods for leakage management in pipe networks. *Urban Water Journal*, 7(1):25–45, 2010.

[5] Y. Gao, M. J. Brennan, P. F. Joseph, J. M. Muggleton, and O. Hunaidi. On the selection of acoustic/vibration sensors for leak detection in plastic water pipes. *Journal of Sound and Vibration*, 283(3-5):927–941, 2005.

[6] Malcolm Farley and Stuart Trow. *Losses in water distribution networks*. IWA publishing, 2003.

[7] Nina Golgowski. Water-main break floods ucla campus, sunset boulevard with 8 to 10 million gallons of water. *Daily News, Online Search*, 06/29/2014.

[8] Murray N Charlton and Jacqui Milne. *Review of thirty years of change in Lake Erie water quality*. National Water Research Institute, 2004.

[9] Steven Folkman. Water main break rates in the USA and Canada: A comprehensive study. *Mechanical and Aerospace Engineering Faculty publications*, 2018.

[10] P.J. Lee, H.F. Duan, J. Tuck, and M. Ghidaoui. Numerical and Experimental Study on the Effect of Signal Bandwidth on Pipe Assessment Using Fluid Transients. *American Society of Civil Engineers*, 141(2):1–10, 2014.

[11] Lai Cheng Cheong. Unaccounted for water and the economics of leak detection. In *Proc. International Water Supply Congress and Exhibition, Copenhagen. Water Supply*, volume 9, 1991.

[12] MAI Chowdhury, MF Ahmed, and MA Gaffar. Water system leak detection in secondary towns of bangladesh. *Water Supply*, 17(3):343–349, 1999.

[13] Kenneth J Brothers. Water leakage and sustainable supply-truth or consequences? *Journal (American Water Works Association)*, 93(4):150–152, 2001.

[14] Laura Wood. Global non-revenue water losses of about 40 billion is driving growth opportunities for smart water leakage management solutions. *GlobeNewswire, Research and Markets*, 10/24/2018.

[15] Andrew F. Colombo and Bryan W. Karney. Energy and Costs of Leaky Pipes: Toward Comprehensive Picture. *Journal of Water Resources Planning and Management*, 128(6):441–450, 2002.

[16] Mark W LeChevallier, Richard W Gullick, Mohammad R Karim, Melinda Friedman, and James E Funk. The potential for health risks from intrusion of contaminants into the distribution system from pressure transients. *Journal of Water and Health*, 1(1):3–14, 2003.

[17] PFM Teunis, M Xu, KK Fleming, J Yang, CL Moe, and MW LeChevallier. Enteric virus infection risk from intrusion of sewage into a drinking water distribution network. *Environmental science & technology*, 44(22):8561–8566, 2010.

[18] Ontario MOECC. Design guidelines for drinking-water systems. 2008.

[19] Osama Hunaidi and Wing T Chu. Acoustical characteristics of leak signals in plastic water distribution pipes. *Applied Acoustics*, 58:235–254, 1999.

[20] City of Guelph. *District Metering Area 11 of City of Guelph Water Service*. City of Guelph Water Service, 2018.

[21] Rui Li, Haidong Huang, Kunlun Xin, and Tao Tao. A review of methods for burst/leakage detection and location in water distribution systems. *Water Science & Technology: Water Supply*, 15(3):429, 2015.

[22] Marshal Deep Kafle and Sriram Narasimhan. Active acoustic leak detection in a pressurized pvc pipe. *Urban Water Journal*, 17(4):315–324, 2020.

[23] Y. A. Khulief, A. Khalifa, R. Ben Mansour, and M. A. Habib. Acoustic Detection of Leaks in Water Pipelines Using Measurements inside Pipe. *Journal of Pipeline Systems Engineering and Practice*, 3(2):47–54, 2012.

[24] Alessandro Stuart Savoia, Barbara Mauti, and Giosuè Caliano. A low frequency broadband flextensional ultrasonic transducer array. *IEEE Transactions on Ultrasonics, Ferroelectrics, and Frequency Control*, 63(1):128–138, 2015.

[25] J Thorton. Water loss control manual, 2002.

[26] Balvant Rajani and Yehuda Kleiner. Non-destructive inspection techniques to determine structural distress indicators in water mains. *Evaluation and Control of Water Loss in Urban Water Networks*, pages 21–25, 2004.

[27] Julian Thornton, Reinhard Sturm, and George Kunkel. *Water loss control*. McGraw-Hill Education, 2008.

[28] Andrew F. Colombo, Pedro Lee, and Bryan W. Karney. A selective literature review of transient-based leak detection methods. *Journal of Hydro-Environment Research*, 2(4):212–227, 2009.

[29] Shantanu Datta and Shibayan Sarkar. A review on different pipeline fault detection methods. *Journal of Loss Prevention in the Process Industries*, 41:97–106, 2016.

[30] Chun Hua Tian, Jun Chi Yan, Jin Huang, Yu Wang, Dong-Sup Kim, and Tongnyoul Yi. Negative pressure wave based pipeline Leak Detection: Challenges and algorithms. *Proceedings of 2012 IEEE International Conference on Service Operations and Logistics, and Informatics*, pages 372–376, 2012.

[31] Zheng Liu and Yehuda Kleiner. State of the art review of inspection technologies for condition assessment of water pipes. *Measurement: Journal of the International Measurement Confederation*, 46(1):1–15, 2013.

[32] T. K. Chan, Cheng Siong Chin, and Xionghu Zhong. Review of Current Technologies and Proposed Intelligent Methodologies for Water Distributed Network Leakage Detection. *IEEE Access*, 6:78846–78867, 2019.

[33] Junrong Liu, Jun Yao, Mike Gallaher, Jeff Coburn, and Roger Fernandez. Study on methane emission reduction potential in chinas oil and natural gas industry. Technical report, Tech. rep., April, 2008.

[34] James A Liggett and Li-Chung Chen. Inverse transient analysis in pipe networks. *Journal of Hydraulic Engineering*, 120(8):934–955, 1994.

[35] Ranko S Pudar and James A Liggett. Leaks in pipe networks. *Journal of Hydraulic Engineering*, 118(7):1031–1046, 1992.

[36] Lennart Jönsson and Magnus Larson. Leak detection through hydraulic transient analysis. In *Pipeline systems*, pages 273–286. Springer, 1992.

[37] Reinaldo A Silva, Claudio M Buiatti, Sandra L Cruz, and João AFR Pereira. Pressure wave behaviour and leak detection in pipelines. *Computers & chemical engineering*, 20:S491–S496, 1996.

[38] Huan-Feng Duan, Pedro J. Lee, Mohamed S. Ghidaoui, and Yeou-Koung Tung. Leak detection in complex series pipelines by using the system frequency response method. *Journal of Hydraulic Research*, 49(2):213–221, 2011.

[39] Pedro J. Lee, John P. Vítkovský, Martin F. Lambert, Angus R. Simpson, and James Liggett. Leak location in pipelines using the impulse response function. *Journal of Hydraulic Research*, 45(5):643–652, 2007.

[40] P J Lee, M F Lambert, A R Simpson, and J P Vitkovsky. Experimental verification of the frequency response method for pipeline leak detection. *Journal of Hydraulic Research*, 44(5):693–707, 2006.

[41] P.J. Lee, J.P. Vítkovský, M.F. Lambert, A.R. Simpson, and J.A. Liggett. Frequency domain analysis for detecting pipeline leaks. *Journal of Hydraulic Engineering*, 131(7):596–604, 2005.

[42] Pedro J. Lee, John P. Vítkovský, Martin F. Lambert, Angus R. Simpson, and James A. Liggett. Leak location using the pattern of the frequency response diagram in pipelines: A numerical study. *Journal of Sound and Vibration*, 284(3-5):1051–1073, 2005.

[43] Zheng Yi Wu, Paul Sage, and David Turtle. Pressure-Dependent Leak Detection Model and Its Application to a District Water System. *Journal of Water Resources Planning and Management*, 136(1):116–128, 2010.

[44] Guoliang Ye and Richard Andrew Fenner. Kalman Filtering of Hydraulic Measurements for Burst Detection in Water Distribution Systems. *Journal of Pipeline Systems Engineering and Practice*, 2(1):14–22, 2011.

[45] Ramon Perez, Gerard Sanz, Vicenc Puig, Joseba Quevedo, Miquel Angel Cuguero Escofet, Fatiha Nejjari, Jordi Meseguer, Gabriela Cembrano, Josep M. Mirats Tur, and Ramon Sarrate. Leak localization in water networks: A model-based methodology using pressure sensors applied to a real network in barcelona [applications of control]. *IEEE Control Systems*, 34(4):24–36, 2014.

[46] Z. Poulakis, D. Valougeorgis, and C. Papadimitriou. Leakage detection in water pipe networks using a Bayesian probabilistic framework. *Probabilistic Engineering Mechanics*, 18(4):315–327, 2003.

[47] S. R. Mounce, J. B. Boxall, and J. Machell. Development and Verification of an Online Artificial Intelligence System for Detection of Bursts and Other Abnormal Flows. *Journal of Water Resources Planning and Management*, 136(3):309–318, 2010.

[48] Adrià Soldevila, Rosa M. Fernandez-Canti, Joaquim Blesa, Sebastian Tornil-Sin, and Vicenç Puig. Leak localization in water distribution networks using Bayesian classifiers. *Journal of Process Control*, 55:1–9, 2017.

[49] Paul Sage. Developments in use of network models for leakage management at united utilities north west. In *CIWEM North West and North Wales Branch Water Treatment and Distribution Conference, Warrington, UK*, pages 1–31, 2005.

[50] Osama Hunaidi, Wing Chu, Alex Wang, and Wei Guan. Detecting leaks in plastic pipes. *Journal-American Water Works Association*, 92(2):82–94, 2000.

[51] Osama Hunaidi and Peter Giamou. Ground-penetrating radar for detection of leaks in buried plastic water distribution pipes. *Proceedings of the 7th International Conference on Ground Penetrating Radar*, (May):783–786, 1998.

[52] Albane Saintenoy and Jan W. Hopmans. Ground Penetrating Radar: Water Table Detection Sensitivity to Soil Water Retention Properties. *IEEE Journal of Selected Topics in Applied Earth Observations and Remote Sensing*, 4(4):748–753, 2011.

[53] Mohamed Fahmy and Osama Moselhi. Automated Detection and Location of Leaks in Water Mains Using Infrared Photography. *Journal of Performance of Constructed Facilities*, 24(3):242–248, 2010.

[54] Sunil K Sinha and Fakhri Karray. Classification of underground pipe scanned images using feature extraction and neuro-fuzzy algorithm. *IEEE Transactions on Neural Networks*, 13(2):393–401, 2002.

[55] Majid Ahadi and Mehrdad Sharif Bakhtiar. Leak detection in water-filled plastic pipes through the application of tuned wavelet transforms to acoustic emission signals. *Applied Acoustics*, 71(7):634–639, 2010.

[56] Osama Hunaidi, Alex Wang, M. Bracken, T Gambino, and C Fricke. Acoustic methods for locating leaks in municipal water pipe networks. *International Water Demand Management Conference*, pages 1–14, 2004.

[57] Roya Cody, Jinane Harmouche, and Sriram Narasimhan. Leak detection in water distribution pipes using singular spectrum analysis. *Urban Water Journal*, 15(7):636–644, 2018.

[58] Alberto Martini, Marco Troncossi, and Alessandro Rivola. Vibroacoustic measurements for detecting water leaks in buried small-diameter plastic pipes. *Journal of Pipeline Systems Engineering and Practice*, 8(4):04017022, 2017.

[59] Alberto Martini, Alessandro Rivola, and Marco Troncossi. Autocorrelation analysis of vibro-acoustic signals measured in a test field for water leak detection. *Applied Sciences*, 8(12):2450, 2018.

[60] Sepideh Yazdekhasti, Kalyan R Piratla, Jacob Sorber, Sez Atamturktur, Abdul Khan, and Harshit Shukla. Sustainability analysis of a leakage-monitoring technique for water pipeline networks. *Journal of Pipeline Systems Engineering and Practice*, 11(1):04019052, 2020.

[61] Hao Jin, Laibin Zhang, Wei Liang, and Qikun Ding. Integrated leakage detection and localization model for gas pipelines based on the acoustic wave method. *Journal of Loss Prevention in the Process Industries*, 27:74–88, 2014.

[62] J. D. Butterfield, A. Krynkin, R. P. Collins, and S. B M Beck. Experimental investigation into vibro-acoustic emission signal processing techniques to quantify leak flow rate in plastic water distribution pipes. *Applied Acoustics*, 119:146–155, 2017.

[63] Zhenlin Li, Haifeng Zhang, Dongjie Tan, Xin Chen, and Hongxiang Lei. A novel acoustic emission detection module for leakage recognition in a gas pipeline valve. *Process Safety and Environmental Protection*, 105(51):32–40, 2017.

[64] SR Haqshenas and W. Kropp. Leak detection in plastic water pipe using pulse-echo method. *Department of Civil and Environmental Engineering*, Master:50, 2010.

[65] Charles H. Knapp and G. Clifford Carter. The Generalized Correlation Method for Estimation of Time Delay. *IEEE Transactions on Acoustics, Speech, and Signal Processing*, 24(4):320–327, 1976.

[66] Y. Gao, M. J. Brennan, and P. F. Joseph. A comparison of time delay estimators for the detection of leak noise signals in plastic water distribution pipes. *Journal of Sound and Vibration*, 292(3-5):552–570, 2006.

[67] Yan Gao, Michael J. Brennan, Yuyou Liu, Fabrício C.L. Almeida, and Phillip F. Joseph. Improving the shape of the cross-correlation function for leak detection in a plastic water distribution pipe using acoustic signals. *Applied Acoustics*, 127:24–33, 2017.

[68] Peter R Roth. Effective measurements using digital signal analysis. *IEEE spectrum*, 8(4):62–70, 1971.

[69] G Clifford Carter, Albert H Nuttall, and Peter G Cable. The smoothed coherence transform. *Proceedings of the IEEE*, 61(10):1497–1498, 1973.

[70] Alfred Hero and S Schwartz. A new generalized cross correlator. *IEEE transactions on acoustics, speech, and signal processing*, 33(1):38–45, 1985.

[71] G Clifford Carter. Coherence and time delay estimation. *Proceedings of the IEEE*, 75(2):236–255, 1987.

[72] Didem Ozevin and James Harding. Novel leak localization in pressurized pipeline networks using acoustic emission and geometric connectivity. *International Journal of Pressure Vessels and Piping*, 92:63–69, 2012.

[73] Bruno Brunone, Marco Ferrante, and Silvia Meniconi. Portable pressure wave-maker for leak detection and pipe system characterization. *Journal-American Water Works Association*, 100(4):108–116, 2008.

[74] S. Kim. Inverse transient analysis for a branched pipeline system with leakage and blockage using impedance method. *Procedia Engineering*, 89:1350–1357, 2014.

[75] Si Tran Nguyen Nguyen, Jinzhe Gong, Martin F Lambert, Aaron C Zecchin, and Angus R Simpson. Least squares deconvolution for leak detection with a pseudo random

binary sequence excitation. *Mechanical Systems and Signal Processing*, 99:846–858, 2018.

[76] Xun Wang, Muhammad Waqar, Hao-Chen Yan, Moez Louati, Mohamed S Ghidaoui, Pedro J Lee, Silvia Meniconi, Bruno Brunone, and Bryan Karney. Pipeline leak localization using matched-field processing incorporating prior information of modeling error. *Mechanical Systems and Signal Processing*, 143:106849, 2020.

[77] Fabrício C.L. Almeida, Michael J. Brennan, Phillip F. Joseph, Simon Dray, Stuart Whitfield, and Amarildo T. Paschoalini. Towards an in-situ measurement of wave velocity in buried plastic water distribution pipes for the purposes of leak location. *Journal of Sound and Vibration*, 359:40–55, 2015.

[78] Pedro Lee, Jeffrey Tuck, Mark Davidson, and Robert May. Piezoelectric wave generation system for condition assessment of field water pipelines. *Journal of Hydraulic Research*, 55(5):721–730, 2017.

[79] Jinzhe Gong, Martin F Lambert, Si TN Nguyen, Aaron C Zecchin, and Angus R Simpson. Detecting thinner-walled pipe sections using a spark transient pressure wave generator. *Journal of Hydraulic Engineering*, 144(2):06017027, 2018.

[80] K A Papadopoulou, M N Shamout, B Lennox, D Mackay, A R Taylor, J T Turner, and X Wang. An evaluation of acoustic reflectometry for leakage and blockage detection. *Proceedings of the Institution of Mechanical Engineers, Part C: Journal of Mechanical Engineering Science*, 222(6):959–966, 2008.

[81] A C Jackson, J P Butler, E J Millet, F G Hoppin, and S V Dawson. Airway geometry by analysis of acoustic pulse response measurements. *Journal of applied physiology (Bethesda, Md. : 1985)*, 43(3):523–536, 1977.

[82] Ian Marshall, Michael Rogers, and Gordon Drummond. Acoustic reflectometry for airway measurement. Principles, limitations and previous work. *Clinical Physics and Physiological Measurement*, 12(2):131–141, 1991.

[83] Jeffrey J Fredberg, ME Wohl, GARY M Glass, and HENRY L Dorkin. Airway area by acoustic reflections measured at the mouth. *Journal of Applied Physiology*, 48(5):749–758, 1980.

[84] D B Sharp and D M Campbell. Leak detection in pipes using acoustic pulse reflectometry. *Acustica*, 83(3):560–566, 1997.

[85] Moez Louati and Mohamed S. Ghidaoui. High-frequency acoustic wave properties in a water-filled pipe. Part 1: dispersion and multi-path behaviour. *Journal of Hydraulic Research*, 55(5):613–631, 2017.

[86] AP Watson and JM Bowsher. Impulse measurements on brass musical instruments. *Acta Acustica united with Acustica*, 66(3):170–174, 1988.

[87] Moez Louati and Mohamed S. Ghidaoui. High-frequency acoustic wave properties in a water-filled pipe. Part 2: range of propagation. *Journal of Hydraulic Research*, 55(5):632–646, 2017.

[88] Fabrício César Lobato De Almeida, Michael John Brennan, Phillip Frederick Joseph, Simon Dray, Stuart Whitfield, and Amarildo Tabone Paschoalini. Measurement of wave attenuation in buried plastic water distribution pipes. *Strojniski Vestnik/Journal of Mechanical Engineering*, 60(5):298–306, 2014.

[89] Xun Wang, Jingrong Lin, Alireza Keramat, Mohamed S Ghidaoui, Silvia Meniconi, and Bruno Brunone. Matched-field processing for leak localization in a viscoelastic pipe: An experimental study. *Mechanical Systems and Signal Processing*, 124:459–478, 2019.

[90] Hanafi M. Yusop, M. F. Ghazali, M. F.M. Yusof, and W. S.W. Hamat. Improvement of cepstrum analysis for the purpose to detect leak, feature and its location in water distribution system based on pressure transient analysis. *Journal of Mechanical Engineering*, SI 4(4):103–122, 2017.

[91] SBM Beck, J Foong, and WJ Staszewski. Wavelet and cepstrum analyses of leaks in pipe networks. In *Progress in Industrial Mathematics at ECMI 2004*, pages 559–563. Springer, 2006.

[92] M. Taghvaei, S. B.M. Beck, and W. J. Staszewski. Leak detection in pipelines using cepstrum analysis. *Measurement Science and Technology*, 17(2):367–372, 2006.

[93] Niloufar Motazedi and Stephen Beck. Leak detection using cepstrum of cross-correlation of transient pressure wave signals. *Proceedings of the Institution of Mechanical Engineers, Part C: Journal of Mechanical Engineering Science*, 232(15):2723–2735, 2018.

[94] Muhammad Waqar, Moez Louati, and Mohamed S Ghidaoui. Leak Localization Using Time Reversal Technique. *38th IAHR World Congress - "Water: Connecting the World"*, 38(May 2020):3351–3358, 2019.

[95] J. M. Muggleton, M. J. Brennan, and P. W. Linford. Axisymmetric wave propagation in fluid-filled pipes: Wavenumber measurements in in vacuo and buried pipes. *Journal of Sound and Vibration*, 270(1-2):171–190, 2004.

[96] M. Prek. Wavelet analysis of sound signal in fluid-filled viscoelastic pipes. *Journal of Fluids and Structures*, 19(1):63–72, 2004.

[97] Matjaz Prek. Analysis of wave propagation in fluid-filled viscoelastic pipes. *Mechanical Systems and Signal Processing*, 21(4):1907–1916, 2007.

[98] Matthew D. Gillette and Harvey F. Silverman. A linear closed-form algorithm for source localization from time-differences of arrival. *IEEE Signal Processing Letters*, 15(1):1–4, 2008.

[99] Brian O'Keefe. Finding Location with Time of Arrival and Time Difference of Arrival Techniques. *ECE Senior Capstone Project*, (2017 Tech Notes), 2017.

[100] DS Ballantine Jr, Robert M White, Stephen J Martin, Antonio J Ricco, ET Zellers, GC Frye, and H Wohltjen. *Acoustic wave sensors: theory, design and physico-chemical applications*. Elsevier, 1996.

[101] Rj Urick. Fundamentals of Underwater Sound. *International Association of Oil & Gas Producers*, (406):24, 2008.

[102] Alan Jeffrey. *Advanced engineering mathematics*. Elsevier, 2001.

[103] Lawrence E Kinsler, Austin R Frey, Alan B Coppens, and James V Sanders. Fundamentals of acoustics, 1999.

[104] BD Hauer, C Doolin, KSD Beach, and JP Davis. A general procedure for thermomechanical calibration of nano/micro-mechanical resonators. *Annals of Physics*, 339:181–207, 2013.

[105] Yong Woo Shin, Min Soo Kim, and Sang Kwon Lee. Identification of acoustic wave propagation in a duct line and its application to detection of impact source location based on signal processing. *Journal of Mechanical Science and Technology*, 24(12):2401–2411, 2010.

[106] R J Pinnington and A R Briscoe. Externally Applied Sensor for Axisymmetric Waves in a Fluid Filled Pipe, 1994.

[107] J. M. Muggleton, M. J. Brennan, and R. J. Pinnington. Wavenumber prediction of waves in buried pipes for water leak detection. *Journal of Sound and Vibration*, 249(5):939–954, 2002.

[108] Native Dynamics. Speed of sound in fluids and fluid in pipes. *Online Search*, 2018.

[109] M J Brennan, M Karimi, J M Muggleton, F C L Almeida, F Kroll De Lima, P C Ayala, D Obata, A T Paschoalini, and N Kessissoglou. On the effects of soil properties on leak noise propagation in plastic water distribution pipes. *Journal of Sound and Vibration*, 427:120–133, 2018.

[110] Léon Brillouin. *Wave propagation and group velocity*, volume 8. Academic press, 2013.

[111] John David Anderson Jr. *Fundamentals of aerodynamics*. Tata McGraw-Hill Education, 2010.

[112] A. F. Seybert and D. F. Ross. Experimental determination of acoustic properties using a two-microphone random-excitation technique. *The Journal of the Acoustical Society of America*, 61(5):1362–1370, 1977.

[113] RG Lyons. *Understanding Digital Signal Processing*. 2011.

[114] Anders Brandt. *Noise and vibration analysis: signal analysis and experimental procedures*. John Wiley & Sons, 2011.

[115] Nick Davis. An introduction to filters. *Online Search*, 2017.

[116] Christian Lalanne. *Mechanical Vibration and Shock Analysis, Random Vibration*, volume 3. John Wiley & Sons, 2014.

[117] Mylan R Cook, Kent L Gee, Scott D Sommerfeldt, and Tracianne B Neilsen. Coherence-based phase unwrapping for broadband acoustic signals. In *Proceedings of Meetings on Acoustics 173EAA*, volume 30, page 055005. Acoustical Society of America, 2017.

[118] Osama Hunaidi and Alex Wang. A new system for locating leaks in urban water distribution pipes. *Management of Environmental Quality: An International Journal*, 17(4):450–466, 2006.

[119] Carlos Gerardo Treviño-Palacios. Unfolding wrapped phase. *Optical Engineering*, 54(11):110503, 2015.

[120] JY Chung and DA Blaser. Transfer function method of measuring in-duct acoustic properties. i. theory. *The Journal of the Acoustical Society of America*, 68(3):907–913, 1980.

[121] JY Chung and DA Blaser. Transfer function method of measuring in-duct acoustic properties. ii. experiment. *The Journal of the Acoustical Society of America*, 68(3):914–921, 1980.

[122] A. F. Seybert. Two—sensor methods for the measurement of sound intensity and acoustic properties in ducts. *Journal of the Acoustical Society of America*, 83(6):2233–2239, 1988.

[123] He Shi, Jinzhe Gong, Aaron C Zecchin, Martin F Lambert, and Angus R Simpson. Hydraulic transient wave separation algorithm using a dual-sensor with applications to pipeline condition assessment. *Journal of Hydroinformatics*, 19(5):752–765, 2017.

[124] Wei Zeng, Jinzhe Gong, Benjamin S Cazzolato, Aaron C Zecchin, Martin F Lambert, and Angus R Simpson. Condition assessment of pipelines using a bi-directional layer-peeling method and a dual-sensor configuration. *Journal of Sound and Vibration*, 457:181–196, 2019.

[125] Kenneth W Goff. The development of a variable time delay. *Proceedings of the IRE*, 41(11):1578–1584, 1953.

[126] H Foerster. Correlation analysis of narrow-band signals and application to leakage localization. *Kernenergie (Berlin)*, 30(3):101–105, 1987.

[127] FB Hildebrand. Introduction to numerical analysis. mcgraw-hili book co. *New York*, 1956.

[128] Ramdas Kumaresan, DW Tufts, and Loues L Scharf. A prony method for noisy data: Choosing the signal components and selecting the order in exponential signal models. *Proceedings of the IEEE*, 72(2):230–233, 1984.

[129] Y Hua and T K Sarkar. Matrix pencil method for estimating parameters of exponentially damped/undamped sinusoids in noise. *IEEE Transactions on Acoustics, Speech, and Signal Processing*, 38(5):814–824, may 1990.

[130] Tapan K. Sarkar and Odilon Pereira. Using the Matrix Pencil Method to Estimate the Parameters of a Sum of Complex Exponentials. *IEEE Antennas and Propagation Magazine*, 37(1):48–55, 1995.

[131] Frank J Massey Jr. The kolmogorov-smirnov test for goodness of fit. *Journal of the American statistical Association*, 46(253):68–78, 1951.

[132] Daniel Griffin and Jae Lim. Signal estimation from modified short-time fourier transform. *IEEE Transactions on acoustics, speech, and signal processing*, 32(2):236–243, 1984.

[133] MeerP ComaniciuD. Arobust approach toward feature space analysis [j]. *IEEE Transactions on Pattern Analysis and Machine Intelligence*, 24(5):313–329, 2002.

[134] Dorin Comaniciu and Peter Meer. Mean shift analysis and applications. In *Proceedings of the Seventh IEEE International Conference on Computer Vision*, volume 2, pages 1197–1203. IEEE, 1999.

[135] Stanley Fong, Jinane Harmouche, Sriram Narasimhan, and Jerome Antoni. Mean shift clustering-based analysis of nonstationary vibration signals for machinery diagnostics. *IEEE Transactions on Instrumentation and Measurement*, 69(7):4056–4066, 2019.

[136] Enrique Garcia, Pablo Poudereux, Alvaro Hernandez, Jesus Urena, and David Gualda. A robust UWB indoor positioning system for highly complex environments. *Proceedings of the IEEE International Conference on Industrial Technology*, 2015-June(June):3386–3391, 2015.

[137] United States Plastic Corp. 6" Gray PVC Schedule 80 pipe Item No. 26331. *Online Search*, 11/24/2016.

[138] Richard A G Fleming, Mark Kwiecinski, and Dennis F Jones. Analysis of Barrel Stave Flextensional Transducer using MAVART and ATILA Finite Element Codes. *Canadian Acoustics*, 36(2):2–6, 2008.

[139] Kenneth D Rolt. History of the flextensional electroacoustic transducer. *The Journal of the Acoustical Society of America*, 87(3):1340–1349, 1990.

[140] Aykut Şahin. Barrel-Stave Flextensional Transducer Design. (March), 2009.

[141] William G Jacoby. Loess:: a nonparametric, graphical tool for depicting relationships between variables. *Electoral Studies*, 19(4):577–613, 2000.

[142] Fabrício César Lobato de Almeida. Improved Acoustic Methods for Leak Detection in Buried Plastic Water Distribution Pipes. page 274, 2013.

[143] JM Muggleton, MJ Brennan, and Y Gao. Determining the location of buried plastic water pipes from measurements of ground surface vibration. *Journal of Applied Geophysics*, 75(1):54–61, 2011.

[144] Julius S Bendat and Allan G Piersol. *Random data: analysis and measurement procedures*, volume 729. John Wiley & Sons, 2011.

[145] Ismail Güvenç and Chia Chin Chong. A survey on TOA based wireless localization and NLOS mitigation techniques. *IEEE Communications Surveys and Tutorials*, 11(3):107–124, 2009.

[146] Sinan Gezici and Zafer Sahinoglu. Uwb geolocation techniques for ieee 802.15. 4a personal area networks. *MERL Technical report*, 2004.

[147] Dennis F Jones and D A Christopher. A broadband omnidirectional barrel-stave flextensional transducer. *The Journal of the Acoustical Society of America*, 106(2):L13–L17, 1999.

[148] J-N Decarpigny, Bernard Hamonic, and Oscar Bryan Wilson. The design of low frequency underwater acoustic projectors: present status and future trends. *IEEE journal of oceanic engineering*, 16(1):107–122, 1991.

[149] Dhammika De Silva, John Mashford, and Stewart Burn. Computer Aided Leak Location and Sizing in Pipe Networks Urban Water Security Research Alliance Technical Report No . 17. Urban Water Security Research Alliance Technical Report NO. 17, 2011(17).de. *Urban Water Security Research Alliance Technical Report No. 17*, 2011(17), 2011.

[150] Marco Ferrante, Caterina Capponi, Richard Collins, Jonathan Edwards, Bruno Brunone, and Silvia Meniconi. Numerical transient analysis of random leakage in time and frequency domains. *Civil Engineering and Environmental Systems*, 33(1):70–84, 2016.

[151] Stewart Burn, Dhammika DeSilva, Matthias Eiswirth, Osama Hunaidi, Andrew Speers, and Julian Thornton. Pipe Leakage - Future Challenges and Solutions. (June), 1999.

[152] SLR. Assessing Risk and Modeling a Sudden Gas Release Due to Gas Pipeline Ruptures. pages 5–22, 2009.

[153] R Konersmann, C Kühl, and J Ludwig. *On the risks of transporting liquid and gaseous fuels in pipelines*. 2009.

[154] Gregory J Kirmeyer, William Richards, and Ch Dery Smith. *Assessment of water distribution systems and associated research needs, An*. AWWA, 1994.

[155] Kalyan R. Piratla, Sreeganesh R. Yerri, Sepideh Yazdekhasti, Jinsung Cho, Dan Koo, and John C. Matthews. Empirical Analysis of Water-Main Failure Consequences. *Procedia Engineering*, 118:727–734, 2015.

[156] Balvant Rajani and Yehuda Kleiner. Comprehensive review of structural deterioration of water mains: Physically based models. *Urban Water*, 3(3):151–164, 2001.

[157] Transportation Research Board (NA) National Research Council, National Research Council (US). Committee for Pipelines, Public Safety, Scoping Study on the Feasibility of Developing Risk-Informed Land Use Guidance near Existing, and Future Transmission Pipelines. *Transmission Pipelines and Land Use: A Risk-informed Approach*, volume 281. Transportation Research Board, 2004.

[158] T Graf. Acoustic Wave Propagation in Water Filled Buried Plastic Pipes. *Comsol Conference*, 2014.

[159] Tiantian Zhang, Yufei Tan, Xuedan Zhang, and Jinhui Zhao. A novel hybrid technique for leak detection and location in straight pipelines. *Journal of Loss Prevention in the Process Industries*, 35:157–168, 2015.

[160] Jim CP Liou. Leak detection by mass balance effective for norman wells line. *Oil and gas journal*, 94(17), 1996.

[161] B Parry, R Mactaggart, and C Toerper. Compensated volume balance leak detection on a batched lpg pipeline. In *Proceedings of the International Conference on Offshore Mechanics and Arctic Engineering*, pages 501–501. American Society of Mechanical Engineers, 1992.

[162] Gerhard Geiger. State-of-the-Art in Leak Detection and Localization. *Oil gas european magazine*, 12(4):1–6, 2006.

[163] L. Billmann and Rolf Isermann. Leak Detection Methods for Pipelines. *Automatica*, 23(3):381–385, 1987.

[164] Ascher H Shapiro. *The dynamics and thermodynamics of compressible fluid flow*. John Wiley & Sons, 1953.

[165] EJ Farmer, PE Diane, and J Hovey. Pressure point analysis leak detection. methodology, performance and application. In *25 th One Day Technical Meeting A1ChE*, 1996.

[166] E.J. Farmer, P.E. A new approach to pipe line leak detection. *Pipe Line Industry; (USA)*, 70(6), 6 1989.

[167] E Benjamin Wylie, Victor Lyle Streeter, and Lisheng Suo. *Fluid transients in systems*, volume 1. Prentice Hall Englewood Cliffs, NJ, 1993.

[168] Huali Chen, Hao Ye, LV Chen, and Hongyu Su. Application of support vector machine learning to leak detection and location in pipelines. In *Instrumentation and Measurement Technology Conference, 2004. IMTC 04. Proceedings of the 21st IEEE*, volume 3, pages 2273–2277. IEEE, 2004.

[169] Alex Souza de Joode and Andrew Hoffman. Pipeline leak detection and theft detection using rarefaction waves. In *6th pipeline technology conference*, 2011.

[170] Xue Jun Zhang. Statistical leak detection in gas and liquid pipelines. *Pipes & pipelines international*, 38(4):26–29, 1993.

[171] Steven G Buchberger and Gayatri Nadimpalli. Leak Estimation in Water Distribution Systems by Statistical Analysis of Flow Readings. *Journal of Water Resources Planning & Management*, 130(4):321–329, 2004.

[172] Witness Mpesha, Sarah L Gassman, and M Hanif Chaudhry. Leak detection in pipes by frequency response method. *Journal of Hydraulic Engineering*, 127(2):134–147, 2001.

[173] Joydeb Mukherjee and Shankar Narasimhan. Leak detection in networks of pipelines by the generalized likelihood ratio method. *Industrial & engineering chemistry research*, 35(6):1886–1893, 1996.

[174] Johannes H Andersen and Roger S Powell. Implicit state-estimation technique for water network monitoring. *Urban Water*, 2(2):123–130, 2000.

[175] J Golby and T Woodward. Find that leak. *IEE review*, 45(5):219–221, 1999.

[176] Marc Niklès, Bernhard H Vogel, Fabien Briffod, Stephan Grosswig, Florian Sauser, Steffen Luebbecke, André Bals, and Thomas Pfeiffer. Leakage detection using fiber optics distributed temperature monitoring. In *Smart Structures and Materials 2004:*

Smart Sensor Technology and Measurement Systems, volume 5384, pages 18–26. International Society for Optics and Photonics, 2004.

[177] Lufan Zou and Taha Landolsi. Pipeline leakage detection using fiber-optic distributed strain and temperature sensors. 2014.

[178] Kajiro Watanabe and DM Himmelblau. Detection and location of a leak in a gas-transport pipeline by a new acoustic method. *AIChE Journal*, 32(10):1690–1701, 1986.

[179] Boaz Porat. *A course in digital signal processing*. Wiley, 1997.

[180] KN Stevens. Autocorrelation analysis of speech sounds. *The Journal of the Acoustical Society of America*, 22(6):769–771, 1950.

[181] Lizeth Torres, Javier Jiménez-Cabas, Omar González, Lázaro Molina, and Francisco Ronay López-Estrada. Kalman filters for leak diagnosis in pipelines: Brief history and future research. *Journal of Marine Science and Engineering*, 8(3), 2020.

[182] MD Rahman and Kai-Bor Yu. Total least squares approach for frequency estimation using linear prediction. *IEEE Transactions on Acoustics, Speech, and Signal Processing*, 35(10):1440–1454, 1987.

[183] Greg Welch, Gary Bishop, et al. An introduction to the kalman filter. 1995.

[184] Sensor Technology. Low frequency transducers from sensor technology. *Online Search*, 2018.

[185] Y. Gao, M. J. Brennan, P. F. Joseph, J. M. Muggleton, and O. Hunaidi. A model of the correlation function of leak noise in buried plastic pipes. *Journal of Sound and Vibration*, 277(1-2):133–148, 2004.

[186] Dragoș Dumitrescu and Costin-Anton Boiangiu. A study of image upsampling and downsampling filters. *Computers*, 8(2):30, 2019.

[187] Wolfram Mathworld. Bessel function zeros. *Dostupno na: http://mathworld. wolfram. com/BesselFunctionZeros. html qv-volumna generacija topline, volumetric heat*, 2010.

[188] J. Su, J. Rupp, A. Garmory, and J. F. Carrotte. Measurements and computational fluid dynamics predictions of the acoustic impedance of orifices. *Journal of Sound and Vibration*, 352:174–191, 2015.

APPENDICES

Appendix A

List of Publications

The following is a list of journal publications and conference papers resulting from the work contained in this dissertation:

Publications

1. **Kafle, M.D.**, and Narasimhan, S. (2020). Active acoustic leak detection in a pressurized PVC pipe. *Urban Water Journal, 17:4, 315-324.*
   DOI: 10.1080/1573062X.2020.1771381

2. **Kafle, M.D.**, Fong, S., and Narasimhan, S.. Active acoustic leak detection and localization in a plastic pipe using time delay estimation. *Applied Acoustics* - Under review.

3. **Kafle, M.D.**, and Narasimhan, S.. Use of Multilateration (MLAT) with Acoustic Methods for Leak Detection and Localization in Water Distribution Networks. *Journal of Sound and Vibration* - Under preparation.

Peer-reviewed Conference Proceedings - Full paper

1. **Kafle, M.D.**, and Narasimhan, S. (2021). Active acoustics in water distribution networks for leak detection and localization. *Proc., 16th Pipeline Technology Conference*, ptc2021, Berlin.

Appendix B

Dimensions of Lab-based WDNs

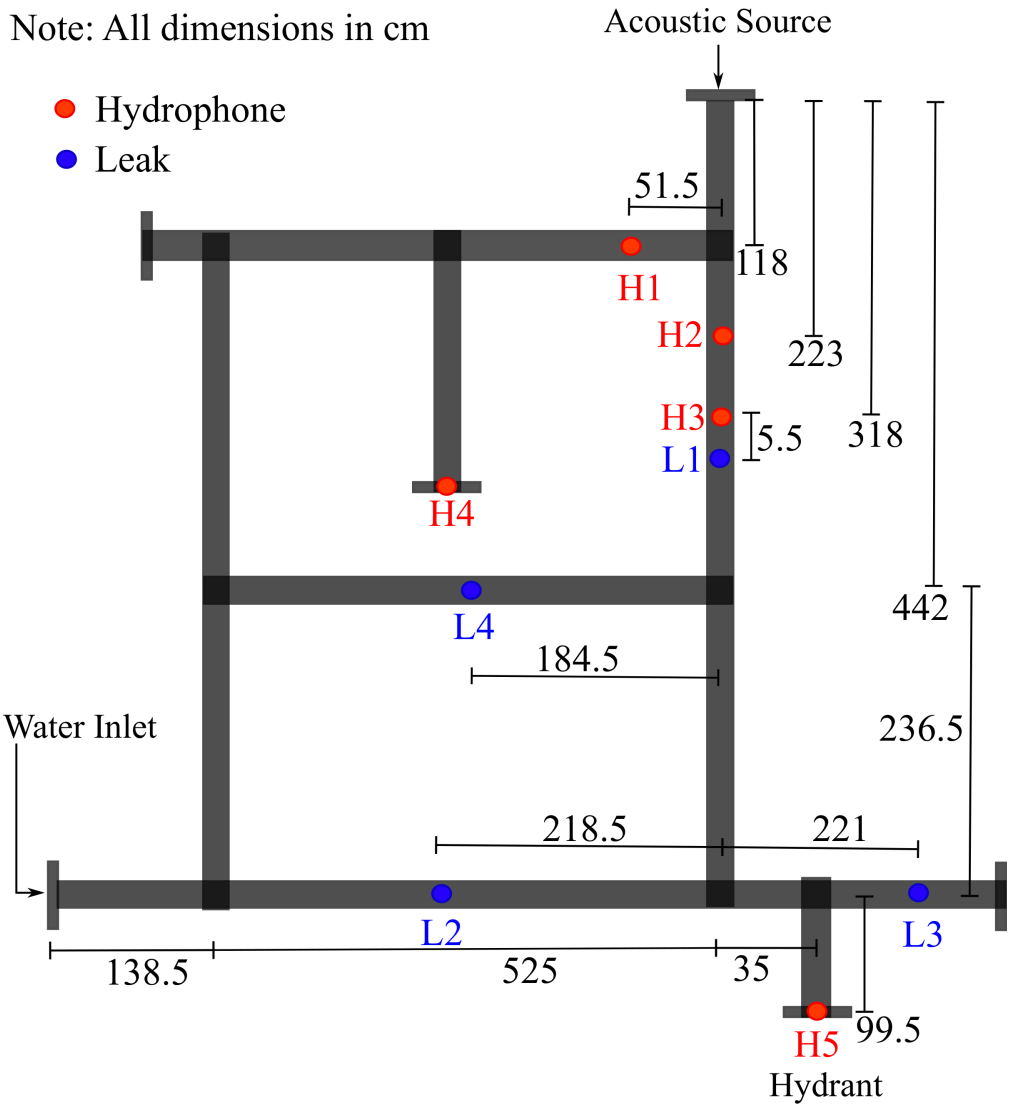

Figure B.1: Lab WDNs dimensions

Appendix C

Pictures from the Experimental Setup

Figure C.1: Pictures from the real experiment setup; (a) WDNs showing the hydrant; (b) view from the diagonal of a hydrant; (c) single pipe setup

Appendix D

First Few Roots of Bessel Function and its Derivatives

Source: Fundamentals of Acoustics [103]

Table D.1: First few roots of Bessel function and its derivative

	j_{mn}					
m \ n	0	1	2	3	4	5
0	—	2.40	5.52	8.65	11.79	14.93
1	0	3.83	7.02	10.17	13.32	16.47
2	0	5.14	8.42	11.62	14.80	17.96
3	0	6.38	9.76	13.02	16.22	19.41
4	0	7.59	11.06	14.37	17.62	20.83
5	0	8.77	12.34	15.70	18.98	22.22

	j'_{mn}				
m \ n	1	2	3	4	5
0	0	3.83	7.02	10.17	13.32
1	1.84	5.33	8.54	11.71	14.86
2	3.05	6.71	9.97	13.17	16.35
3	4.20	8.02	11.35	14.59	17.79
4	5.32	9.28	12.68	15.96	19.20
5	6.41	10.52	13.99	17.31	20.58

Appendix E

NLOS Mitigation Techniques

E.1 Extended Kalman Filter

Kalman filter is an algorithm that provides an efficient computational solution of the least-square methods using a series of measurements sampled over time containing noise to produce more accurate estimates [183]. Extended Kalman filter is a non-linear Kalman filter that linearizes about the current mean and covariance.

In this dissertation, EKF is proposed as a smoother for the NLOS errors in leak localization. As the leak position is not dynamic, the prediction stage of the EKF is not used, and only the update stage is applied for the localization. The co-variance, $\boldsymbol{S}_k$ of the measurement can be estimated as,

$$\boldsymbol{S}_k = \boldsymbol{H}_k.\boldsymbol{P}_k^-.\boldsymbol{H}_k^T + \boldsymbol{R}_k, \tag{E.1}$$

where $\boldsymbol{H}_k$ is the observation matrix at time instant k; $\boldsymbol{P}_k^-$ is the a priori covariance matrix at time instant k and $\boldsymbol{R}_k^-$ is the noise matrix.

Kalman Filter minimizes the mean squared error by using a so-called Kalman gain matrix $\boldsymbol{K}_k$ which finds the optimal weight of the measurements and is given by,

$$\boldsymbol{K}_k = \boldsymbol{P}_k^-.\boldsymbol{H}_k^T.[\boldsymbol{S}_k]^{-1}, \tag{E.2}$$

$$\boldsymbol{K}_k = \boldsymbol{P}_k^-.\boldsymbol{H}_k^T.[\boldsymbol{H}_k.\boldsymbol{P}_k^-.\boldsymbol{H}_k^T + \boldsymbol{R}_k]^{-1}. \tag{E.3}$$

Kalman gain contributes to the calculation of $\hat{\boldsymbol{x}}_k$ in Eq. E.5 based on the measurements and a priori estimates. The measurement is trusted more, and it contributes to the calculation

of $\hat{\boldsymbol{x}}_k$ more than the a priori state estimate, if the measurement noise is small. On the contrary, where the error in the a priori estimate is small, a priori estimate is trusted more while computing $\hat{\boldsymbol{x}}_k$ than the measurement.

The posterior state and the co-variance at time k are given by Eqs. E.4 and E.5. The first term in Eq. E.4 is the prediction stage, while the latter term is the update stage. As mentioned earlier, the prediction stage of the EKF is not used as the leak position does not change its position during the computation of its location. In the equations,

$$\hat{\boldsymbol{x}}_k = \hat{\boldsymbol{x}}_k^- + \boldsymbol{K}_k.(\boldsymbol{z}_k - h(\hat{x}_k^-)), \tag{E.4}$$

$$\boldsymbol{P}_k = (\boldsymbol{I} - \boldsymbol{K}_k.\boldsymbol{H}_k).\boldsymbol{P}_k^-, \tag{E.5}$$

$\boldsymbol{z}_k$ is the TDOA measured vector at k; and $\hat{\boldsymbol{x}}_k = [\hat{x}_k, \hat{y}_k]^T$ is the state vector which is equal to the 2D position of the leak at k. The vector $h(\hat{x}_k^-)$ defined as,

$$h(\hat{x}_k^-) = \begin{bmatrix} h_1(\hat{x}_k^-) \\ h_2(\hat{x}_k^-) \\ . \\ . \\ h_{N-1}(\hat{x}_k^-) \end{bmatrix}, \tag{E.6}$$

where a priori estimated TDOA vector $h_i(\hat{x}_k^-)$ is

$$h_i(\hat{x}_k^-) = \sqrt{(\hat{x}_k^- - x_i)^2 + (\hat{y}_k^- - y_i)^2 + (\hat{z}_k^- - z_i)^2} \tag{E.7}$$

$$+\sqrt{(\hat{x}_k^- - x_r)^2 + (\hat{y}_k^- - y_r)^2 + (\hat{z}_k^- - z_r)^2}, \quad \text{(Active method)} \tag{E.8}$$

$$h_i(\hat{x}_k^-) = \sqrt{(\hat{x}_k^- - x_i)^2 + (\hat{y}_k^- - y_i)^2 + (\hat{z}_k^- - z_i)^2}. \quad \text{(Passive method)} \tag{E.9}$$

The EKF linearizes the non-linear function around the mean of the current state estimates $\hat{\boldsymbol{x}}_k$ and $\boldsymbol{P}_k$. At each time step, the linearization is performed locally, and the resulting Jacobian matrices are then used in the prediction and correction stages of the Kalman Filter algorithm. The observation matrix $\boldsymbol{H}_k$ defined as the Jacobian is given by,

$$\boldsymbol{H}_k = \begin{bmatrix} \frac{\partial h_1(\hat{x}_k^-)}{\partial \hat{x}_k^-} & \frac{\partial h_1(\hat{x}_k^-)}{\partial \hat{y}_k^-} \\ . & . \\ . & . \\ \frac{\partial h_{N-1}(\hat{x}_k^-)}{\partial \hat{x}_k^-} & \frac{\partial h_{N-1}(\hat{x}_k^-)}{\partial \hat{y}_k^-}) \end{bmatrix}. \tag{E.10}$$

The observation noise matrix $\boldsymbol{R}_k$ can be found by processing the measurements while the output of the system is held constant. In this case, only noise remains in the data after its mean is removed. The matrix $\boldsymbol{R}_k$ is given by,

$$\boldsymbol{R}_k = \begin{bmatrix} \sigma_{1,k}^2 + \sigma_{2,k}^2 & \sigma_{1,k}^2 & \sigma_{1,k}^2 \\ \sigma_{1,k}^2 & \ddots & \sigma_{1,k}^2 \\ \sigma_{1,k}^2 & \sigma_{1,k}^2 & \sigma_{1,k}^2 + \sigma_{N,k}^2 \end{bmatrix}. \tag{E.11}$$

The diagonal term of the matrix $\boldsymbol{R}_k$ is the variance σ^2 and the entry values depend on the NLOS condition measured for each sensor pair. Chapter 6 describes the experimental studies and the implementation of multilateration techniques and EKF.

E.2 Maximum Likelihood Method

Consider the network that has fixed sensor location given by $\hat{\boldsymbol{x}} = [\hat{x}\,\hat{y}]^T$ and a leak location given by $\boldsymbol{x}_i = [x_i\, y_i]$, $\hat{d}_i$ is the distance between the sensor location and leak position and can be modeled as [145],

$$\hat{d}_i = d_i + b_i + n_i = c\, t_i, \tag{E.12}$$

where t_i is the TOA of the signal at the ith sensor, d_i is the real distance between the sensor and leak location, n_i is the additive white gaussian noise with variance σ^2, and b_i is the bias introduced due to NLOS and is given by,

$$b_i = \begin{cases} 0 & \text{if ith sensor is LOS,} \\ \psi_i & \text{if ith sensor is NLOS.} \end{cases}$$

For NLOS sensors, the bias term ψ_i is modeled using various distributions as needed in the literature.

Assume the actual distance between the fixed sensors and leak location is given by $\mathbf{d} = \mathbf{d(x)} = [d_1, d_2, ...d_N]^T$. The measured distance is given by $= [\hat{d}_1, \hat{d}_2, ...\hat{d}_N]^T$ and the bias is given by $\mathbf{b} = [b_1, b_2, ...b_N]^T$. In the absence of noise and NLOS bias, the true distance d_i is obtained using the expression,

$$\hat{d}_i^2 = (x - x_i)^2 + (y - y_i)^2, \quad \text{i = 1,2,..,N} \tag{E.13}$$

In the absence of the NLOS bias, the conditional PDF of $\hat{\boldsymbol{d}}$ given $\boldsymbol{x}$ is expressed as [145],

$$P(\hat{\boldsymbol{d}}|\boldsymbol{x}) = \prod_{i=1}^{N} \frac{1}{\sqrt{2\pi\sigma_i^2}} \exp\{-\frac{(\hat{d}_i - d_i)^2}{2\sigma_i^2}\}. \tag{E.14}$$

The maximum likelihood (ML) solution for $\boldsymbol{x}$ is the one that maximizes $P(\hat{\boldsymbol{d}}|\boldsymbol{x})$ and solving for $\boldsymbol{x}$ requires search for all the x and y value.

To mitigate the NLOS errors, prior knowledge regarding the distribution of NLOS bias is required. According to [146], the bias b_i can be assumed to be exponentially distributed with parameter λ_i. Thus, the simplified ML solution for NLOS condition is given by,

$$\hat{\boldsymbol{x}} = \max_{\boldsymbol{x}}\{\sum_i \lambda_i(\hat{d}_i - d_i) + \sum_i \frac{(\hat{d}_i - d_i)^2}{2\sigma_i^2}\}. \tag{E.15}$$

Appendix F

Leak Localization using Multilateration in a Single Pipe

In the case of single pipe, for the broadband white noise as mentioned in section 6.3.2, the cross correlation of two signals from H1 and H2 is treated using MPM to obtain the time delays corresponding to different impedance changes. An example of time delay comparison between leak and no leak is shown in a histogram chart in Fig. F.1. The histogram bar bounded by [0.0173 0.0185] seconds signifies the leak location which gives the estimated leak distance bounded by [3.72 4.1] m and centered at 3.91 m from the H2 (true value is 4 m).

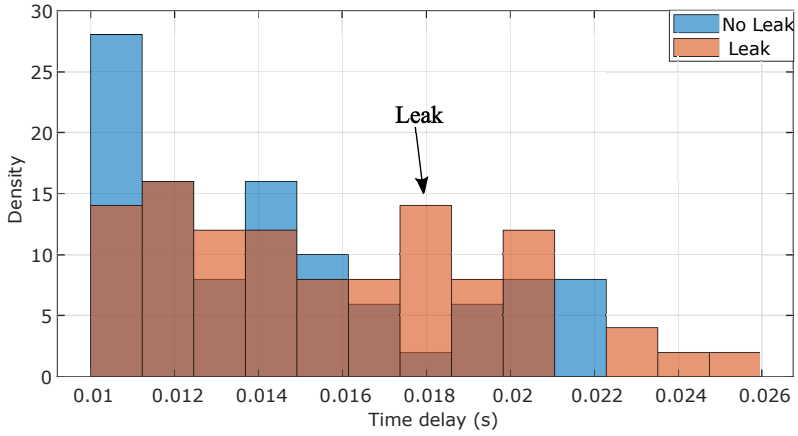

Figure F.1: Comparison of time delay for leak and no leak using MPM in a single pipe

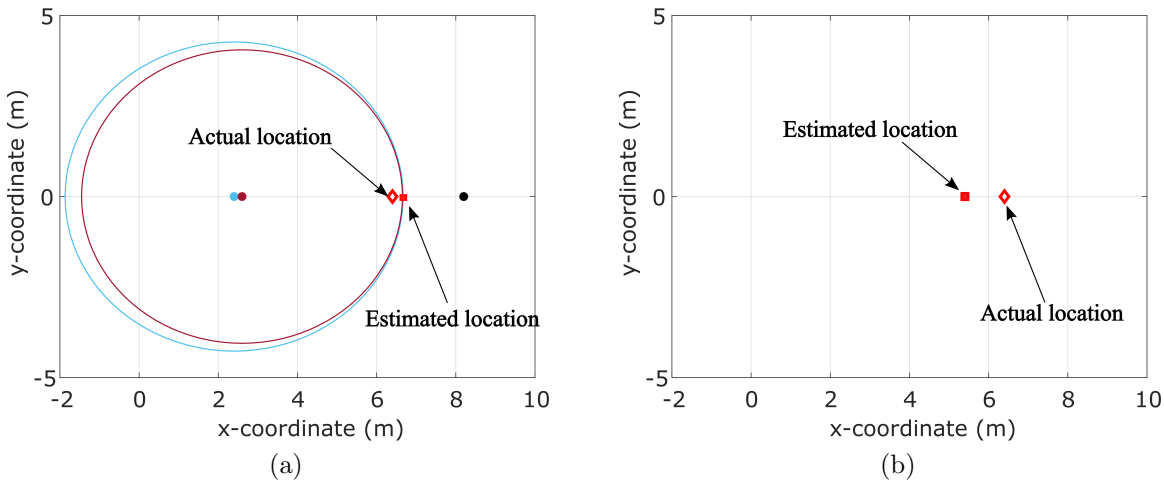

Figure F.2: Comparison of leak localization in single pipe using (a) TOA; (b) TDOA

With the second time delay obtained from the MPM of the cross-correlation signal between H2 and H3, two circles are drawn using TOA Eq. 4.36 with centre at H1 and H2. The approximate intersection of the circle gives the location of leak. Similarly, the closed form solution of TDOA represented by Eq. 4.38 is solved with the position of H1 as reference sensor($x_r = x_1, y_r = y_1$) and two time delays from H1H2 and H1H3. In a single pipe case, the unknown in Eq. 4.38 are the x_s and D_r and with two equations, the position, x_s can be easily identified. The location of leak obtained using TOA and TDOA are shown in Fig. F.2. Although, the location of the leak obtained from both the MLAT technique is consistent with the distance given by MPM, the TOA method best estimates the true leak position which is shown in Fig. F.2a .

Appendix G

Results of High Frequency Continuous Sine Wave from WDNs

G.1 Results of Continuous Sine Wave of 1600 Hz with Leak L1

While it is clear that reflection of plane waves occur at extremely low frequencies, for exploratory reasons, testing is conducted at high frequencies to determine the sensitivity of high frequency plane waves to leaks. The fundamental resonant frequency of the acoustic source (flextensional mode) is 1600 Hz. Since this still falls within the cut-off frequency for a plane wave, a sine wave of 1600 Hz is used to excite the WDNs for a length of 4 seconds with leak L1 open, and the time traces is recorded at one hydrophone location H2 as shown in Fig. G.1. The FFT of the time traces due to L1 obtained from H2 is shown in Fig. G.2.

The results show that for the leak case (L1), the amplitude of the excitation frequency is significantly higher at the hydrophone located close to the acoustic source and before leak location than in the no leak case. Unlike the ambient condition, the change in amplitude of the excitation frequency due to the leak is detectable and can be seen in the time signal and frequency spectrum of the data obtained from H2, demonstrating that the active acoustic method is a better detector of leaks irrespective of the pipe configuration and leak position. The theoretical explanation is not possible at this time and will be investigated in future work. The current working hypothesis is that this is due to the presence of electro-mechanical coupling between the pipe-driver system and the pipe, which changes

when there is a leak. The frequency-domain results show the effect of the leak causing the amplitude to increase at various frequency bands. A similar pattern is also observed when simulating other leak locations.

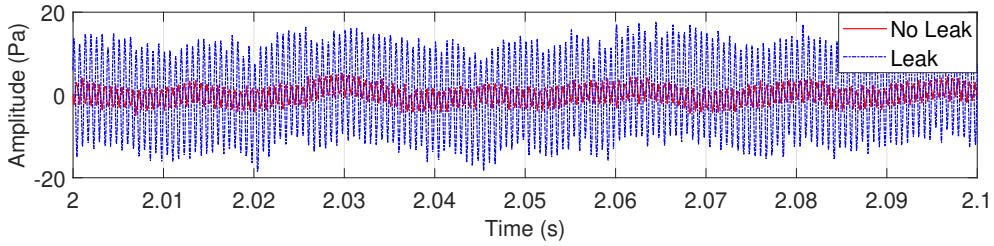

Figure G.1: Pipe network: time trace of 1600 Hz sine wave from H2 with/without leak L1

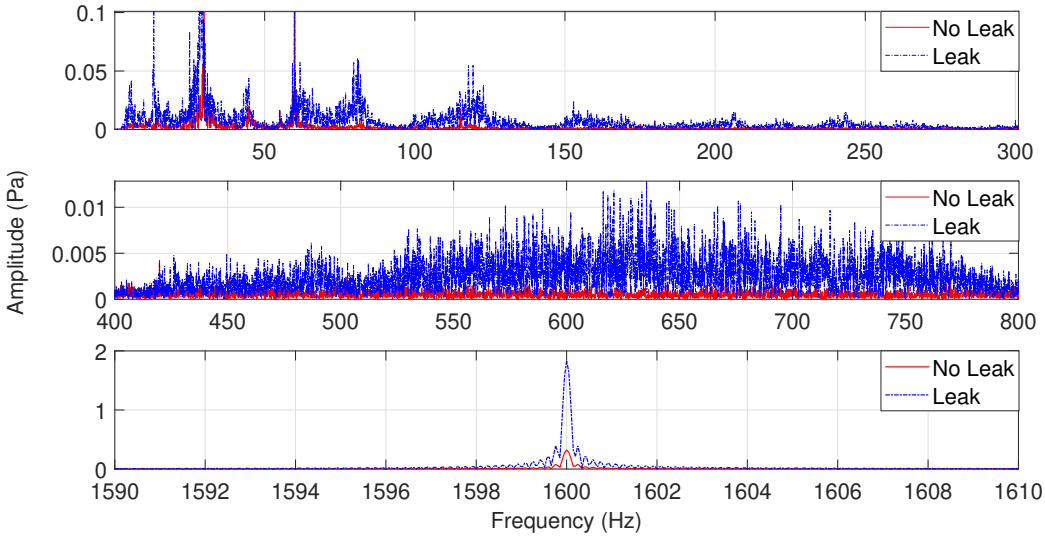

Figure G.2: Pipe network: FFT of the time trace from H2 with/without leak L1